Fall 11-9-2016

Non-Destructive Evaluation of Functional Material Properties Performed on Additively Manufactured Coupons

Devin S. Plagge
Devin S. Plagge

Devin S. Plagge

Candidate

Mechanical Engineering

Department

This thesis is approved, and it is acceptable in quality and form for publication:

Approved by the Thesis Committee:

Yu-Lin Shen, Chairperson

John Russell

Nicholas Leathe

NON-DESTRUCTIVE EVALUATION OF FUNCTIONAL MATERIAL PROPERTIES PERFORMED ON ADDITIVELY MANUFACTURED COUPONS

By

Devin S. Plagge

B.S., Mechanical Engineering, University of New Mexico, 2013

THESIS

Submitted in Partial Fulfillment of the

Requirements for the Degree of

Master of Science

Mechanical Engineering

The University of New Mexico

Albuquerque, New Mexico

December, 2016

NON-DESTRUCTIVE EVALUATION OF FUNCTIONAL MATERIAL PROPERTIES PERFORMED ON ADDITIVELY MANUFACTURED COUPONS

By

Devin S. Plagge

B.S., Mechanical Engineering, University of New Mexico, 2013

M.S., Mechanical Engineering, University of New Mexico, 2016

ABSTRACT

This thesis presents the development of non-destructive characterization of functional material properties of additively manufactured metals. In particular, this study was focused on the common structural stainless steel alloy, 316L, utilizing a coupon designed specifically for simple modal analysis. Additive manufacturing (AM) has moved to the forefront of the manufacturing world, particularly in aerospace and defense segments because of the potential to produce multi-functional, highly optimized components. The ability to confidently qualify these complex, and thus expensive, components has been lagging behind the advancing technology. The adoption of traditional characterization techniques developed for wrought materials has been most common, and much useful data can be extracted from these methods, but many of these tests are destructive in nature and thus are performed on representative samples. By taking advantage of the Modal Frequency Technique (MFT), the functional bulk properties of an as-printed component can be accurately characterized and the anisotropies inherent to AM can be quantified. Tests were performed using laser Doppler vibrometry and coupled with finite element analysis to show the ability to determine the functional Young's modulus of AM coupons. These tests also identified a dependence of this bulk Young's modulus on both the print orientation and the feature thickness. Modal frequencies were determined across a range of material parameters and experimental data was aligned with these values to determine the resultant Young's modulus for a suite of coupon dimensions printed in to traditional orientations using powder bed direct metal laser sintering (DMLS).

Table of Contents

List of Figures

List of Tables

CHAPTER 1: INTRODUCTION

1.1 Statement of research

The field of additive manufacturing, while not new, has recently gained momentum as more than just a novel method for producing fit-test prototypes and physical models. The progress in the research of additive manufacturing (AM) of metals has opened a new design space enabled by the application of AM to functional components produced from structural metallic alloys with increasing interest from high-level manufacturing companies (1-6). While the prospect for utilizing metallic AM parts is great, there is much speculation into the true quality of parts that these processes can produce. Variations in raw materials up through processing parameters and removal of supports all contribute to the uncertainty associated with AM parts. Qualification of AM parts is one of the biggest hurdles to the inclusion of AM parts in high-consequence applications (7-10). Much of current research into material properties of metallic AM is focused on the processing parameters and their effect on the microstructure of the material (11-19). This is indeed valuable to the complete understanding of the conversion from powdered metal into a fully dense part, but this does not tell us about the functional properties of the part, i.e. the overall stiffness, Young's modulus, anisotropies and any other uniqueness due to the geometry of the part. Until there is sufficient confidence in the uniform processing throughout the entire part, these microstructure analyses will likely hold locally, whereas the global part properties will dictate its functional performance. Many qualification techniques currently available for AM parts are destructive in nature, and thus expensive. Also, destructive tests are not as valuable with current AM processes due to the perceived inconsistencies within a build volume, across build lots and between AM platforms. Traditional testing is partially applicable, generally with caution and specific accommodations necessary to adapt to AM

materials (20). The development of a non-destructive method of testing these macroscopic properties such as Young's modulus is important to the development of functional AM parts and their acceptance into high-consequence applications. The aim of this thesis is to explore the applicability and accuracy of a non-destructive evaluation technique utilizing the modal frequency response, specifically to AM parts. This research is of particular interest to the aerospace and defense industries, and has potential to impact many more arenas such as the automotive and medical industries who are anxious to adopt AM as a larger part of their manufacturing footprint (21).

1.2 Objective of Research

This thesis aims to measure and quantify the functional Young's Modulus in a non-destructive manner. The properties will be extracted from an AM coupon using the Modal Frequency Technique (MFT). This evaluation technique observes the resonant vibrational modes of a particular part, and, when coupled with known parameters like the parts geometry and density, can be used to extract these functional parameters. MFT is not new, and has been used as a non-destructive evaluation (NDE) method for years. The uniqueness is introduced by its application to AM parts, and more specifically within this thesis, the design of an AM coupon intended specifically for this evaluation technique. The design of the coupon geometry lends itself to this evaluation technique, given that it utilizes a series of cantilever beams oriented either parallel or perpendicular to the build plane, depending on build orientation. This provides a means to identify simple mode shapes and measure their modal frequencies. Also, by varying the thickness of these cantilever beams, the bulk material can be compared to the wall material, giving us another parameter with which to

guide AM part design. The objective of this thesis is to determine the feasibility of utilizing the MFT to characterize and predict functional material properties for AM parts.

1.3 Methods of Research

This work evaluates the applicability of the MFT to AM metallic parts. The coupons characterized herein were manufactured by Direct Metal Laser Sintering (DMLS) of 316L Stainless Steel. The coupons will be displaced perpendicular to the cantilever series, then rapidly released and the vibrational response from the cantilevers will be measured. This data will contain the vibrational response of the coupon, and thus contain the desired modal frequency data. To collect the data for the MFT, we will be utilizing a laser Doppler vibrometer to allow for non-contact measurement of the instantaneous velocity of the coupon. The test apparatus provides a mounting location for the coupon, an adjustable stage for coupon location, a transverse manual linear stage to displace the nose of the coupons, and an air cylinder to quickly release the cantilevers to induce the vibrational response. The laser Doppler vibrometer provides very accurate and very fast measurements of velocity versus time without introducing unnecessary error into the experiment, as they are a non-contact measurement device. This will allow us to measure the response of the nose of the coupon and, from this data, the modal frequencies can be extracted. Using Fourier transforms, the time domain information can be decomposed into the frequency domain, and this frequency domain information will more easily display the resonant frequencies of each particular coupon. With these modal frequencies and the known part geometry and measured density, the Young's modulus can then be derived for each coupon by comparison of the modal frequencies to those generated from a computer finite element analysis (FEA) simulation. These frequencies, will then be compared to those generated by

a particular parameter set within the FEA simulation and thus, the Young's modulus extracted for each coupon.

1.4 Structure of Thesis

This thesis contains six chapters. Chapter 1 introduces the intent of the research, background and the methods for characterization.

Chapter 2 is a review of the manufacturing methods and evaluation techniques relevant to this research. These include a review of additive manufacturing, knowledge gaps preventing the widespread adoption of AM, non-destructive evaluation methods and modal frequency techniques for characterizing material properties.

Chapter 3 is a review of the modal frequency method. This chapter presents the relevance of the modal frequencies, methods for collection of this data, analysis techniques and considerations for the use of the derived material properties obtained using these methods.

Chapter 4 describes the experimental setup used in this research as well as the simulation techniques used. The method for data collection is described and the data processing techniques are detailed.

Chapter 5 describes the methods and details of the simulations performed as well as the model parameters that were varied for each simulation.

Chapter 6 presents the results of the experimentation as well as their comparison to the simulated results obtained from the finite element model.

Chapter 7 summarizes this results determined from this thesis and presents suggestions for future work in this research area.

CHAPTER 2: Review of Additive Manufacturing

2.1 AM Overview

Additive manufacturing comes in many forms and is commonly referred to as 3-D printing. AM offers a wholly new design space without constraints of traditional manufacturing methods (3-5). Also known as Free-Form, AM produces parts from a bottom-up methodology rather than a top-down approach. Generating parts by adding material layer-by-layer, AM presents the opportunity to create geometries that would otherwise be impossible or cost-prohibitive to manufacture. AM can produce well-integrated designs and structures, single parts with functions of multi-part assemblies as well as fully-optimized and organic geometries. These features of AM have been driving the progression of the field since its inception and with the continued development of the supporting technologies, driving its adoption into mainstream manufacturing (1).

3-D printing has been around since the late-80's, originating with stereolithography (SLA) which produced 3-dimensional models by curing photosensitive resin with ultraviolet light in a layer-wise fashion. Fused deposition modeling (FDM) followed soon after, using extruded thermoplastics. In general, a filament is forced through a nozzle that is heated to the melting temperature of the material, extruding a thin thread of material and depositing onto the previous layer, fusing as the material cools and thus solidifies. Each layer of the model is deposited in the manner until the complete model is formed. FDM has become the most common consumer form of additive manufacturing with complete systems available for well under $1000 USD (4). Selective Laser Sintering (SLS) or Selective Laser Melting (SLM) are the most common AM techniques to produce metallic parts. These processes utilize powdered metal that is melted or sintered by a laser in a pattern determined by the CAD geometry and software system. SLS and SLM parts are also

generated layer-by-layer, innately similar to the processes described above. While each AM method has unique characteristics, they have a common basis of building a 3-D part by stacking multiple "2-D" layers one on top of the other until the desired geometry is produced. This layer-by-layer process is the basis for all AM techniques, each with variations in the deposition as necessary for the differing materials. For metals, this process is performed using powdered metal media that is spread in a thin, planar layer that is selectively sintered, or melted. Again, each layer is built upon the previous layer until a complete 3-dimensional structure is realized. This is commonly referred to as a powder bed system. This powder bed system is also used for polymers and ceramics, where as opposed to a laser or electron beam binding the powdered material, a liquid binder is deposited onto the powder layer to create each layer of the 3-D part. This has been traditionally referred to as Three-dimensional printing because of the use of inkjet print heads to deposit the binder material, but the term 3D printing has recently been generalized to blanket all types of AM.

The parts used in this thesis research were manufactured using Direct Metal Printing (DMP), which is more commonly known as Selective Laser Melting (SLM) or Direct Metal Laser Sintering (DMLS) on a powder bed system. In this process, powdered metal is spread across a build plate in a thin, uniform layer, generally on the order 10-100μm thick. A laser is then directed across this powder layer in a pattern determined by computer-aided design tools and the powder is selectively melted. Upon completion of each layer, a fresh layer of powder is spread across this newly melted pattern and the next pattern layer is melted into the previous layer. This process is repeated for each slice of the CAD geometry until the full part is constructed and a fully-dense, metallic part is generated. The un-melted powder

is removed from the part, sifted and recycled back through the process during the next build. A diagram illustrating the process is shown below in Figure 1.

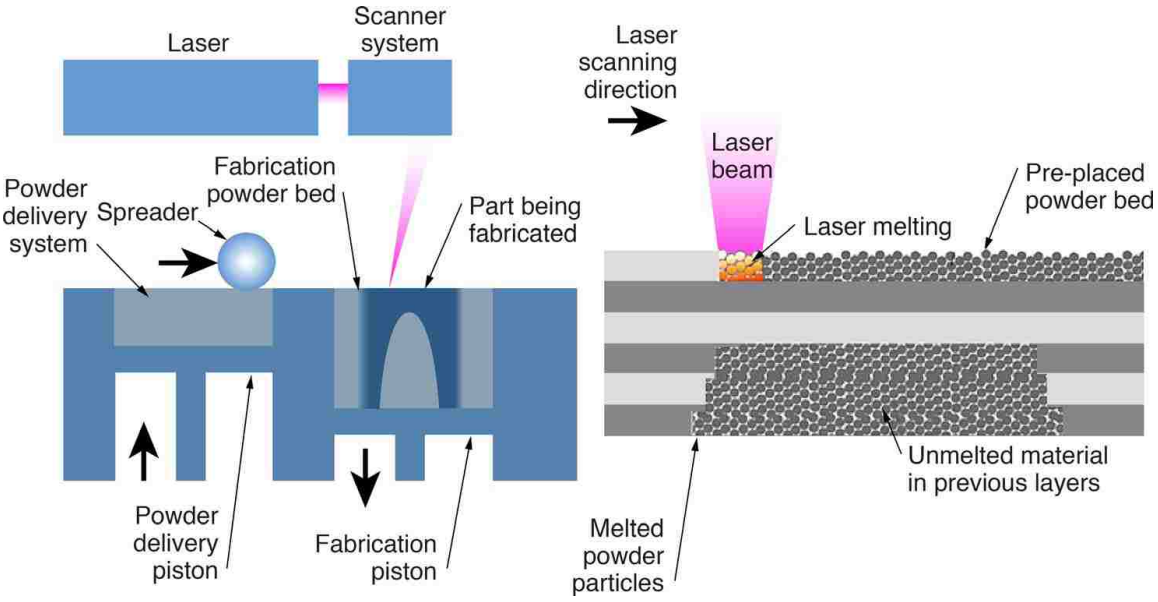

Figure 1 – Diagram of typical laser-sintered powder bed AM process, (12)

This process can produce part densities upwards of 99%, depending on powder particle size and manufacturing parameters. There has been extensive research done with regard to the microstructure generated during this melting and solidification process (22). While the microstructure has direct correlation to the material properties, it remains difficult to predict the bulk properties of the functional part. Many characteristics have influence on the functional properties of AM parts, including homogeneity, surface finish, part geometry, as well as the anisotropies inherent to the stereolithographic construction. The uncertain nature of AM parts is the driving force behind this research.

2.2 Knowledge Gaps in AM

While much focus of research on the progression of AM is on the process parameters and the microstructure of metallic parts produced, these techniques do not immediately translate to parts on the macro scale (23). The behavior of AM parts as a whole is currently unpredictable, and in high-consequence applications, this uncertainty is unacceptable (3). In addition, the types of material testing that is applicable to AM that can be adopted from wrought materials testing needs careful consideration (20). Monitoring the process parameters throughout the duration of the manufacture of a part aims to predict part imperfections and microstructure throughout the part, but these techniques are inherently expensive and require computationally exhaustive simulations including in-process feedback systems. While this may be the distant future of born-qualified AM parts, a near-term solution is needed to accelerate the widespread acceptance of functional, as-printed AM parts. Much research is focused on the qualification of AM material, both pre-processed (24) as well as the as-printed material (25). In parallel, there are many efforts aimed at adopting characterization techniques from experience in wrought material and subtractive manufacturing. This is the natural thought towards qualification, but as these are generally performed on material lots, the translation to AM is not direct, as the material is essentially cast grain by grain. These efforts do provide valuable data, but many of the tests are destructive, such as tensile and hardness tests, thus they are performed on representative samples, and do not translate directly to the qualification of as-printed functional parts. The development of this research aims to progress the use of MFT to allow for direct qualification of as-printed AM parts.

2.3 NDE techniques

With the current level of confidence in AM processes, the qualification of as-printed AM parts requires extensive testing of representative parts, and many tests are destructive in nature. The appeal of non-destructive testing is the ability to obtain data without the degradation of the unit under test. This not only allows for the use of the component post-test, but also lends itself to amassing many data points to develop a statistical dataset to better present the part performance. Some non-destructive evaluation techniques include CT-scanning and X-ray imaging to observe the interior structure of a part and ultrasonic testing to detect imperfections or cracks within a part (21,26-29). These methods are better labeled as inspection techniques rather than evaluation techniques, as they are passive in nature and merely help to identify defects in the structure of the part. The use of resonant frequency in both material property determination and defect detection has been used successfully for wrought and cast materials (30-33). The use of modal analysis in the case of the MFT used in this research allows for the non-destructive characterization of material properties through modal frequency analysis and comparison to validated computer models. This comparison to validated computer models allows for the evaluation of the highly complex geometries that are facilitated by AM. By comparing the experimental data to these predictive models, the functional material properties are determined within a region of interest, and insight is gained into the expected performance of the AM parts.

The non-destructive nature of these tests coupled with the determination of functional bulk material properties is a primary driving factor in this research. The ability to collect the relevant data without any influence on the integrity of the part allows for the test to be performed multiple times, including before and after certain post-processes like tempering

or annealing. Also, the applicability to complex geometries opens a wide range of functional tests to validate AM parts prior to their actual use. By quantifying the potential accuracy of the MFT with respect to AM parts, the qualification and acceptance of AM into high consequence applications will be one step closer to reality.

2.4 Characterizing/Qualifying AM

In any high-consequence application, the surety that each component will perform as expected is paramount. Many of these applications reside in the aerospace and defense sectors where confidence must be absolute, with huge budgets and potentially human lives at stake. A competing priority to confidence in these industries, but just as important to the success of the mission is the minimization of weight. The ability to reduce weight and potentially number of parts by integrating multiple function through the use of AM are driving the design space within these critical industries, and thus creating a highly vested interest in AM. While AM currently offers the capability to revolutionize the available design space, it can only do so with robust qualification efforts that verify and validate the performance of these complex geometries produced by AM (34).

The dimensional accuracy of AM parts is becoming increasingly accurate, as these properties are relatively easy to verify using a number of well-known techniques including coordinate measurement machines (CMM) coupled to nominal CAD geometry. The ability to measure the complex and often organic shapes produced with AM is key to the qualification, but is only a piece of the puzzle. While dimensional accuracy is important, the bigger mystery within AM is the behavior of the material beneath the surface. With wrought material, the uniformity across lots of material has been tightly characterized for hundreds of years and is guided by many standards that provide the confidence that a billet

part will perform as expected. This in depth understanding of material behavior does not yet exist in the world of AM, and thus the confidence in parts made with AM does not meet the needs of many applications.

While some alloys are more adept to use with AM processing (35), practically every alloy in use with sintered AM processes have differing properties between their wrought counterparts. These differences are not necessarily negative, with some properties actually being more desirable in comparison (36,37). Understanding these differences are key, as deltas between similarly identified materials can create distrust in a particular process that may not be inferior, merely mischaracterized. Research in this area suggests that identification of AM powder, which is based on what the powder is derived from, may require greater clarification, as differing phases are present due to the melting and solidification process.

In addition to the differing properties from the alloys' wrought counterparts, there are also identified anisotropies inherent to AM parts due to the stereolithographic nature. The orientation in which the part is manufactured relative to the build plane influences the effective performance of the part. Studies have shown distinct differences between vertically oriented tensile bars versus horizontal orientation, particularly with 316L stainless steel (38,39). The consistency and surface finish has also shown a distinct effect on the functional properties and integrity of AM parts. The surface finish, influencing the stress concentrations at the part surface can have a large effect on behavior, particularly shown during tensile testing (40). A similar effect has been shown when studying the behavior of porous materials (41). While many laser-sintered AM processes show very high material density, the voids that can behave similarly to porous materials if they are in

a high enough concentration. Understanding these differences in material structure due to the processing parameters such as anisotropies, internal voids or potentially porous material, and surface finish inconsistencies or anomalies is key to understanding the behavior of parts produced using AM. While many of these effects may not be readily identifiable at the micro structure level, they have a macroscopic influence that needs to be characterized at the functional part level for qualification of AM.

CHAPTER 3: Modal Frequency Method

The use of mechanical vibrations has been extensively applied throughout mechanical engineering for evaluation of product performance. There are also several instances of its use in identifying the characteristics of AM parts, particularly silicon wafer fabrication of micro-cantilevers (42). Modal frequency determination is a popular non-destructive evaluation technique primarily used for comparative quality control, but its application to metallic AM parts to specifically determine material properties has yet to be exploited. While Young's modulus can be determined through more traditional destructive techniques such as tensile or compression testing, these quasi-static methods generally do not produce as accurate of results when compared to dynamic methods. The resonant vibration of a part can be observed well below the elastic limit of the material, thus providing the necessary information without damaging the material, hence non-destructive. Some of these dynamic methods include the physical vibrational displacement measurements that will be used in this experimentation, commonly referred to as bar resonance (42-46), as well as ultrasonic propagation methods using ultrasound pulse-echo to determine the resonance of a material commonly referred to as resonant ultrasonic spectroscopy (26-28). With the increasing interest in AM, these novel qualification techniques are also garnering increased interest, hence the basis for this research.

3.1 Analytical Model

The coupons used in this research were designed based on the coupons used in nano-tribometry, which utilize series of cantilever beams to support contact points for friction studies. These generally do the reverse calculations that will be done herein in order to determine the force required to displace a set of known cantilevers a measured distance. This unique geometry lent itself well to the Young's modulus determination due to the

utilization of a simple cantilever, which can be described analytically. While the constraints of the cantilever configuration of the AM coupons are more complex, the basic theory below generally applies, and the concepts are the same.

The simplified geometry of a rectangular bar with known dimensions fixed at one end (y) and free on the other (along x) is shown in Figure 2.

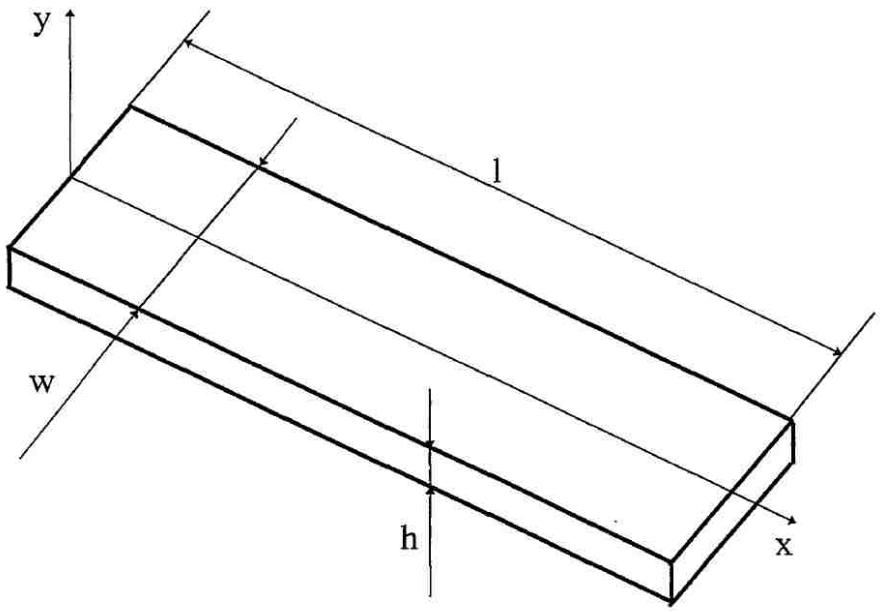

Figure 2 – Simple Rectangular Cantilever Beam, Fixed-Free (42)

With E representing the Young's modulus of the material, A the cross-sectional area of the beam, I the area moment of inertia, ρ the density and assuming isotropy and homogeneity, the equation of motion of the cantilever is given by equation 1:

$$EI\frac{\partial^4 y}{\partial x^4} + \rho A\frac{\partial^2 y}{\partial x^2} = 0 \qquad \text{(Eq. 1)(42)}$$

The solution of this 4th order differential equation is:

$$y(x,t) = y(x)[\cos(\omega_n t + \theta)] \quad \text{(Eq. 2)(42)}$$

The natural frequency f_n of the beam subject to flexural vibrations can be described by equation 3:

$$f_n = \frac{\lambda_n^2}{2\pi l^2}\sqrt{\frac{EI}{\rho A}}, \; n = 1,2,3, ... \quad \text{(Eq. 3)(47)}$$

Where n is the vibrational mode. λ is the modal eigenvalue for the system, which can be determined by experimentally measuring the resonant frequencies. By rearranging the equation to solve for E:

$$E = \frac{4\pi^2 l^4 f_n \rho A}{\lambda_n^4 I} \quad \text{(Eq. 4)(47)}$$

Using the ANSYS modal simulation software, these equations were solved for a sweep of parameters using the exact CAD geometry for the coupons used herein. These parameter sweeps produced a series of values for E, Young's modulus, for each parameter set. Based on the measured natural frequency, the measured density, ρ, and the known coupon dimensions, the appropriate value of E for each coupon can be interpolated.

3.2 Frequency Domain

To measure the natural frequencies of each coupon, the vibrational response, generally the displacement of a particular portion of the specimen is observed. In the case of this research, a laser Doppler vibrometer was used to measure the velocity of the nose of the coupons. The velocity of the coupon nose is measured in time. While this time domain data

contains all of the desired information, extracting the particular frequencies requires a transformation into the frequency domain. Once the data is transformed into the frequency domain, the frequency values of the signal are binned, such that the most observed frequencies (natural frequencies) dominate all others. The peaks of the frequency domain signal indicate the frequency of the resonance, and thus allow for the distinct identification of the natural frequencies of the unit under test.

Using MATLAB to process the raw time domain data, the signal was easily transformed into the time domain. With the functions included in the MATLAB Signal Processing Toolbox, the following simple script was used:

```
t_length=length('insert raw time domain signal here');
%Measures the length of the time domain signal

NFFT=2^nextpow2(t_length);
%Pads the time domain signal with zeroes such
%that the total length is a power of 2 multiple

signal_fft=fft(Pt5mmflat1run1,NFFT)/t_length;
%Takes the Fast Fourier Transform of the padded
%time domain signal

fs=2e6;
%Sample rate used to acquire time domain signals

f=fs/2*linspace(0,1,NFFT/2+1);
%Establishes frequency bins from 0 to half the
%sampling frequency

fft_narrowed=2*abs(signal_fft(1:NFFT/2+1));
%Modifies the fft from the complex conjugate form
%to positive real values. Multiple of 2 accounts for
%amplitude absorbed by other half of complex conjugate

plot(f,fft_narrowed);
%Plots fft values against frequency bins
```

Additional information and figures displaying both the time domain and frequency domain signals will be shown later in this document.

CHAPTER 4: Experimental Setup

This chapter presents the experimental techniques used to generate the test coupons and the methods and hardware used for collecting the data from each test. Figure 3 below shows the process flow for coupon design, data collection, processing and comparison.

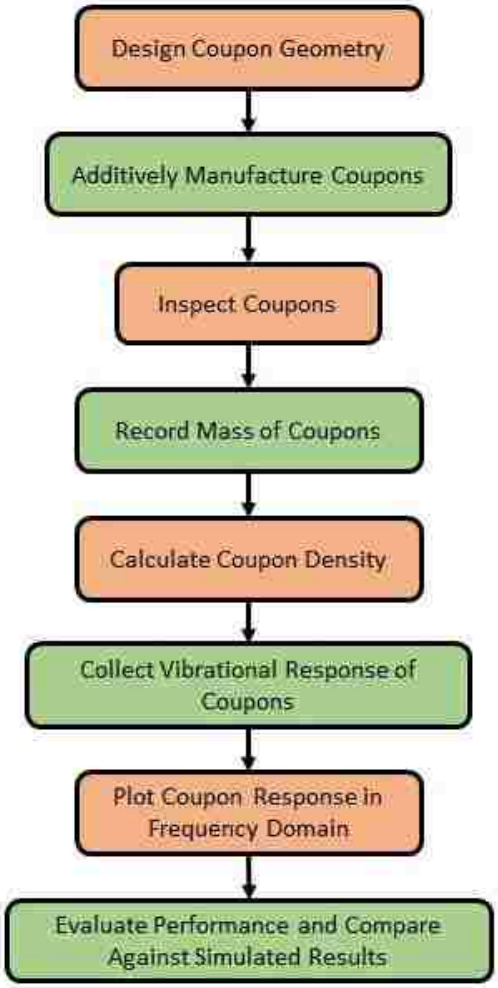

Figure 3 – Experimental Flow Chart

4.1 Coupon Design

The coupon design was intended to provide a means for relatively simple measurement of modal frequencies from a series of cantilever beam thicknesses. The basis for the design was derived from tribology experimentation hardware. Tribology coupons, as shown in Figure 4, are essentially a bi-axial set of calibrated cantilever beams. This novel geometry

lends itself well to additive manufacturing, as the complex shape and thin features are difficult to manufacture using traditional methods and currently require multiple piece-parts to be assembled.

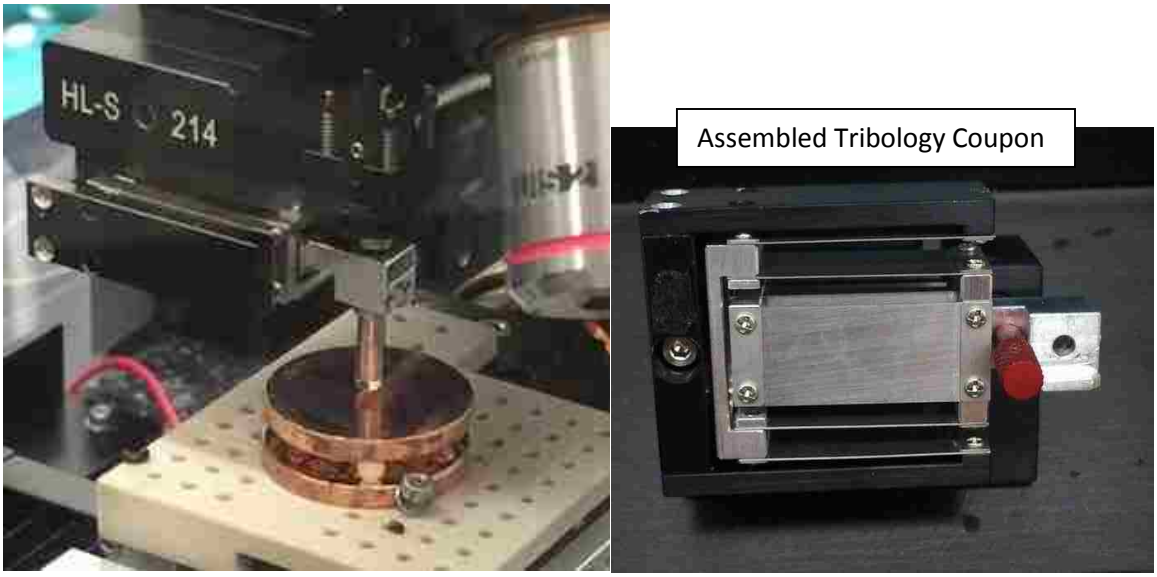

Figure 4 – Ball-on-slab Tribology Test setup (note cantilever-beam pin support coupon)

Ball-on-slab tribology experiments aim to measure the frictional force between a ball and slab material, and the series of cantilever beams provide a means to measure the very sensitive displacement of the ball generated under these sliding conditions. From this displacement and the known geometry and stiffness of the cantilevers, the force needed to displace the cantilevers can be calculated. Sensors are aligned along the two axes of interest that facilitate an accurate measurement of the normal axis displacement and the frictional axis displacement created by the sliding friction interaction. With these two measurements and the known cantilever variables, the coefficient of friction for the sliding interaction can be characterized. These systems are designed to allow for the observation of very minute

details of the interaction, such as stiction and surface roughness interaction. These high-resolution measurements along perpendicular axes coupled with the unique cantilever design were drivers in the design of the coupon used in this research. While the intent of this thesis is not related to friction experiments, the hardware geometry has unique characteristics that lend themselves to the modal techniques for material property characterization for additive manufacturing.

The coupons for this experiment were designed similarly, with a series of cantilevers that deflect along a single axis. To simplify the scope of this thesis, the coupons were designed with only a single displacement plane, but retain a similar geometry to the tribology coupons such that subsequent experimentation could evaluate multi-plane coupons. Coupons were designed with differing cantilever thicknesses in order to help more broadly characterize the properties of the printed material. The varying thicknesses also allow for the observation of any differing properties between "wall" material and "body" material. The "wall" material is the material that composes the exterior walls of the component while the "body" material is that which is internal to the part. The material that solidifies along the exterior walls may harden at a different rate than that within the interior of the part, thus creating the potential for additional anisotropies. To address these concerns, coupons with cantilever thicknesses varying from 0.5mm to 2.5mm in 0.50mm increments were tested and analyzed. Figure 5 shows the suite of coupons designed in SolidWorks with the varying cantilever thicknesses along with the printed coupons of varying cantilever thicknesses.

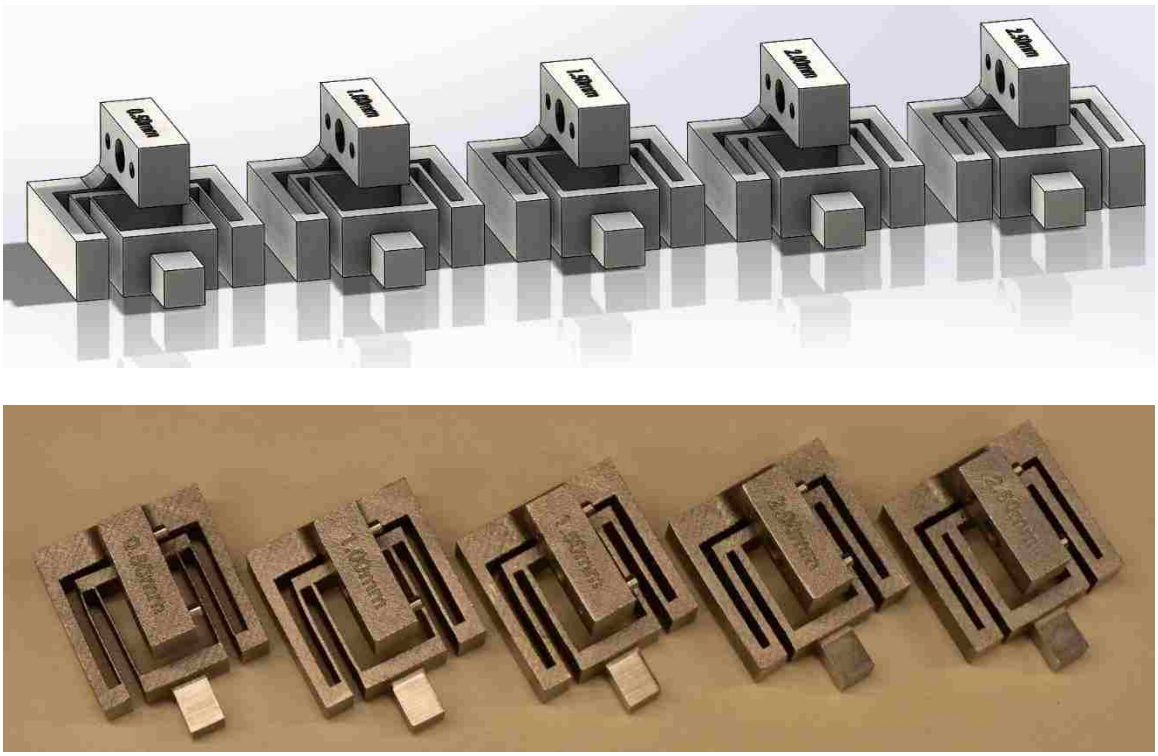

Figure 5 – CAD-designed Coupons (top) and as-printed DMLS 316L Coupons

4.2 Coupon Manufacture

Coupons were manufactured from 316L stainless steel using additive processes. The particular AM technique used in the manufacture of the coupons is known as DMLS, or Direct Metal Laser Sintering. This process is described in more detail in a previous chapter. The parts were sourced from Proto Labs, Inc. out of Maple Plain Minnesota. The build specifications as quoted from Proto Labs were normal resolution, which correlates to a layer thickness of 30 microns (0.0012") with a minimum feature size of 0.380mm (0.015"). Typical tolerance expectations are +/- 0.076mm (0.003") with an additional 0.001mm/mm expected. Surface finish, though not explicitly measured for this experiment, is typically on the order of 200-400µ-inch Ra. Advertised material properties follow the AMS5653H SAE specification. Coupons were printed in different orientations to help in characterizing anisotropies induced by print orientation. Coupons were printed in the traditional "flat"

orientation and also printed at a 45-degree angle or “diagonal” orientation as shown in Figure 6. In the image of the as-printed coupons, the striations generated while printing in the 45-degree orientation can be seen, and were the primary means for differentiating the two print orientations. The 45-degree orientation was chosen to provide an additional orientation while allowing for manufacture without the use of support material. As current additive manufacturing is a layer-by-layer process, there is concern about the parts produced having directionally biased material properties. These multiple orientations aim to characterize the anisotropies induced in these particular coupons.

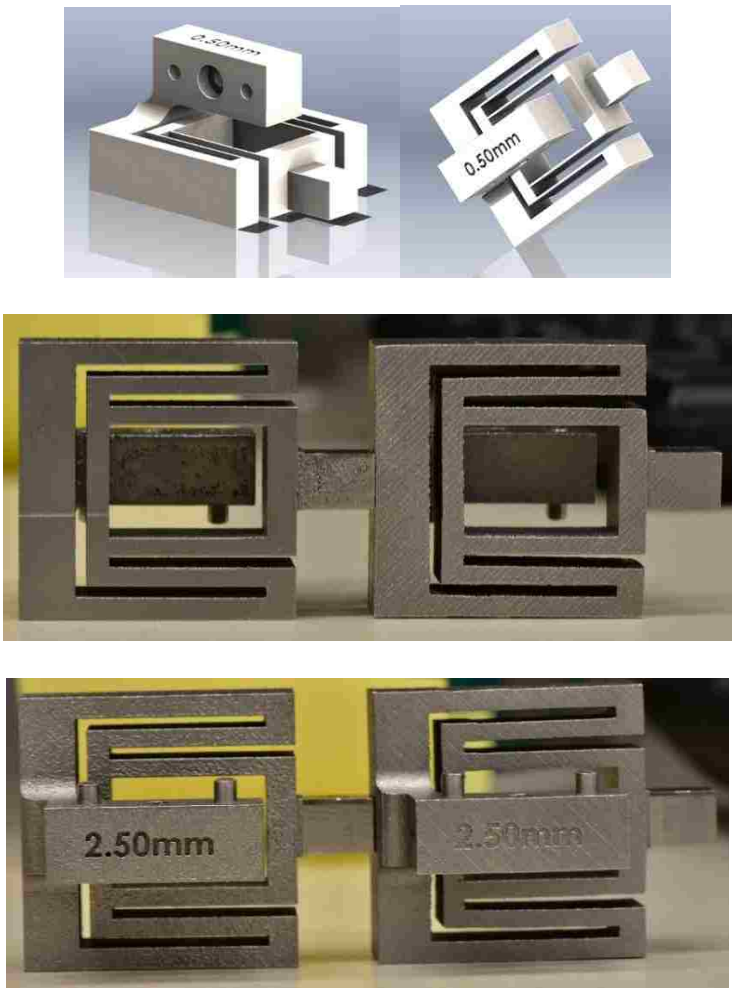

Figure 6 – Coupon Orientation Identification (note striations generated by angled print orientation (right)

Characterizing the anisotropies inherent to AM is very important to the qualification and acceptance of high-consequence functional AM components. Through the testing of the multiple cantilever thicknesses and the differing print orientations, qualitative statements can be made about the properties of these AM coupons in addition to the focus on the evaluation of the modal frequency techniques for material property characterization. The suite of coupons examined are pictured in Figure 5 and identified in Table 1.

Cantilever Thickness	Print Orientation	Quantity
0.5mm	Flat	5 pc
0.5mm	Angled	5 pc
1.0mm	Flat	5 pc
1.0mm	Angled	5 pc
1.5mm	Flat	5 pc
1.5mm	Angled	5 pc
2.0mm	Flat	5 pc
2.0mm	Angled	5 pc
2.5mm	Flat	5 pc
2.5mm	Angled	5 pc

Table 1 - Coupon Types

4.3 Test Theory

As described previously in more detail, a commonly used method for non-destructive materials characterization is known as the modal frequency technique. This technique uses the natural resonant frequencies of the unit under test to determine the state of health of the component, or to determine some other unknown property of the part. All physical things resonate at particular frequencies. These frequencies are dependent upon the known geometry of the part, the measurable mass and density of the part and the unknown stiffness of the material of which the part is made. Using the known and attainable information about the coupons, the unknown Young's modulus, or stiffness, of the coupon can be determined by matching the modal results to a model.

The parameters of the coupon are measured using traditional laboratory techniques. The mass of the coupons is collected using a calibrated digital benchtop scale. The density is measured using the mass of the part and the volume calculated by measuring the buoyant force exerted on the coupon when it is submerged in a known fluid using the Archimedes principle. The dimensions of the coupons were confirmed using digital image processing. The coupons were scanned along with a gauge block for calibration using a high-resolution scanner, and the images were processed using MATLAB image processing to measure the thickness of the cantilevers. Figure 7 shows an example of the digital image measurements. Upon inspection of several coupon dimensions, there was minimal deviation from nominal dimensions, and thus for subsequent calculations, nominal cantilever dimensions were assumed throughout this study.

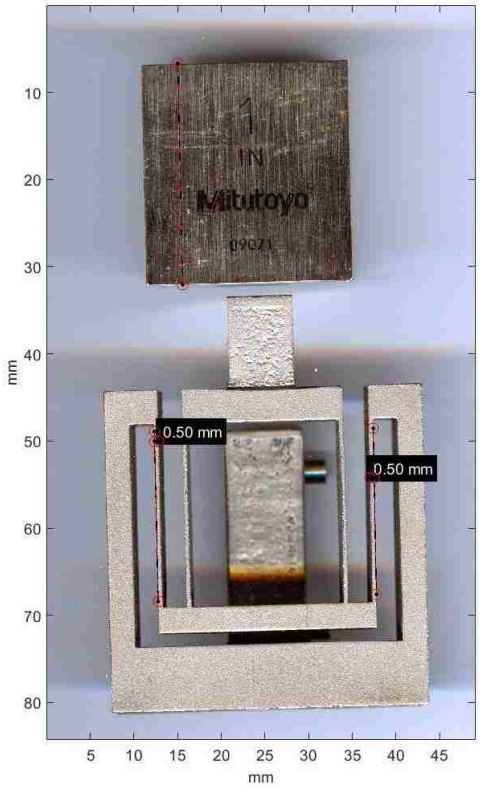

Figure 7 – Digital Image Correlation Measurement

For the experimentation of the cantilever coupons, the vibrational response to an excitation is observed and recorded. This time domain vibrational response is converted to the frequency domain, where particular resonant frequencies can be more easily observed graphically. With these particular resonant frequencies identified, one can begin to correlate the resonance to a particular mode shape, and ultimately determine the material properties that would produce these modal frequencies based on FEA simulation for a given part geometry and measured physical properties.

4.4 Density Measurements

The density of the material has a significant effect on the modal response, particularly because of the influence of the mass contribution. Density is also an area of interest with regards to AM material and the parts that are produced. Because metallic AM parts are generally produced from sintering loose powder, the potential for less than 100% dense material is increased. To accurately measure the density of the coupons, the Archimedes principle was used. This provides a means to easily take very accurate volume measurements that, in conjunction with mass measurements, can provide the bulk density values for the coupons. Each coupon was weighed using a Mettler-Toledo digital scale with precision to 0.001g. The coupons were then submerged in deionized (DI) water and the mass of the coupon with the buoyant force included was measured. This was done using the Archimedes buoyant force fixture pictured in Figure 8.

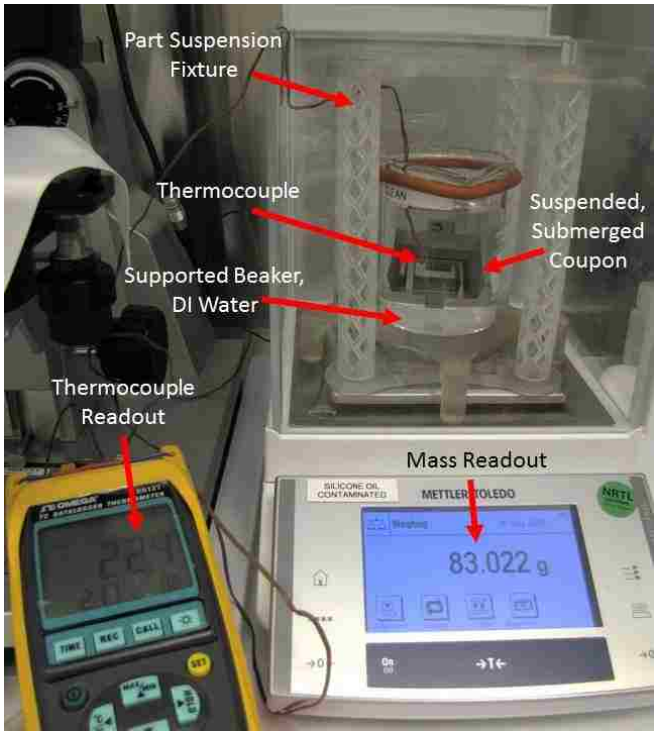

Figure 8 – Archimedes Bouyant Force Measurement Setup

The temperature of the DI water was recorded for each measurement to provide greater accuracy to the density of the water. With the density of the water known, and the buoyant force found by subtracting the submerged weight from the dry mass, the volume of the coupon can be found by calculating the amount of water that was displaced. The simple equation to determine the bulk coupon density is shown Equation 5:

$$\boldsymbol{Bulk\ Coupon\ Density\ = Density\ of\ DI\ Water\ \times \left(\frac{Mass\ of\ Coupon}{Buoyant\ Mass}\right)} \qquad \text{(Eq. 5)}$$

4.5 Vibration Test Fixture

Testing was performed using the custom fixture shown in Figure 9 as a rendered CAD image. Preliminary tests were performed using the tribology hardware, including the capacitive displacement sensors and the piezo-stages. These provided good results for the thinnest cantilever thicknesses, but as the thickness and consequently the stiffness increased, the stages were deflecting in conjunction with the coupons. The range of the

capacitive displacement sensors also limited the scope of experiments that could be performed using the tribology fixturing. In order to facilitate the deflections of the stiffest coupon cantilevers, the fixture needed to be much stiffer than the cantilevers to prevent the introduction of additional frequency response into the measured excitation. The custom fixture included a stainless steel mounting block attached to a 2-axis positioning stage to allow for precise positioning of the coupon nose in relation to the plucking block. The plucking block, the contact point between the fixture and the cantilevers, was bolted to a slide stage, and engaged and disengaged by an air cylinder. All of this is mounted to a manual linear stage used to displace the cantilevers. To measure the response of the cantilevers, a commonly used non-contact measurement method was employed; laser Doppler vibrometry. The Polytec PDV-100 laser Doppler vibrometer (LDV) was mounted to a tripod and focused on the nose of the coupon using one of the recommended stand-off distances to accommodate the laser cavity length and thus align with the visibility maxima. For these tests, a stand-off distance of approximately 234mm was used. The complete test setup is pictured in Figure 10.

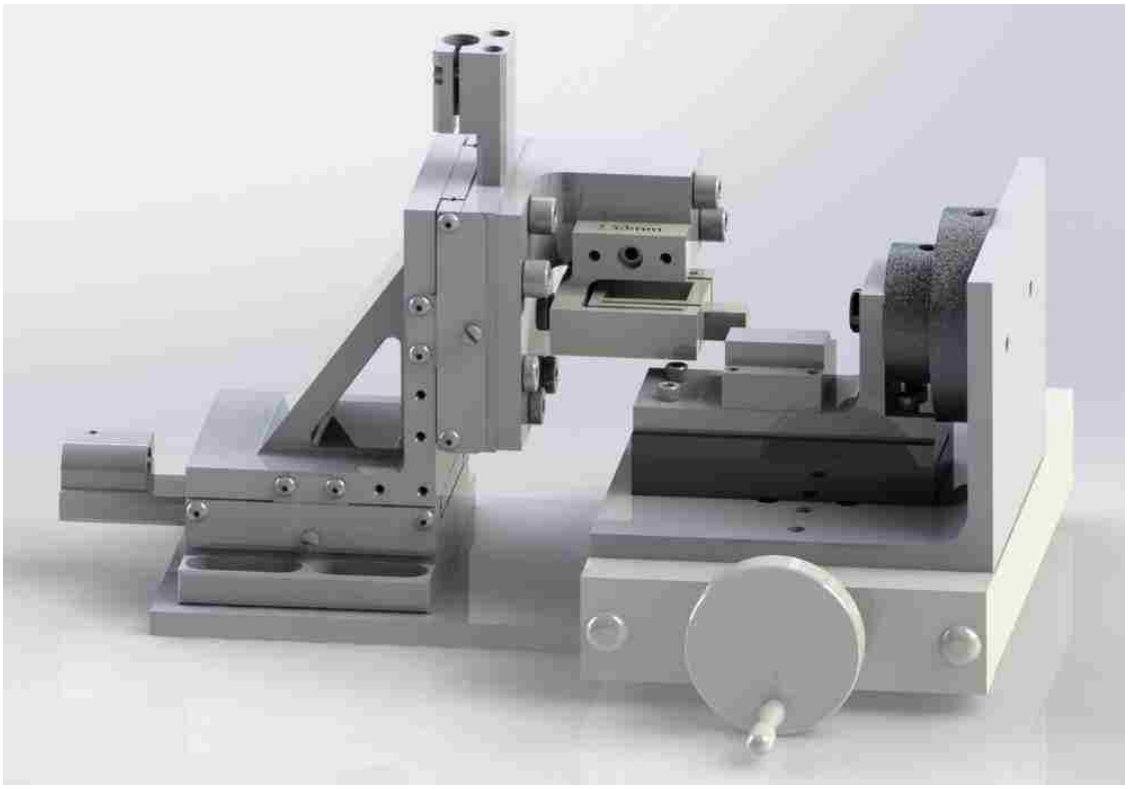

Figure 9 – CAD-designed Test Fixture

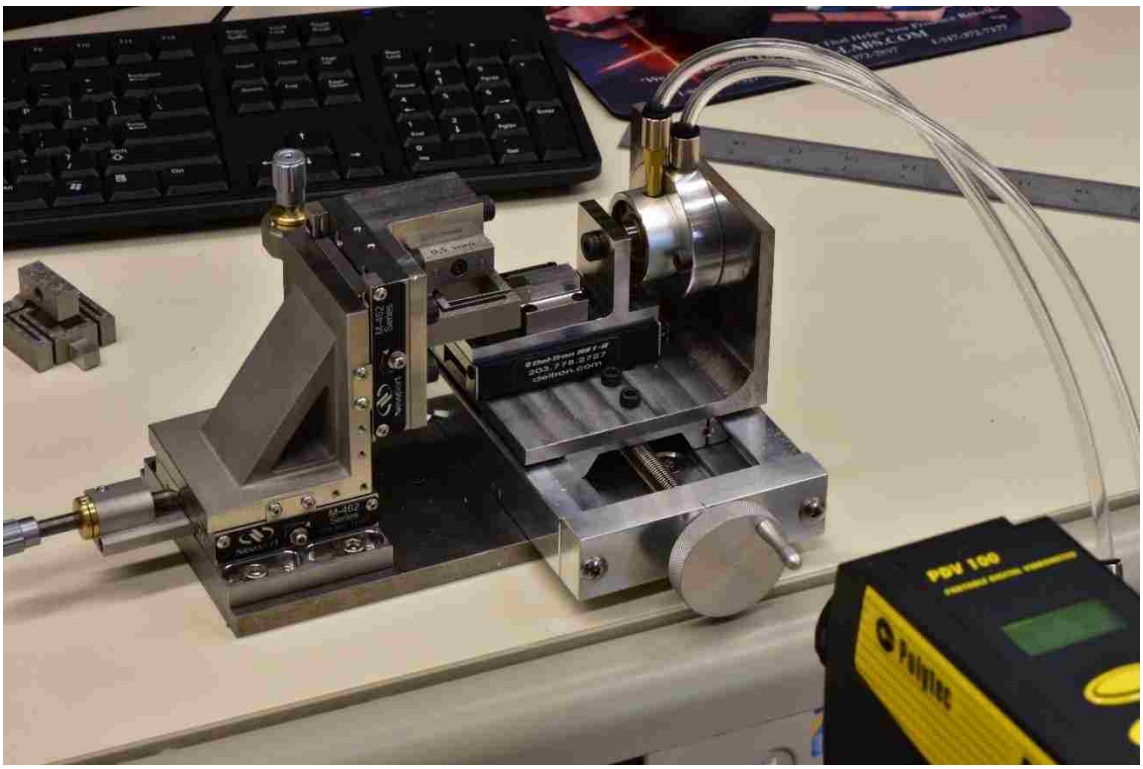

Figure 10 – As-tested Fixture, Coupon and LDV

To excite the cantilevers, the plucking block was brought into contact with the nose of the coupon. Using the manual linear stage, the cantilevers were deflected to a displacement that provided the largest velocity without over-saturating the LDV. The maximum velocity that can be measured with the PDV-100 is 500mm/s. determining the displacement to provide this maximum velocity was generally achieved within 2-3 trials.

4.6 Data Collection

Data collection was performed using standard data acquisition hardware and simple LabVIEW data acquisition coding. Utilizing the analog output of the LDV and connecting to both a digital oscilloscope for quick visualization of the data and the National Instruments USB-6363 data acquisition card for collection, each coupon was plucked and the velocity response at the nose of the coupon was measured. With the LDV set to the maximum velocity setting (500mm/s), each coupon was displaced a distance such that the initial velocity response once plucked was within range for the PDV to measure. This required some iterations utilizing the manual stage and the display of the oscilloscope to observe for any signal saturation. The displacement would be adjusted to balance maximum response without saturating the LDV. Examples of an acceptable measurement (full-time scale & zoomed) and a saturated measurement is shown in Figure 11, Figure 12 & Figure 13. Each coupon was tested multiple times to ensure specific behavior could be confirmed with subsequent runs. Data was collected at a sample rate of 2MHz. The duration of each dataset differed from 3 seconds for the 0.5mm thickness to 2 seconds for the 1.0mm thickness and finally 0.5 seconds for the remaining thicknesses of 1.5mm, 2.0mm and 2.5mm. Data was collected in .csv format and imported to MATLAB.

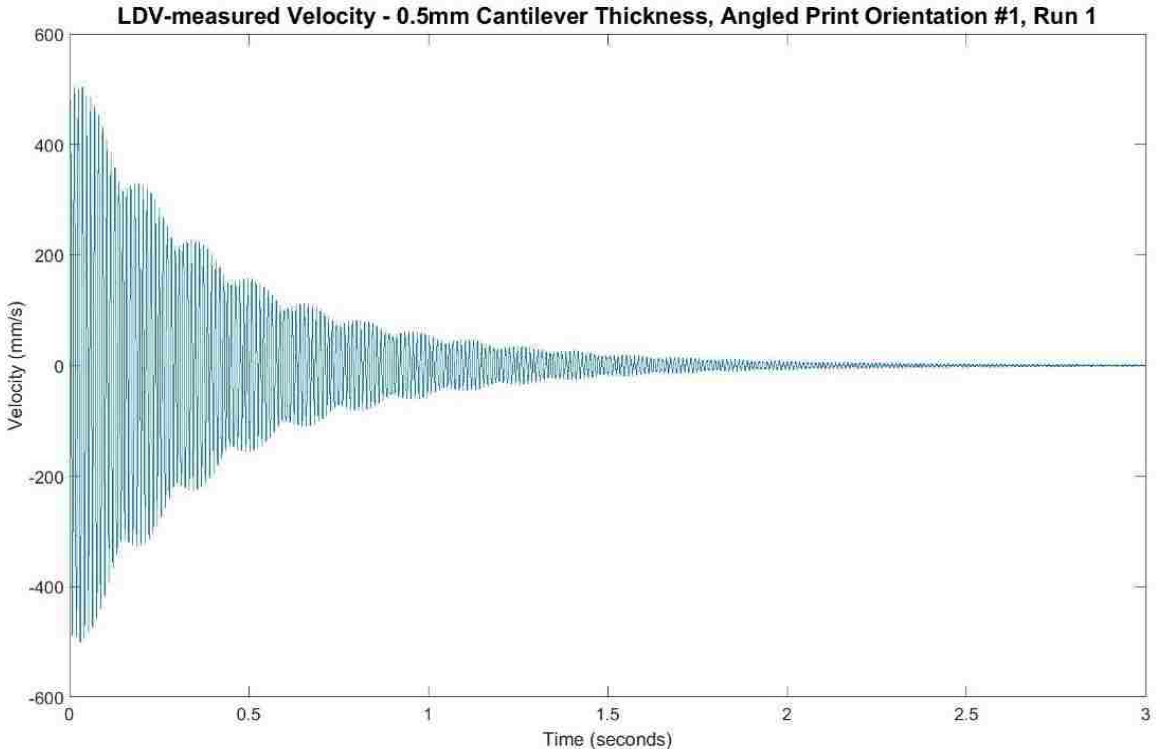

Figure 11 – Clean Time-Domain Velocity Signal Ringout – 0.5mm Cantilever

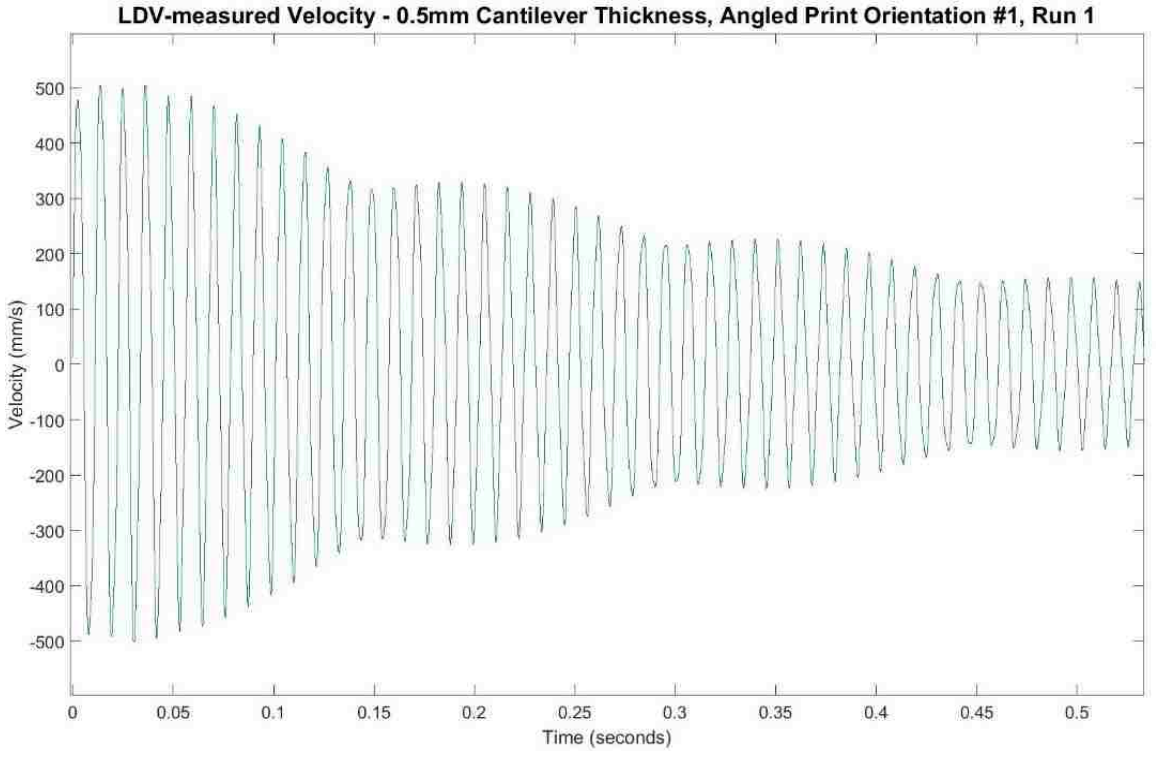

Figure 12 – (Zoom) - Clean Time-Domain Velocity Signal Ringout – 0.5mm Cantilever

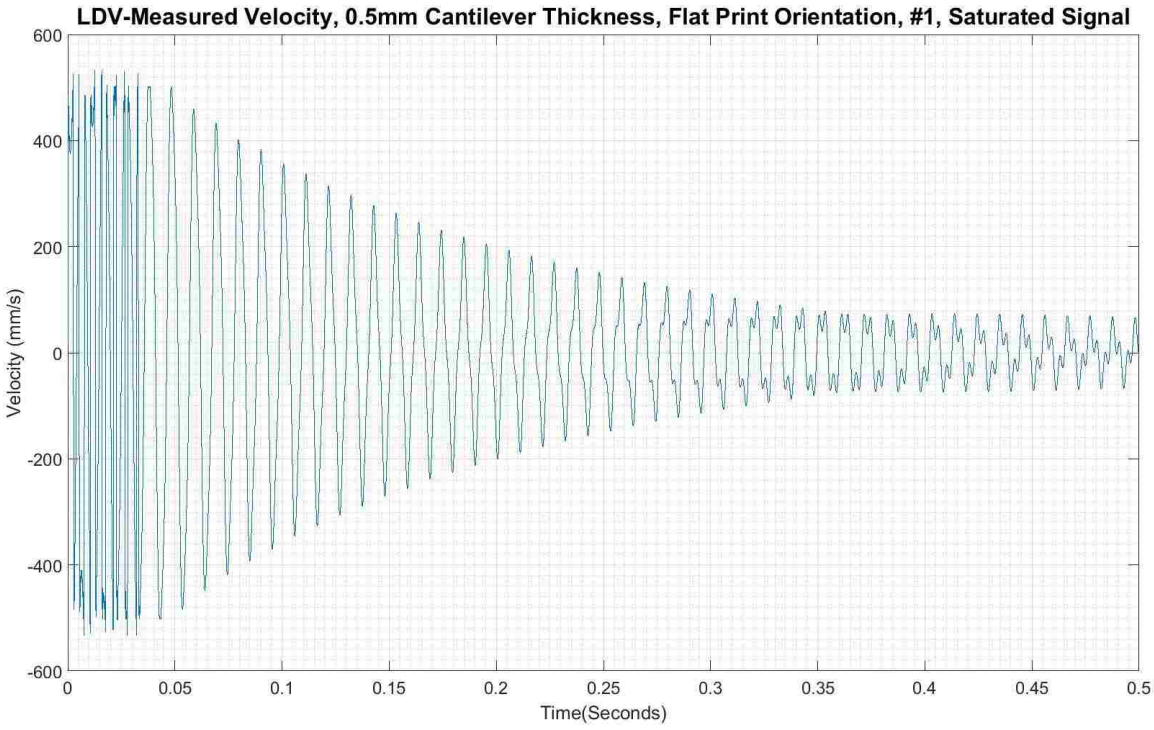

Figure 13 – Saturated Time-Domain Velocity Signal

4.7 Data Processing

The raw data collected via the data acquisition in a single column .csv format was imported into MATLAB for further analysis. Specifically, the time domain signal is converted to the frequency domain using a discrete Fourier transform, described in more detail above, and in this case the fast Fourier transform algorithm (fft) in MATLAB. The signal is decomposed into the specific frequencies contained within, and the magnitude of the frequencies contained are plotted. With a sample rate of 2MHz and expected resonance frequencies well under 1kHz, the fft was well-suited to this application. Figure 14 shows an example of the plotted results from the fft when performed on the time domain signal shown in Figure 11.

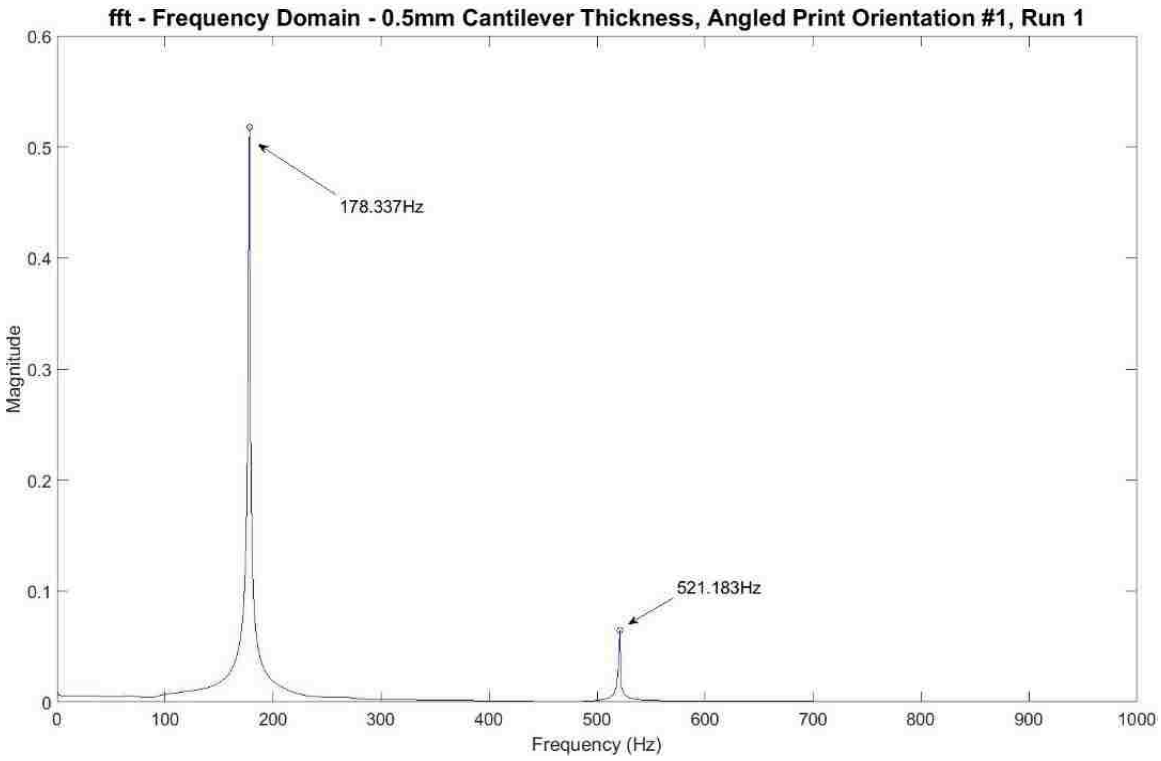

Figure 14 – Frequency Domain Signal with Modal Frequencies Identified

As can be seen, the resonant peaks are very distinct for this particular dataset. Each peak represents the resonant frequency for a particular mode shape. The frequency value for each peak of interest was also identified through software to precisely identify the peak amongst the spectral leakage. The fft results were plotted for each coupon as well as for each subset of coupons to allow for direct comparison between the individual runs on a single coupon as well as comparison across the set of coupons. This comparison across the subset of coupons can help to identify specific coupons that may have an internal defect or dimensional inaccuracy. Figure 15 & Figure 16 show examples of the fft data plots for the 0.5mm coupons printed in the angled orientation. The data plots for the remaining coupons can be found in Appendix A.4.

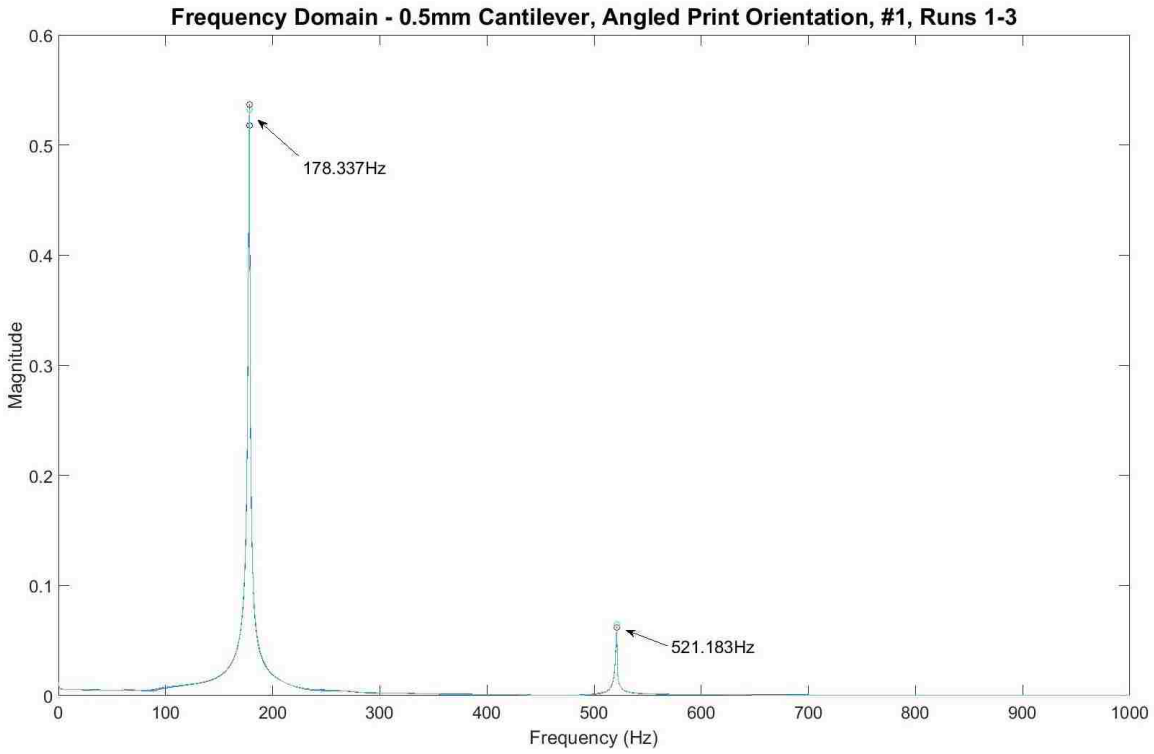

Figure 15 – Frequency Domain – 0.5mm Cantilever, Angled #1 Runs 1-3

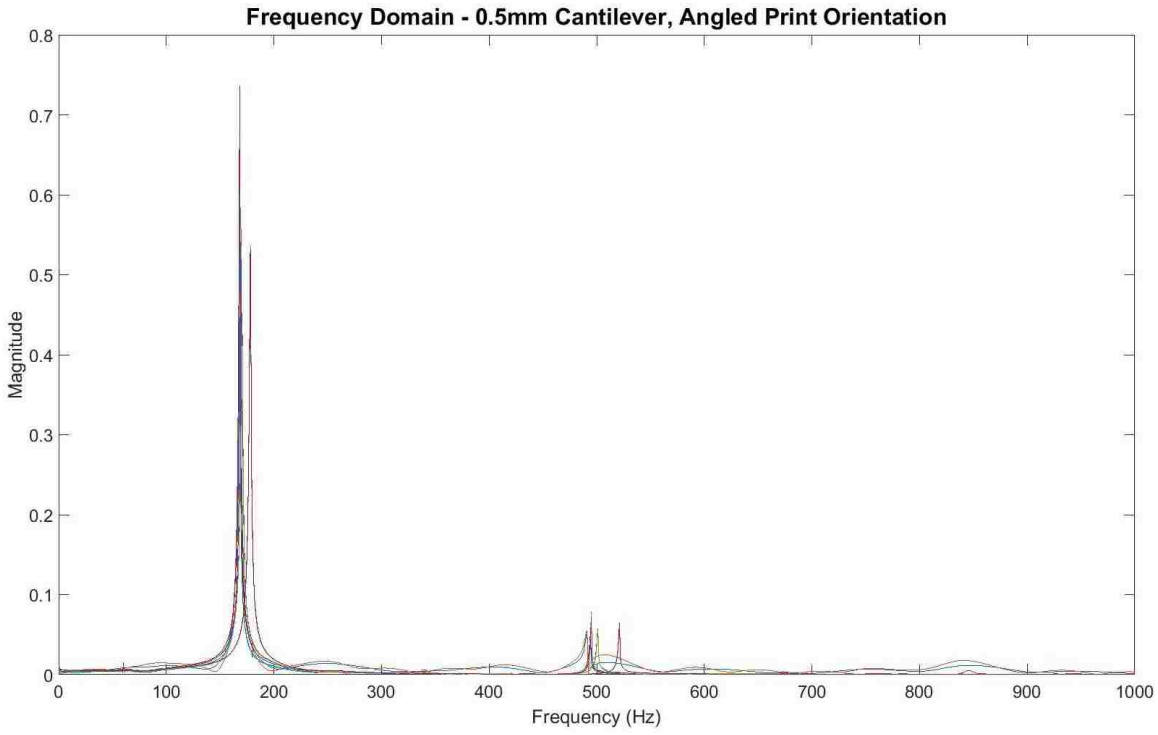

Figure 16 – Frequency Domain – 0.5mm Angled – All Cantilevers, All Runs

The combined plot in Figure 16 shows a tight grouping of the coupons both at the first modal frequency and second modal frequency, with a single outlier showing a higher resonance for both modes. This type of data can be used to identify defects in large populations of data, and can provide a means to cull unsatisfactory parts. For parts produced using AM, this could point to a variation in print parameters or material lot, a dimensional inaccuracy or defect within the part. Further analysis of the experimental data and comparison to simulated data is reported later in this thesis.

CHAPTER 5: Simulation Technique

5.1 Parameterization

In order to correlate the modal behavior of the coupons under test to a useable value for Young's modulus, a finite element model created using ANSYS 16.1 simulation software (ANSYS) and coupling with a SolidWorks parametric model. The coupon geometry was modeled with the thickness of the set of cantilevers parameterized such that the dimension could be swept between minima and maxima. Within the ANSYS workbench, the density and Young's modulus were also parameterized in order to simultaneously sweep through the variations that were expected within the additively manufactured coupons. Table 2 below shows the range of parameters that were used in the modal simulation.

	Units	Nominal	Minimum (-20%)	Maximum (+20%)	Delta	Step Size	# of Steps
Density	kg/m^3	7750	6200	9300	3100	79.487	40
Young's modulus	Pa	1.93E+11	1.544E+11	2.316E+11	7.72E+10	1.98E+09	40
Cantilever Thickness	mm	1.5	0.4	2.6	2.2	0.05	45

Table 2 – Simulation Parameter Ranges

By inputting these ranges of the parameters into the ANSYS simulation, each parameter could be swept against the other, allowing for each combination of circumstances to be simulated. The results from these parameter-sweeping simulations were used to correlate the measured modal behavior to the modal behavior of the simulated model, and from the overlap, the actual material properties extracted. The workbench setup is shown in Figure 17.

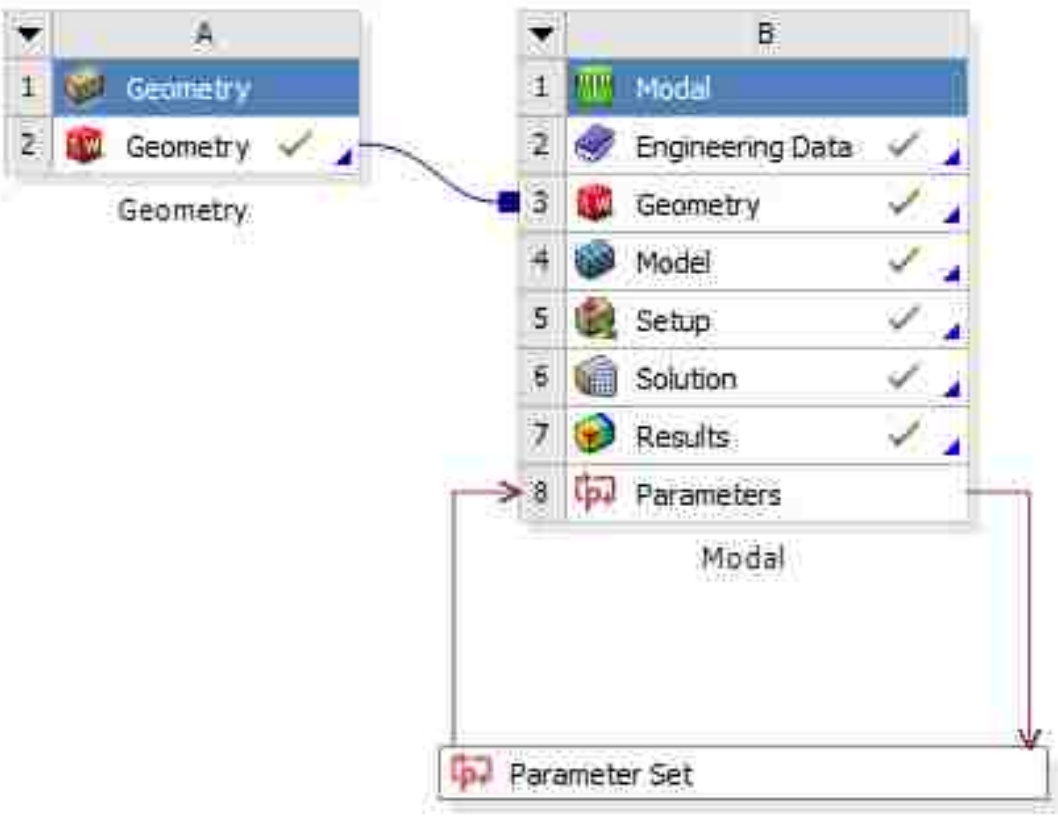

Figure 17 – ANSYS Workbench Configuration

The interface for configuring the parameterization of the model and simulation is shown in Figure 18. The range of parameters and the number of steps within each parameter range resulted in a large number of individual simulations that were able to run sequentially using this parameterized model and simulation technique. The particular parameter sets that were simulated are outlined in Table 2, showing the groups of parameters that were run together with the third parameter held at the nominal value. This grouping provided the most functional and presentable datasets.

Outline of All Parameters

	A	B	C	D
1	ID	Parameter Name	Value	Unit
2	Input Parameters			
3	Modal (B1)			
4	P1	Young's Modulus	1.544E+11	Pa
5	P8	Density	7750	kg m^-3
6	P12	DS_Leg@Sketch1@Parametric_Hollow_Coupon.Part	0.5	
*	New input parameter	New name	New expression	
8	Output Parameters			
9	Modal (B1)			
10	P3	Total Deformation Reported Frequency	227.9	Hz
11	P4	Total Deformation 2 Reported Frequency	669.73	Hz
12	P5	Total Deformation 3 Reported Frequency	1263.2	Hz
13	P6	Total Deformation 4 Reported Frequency	1755.6	Hz
14	P7	Total Deformation 5 Reported Frequency	1793.2	Hz
15	P9	Total Deformation 7 Reported Frequency	3085.1	Hz
16	P10	Total Deformation 6 Reported Frequency	2632.5	Hz
17	P11	Total Deformation 8 Reported Frequency	3467.2	Hz
*	New output parameter		New expression	
19	Charts			

Table of Design Points

	C	D	E	F	G	H	I	J
1	P1 - Young's Modulus	P8 - Density	P12 - DS_Leg@... .Part	P3 - Total Deformation Reported Frequency	P4 - Total Deformation 2 Reported Frequency	P5 - Total Deformation 3 Reported Frequency	P6 - Total Deformation 4 Reported Frequency	P7 - Total Deformation 5 Reported Frequency
2	Pa	kg m^-3		Hz	Hz	Hz	Hz	Hz
3	1.544E+11	7750	0.5	227.9	669.73	1263.2	1755.6	1793.2
4	1.5638E+11	7750	0.5	227.9	669.73	1263.2	1755.6	1793.2
5	1.5836E+11	7750	0.5	227.9	669.73	1263.2	1755.6	1793.2
6	1.6034E+11	7750	0.5	227.9	669.73	1263.2	1755.6	1793.2
7	1.6232E+11	7750	0.5	227.9	669.73	1263.2	1755.6	1793.2
8	1.643E+11	7750	0.5	227.9	669.73	1263.2	1755.6	1793.2
9	1.6628E+11	7750	0.5	227.9	669.73	1263.2	1755.6	1793.2
10	1.6826E+11	7750	0.5	227.9	669.73	1263.2	1755.6	1793.2
11	1.7024E+11	7750	0.5	227.9	669.73	1263.2	1755.6	1793.2
12	1.7222E+11	7750	0.5	227.9	669.73	1263.2	1755.6	1793.2
13	1.742E+11	7750	0.5	227.9	669.73	1263.2	1755.6	1793.2
14	1.7617E+11	7750	0.5	227.9	669.73	1263.2	1755.6	1793.2
15	1.7815E+11	7750	0.5	227.9	669.73	1263.2	1755.6	1793.2
16	1.8013E+11	7750	0.5	227.9	669.73	1263.2	1755.6	1793.2
17	1.8211E+11	7750	0.5	227.9	669.73	1263.2	1755.6	1793.2
18	1.8409E+11	7750	0.5	227.9	669.73	1263.2	1755.6	1793.2
19	1.8607E+11	7750	0.5	227.9	669.73	1263.2	1755.6	1793.2
20	1.8805E+11	7750	0.5	227.9	669.73	1263.2	1755.6	1793.2
21	1.9003E+11	7750	0.5	227.9	669.73	1263.2	1755.6	1793.2
22	1.9201E+11	7750	0.5	227.9	669.73	1263.2	1755.6	1793.2
23	1.9399E+11	7750	0.5	227.9	669.73	1263.2	1755.6	1793.2
24	1.9597E+11	7750	0.5	227.9	669.73	1263.2	1755.6	1793.2
25	1.9795E+11	7750	0.5	227.9	669.73	1263.2	1755.6	1793.2
26	1.9993E+11	7750	0.5	227.9	669.73	1263.2	1755.6	1793.2

Figure 18 – ANSYS Parameterization Configuration

5.2 Mesh & Constraints

A simplified geometry was used during simulations in order to reduce the computational time necessary to carry out the simulations. The area of interest was maintained, while the mounting snout was modified, as these modifications would not adversely affect the simulation accuracy. The mounting holes needed to affix the coupon to the physical testing fixture were removed from the CAD geometry. Figure 19 below shows the complete CAD model and the CAD model used during the ANSYS simulations with the mounting holes removed for simplicity.

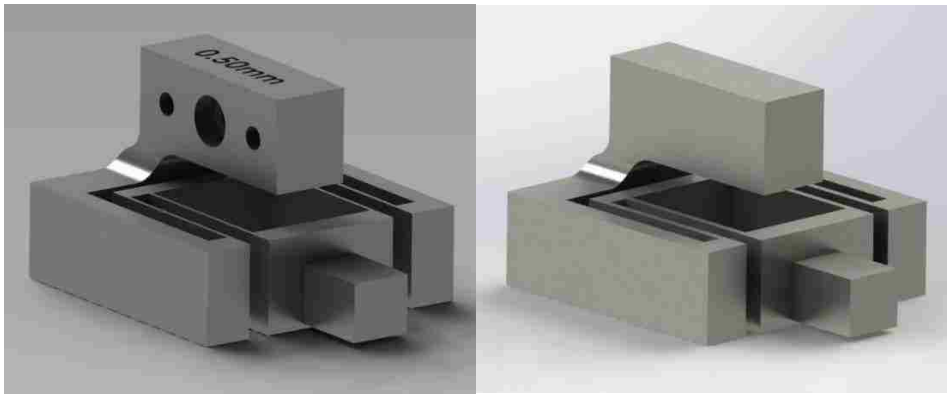

Figure 19 – CAD Geometries used for ANSYS Simulation

The constraints used during the simulations are shown in Figure 20. Initial simulations were performed using the complete CAD model including the mounting holes and the fixed constraints were applied to these mounting holes as shown at the top of Figure 20. Identical simulations were performed using the simplified model with the constraints applied to the two opposing faces where the mounting holes were removed, shown at the bottom of Figure 20. The two simulations produced virtually identical results, thus the subsequent ANSYS simulations were performed on the simplified model using these constraints to reduce number of mesh elements in this area of non-interest, and thus reducing computational time.

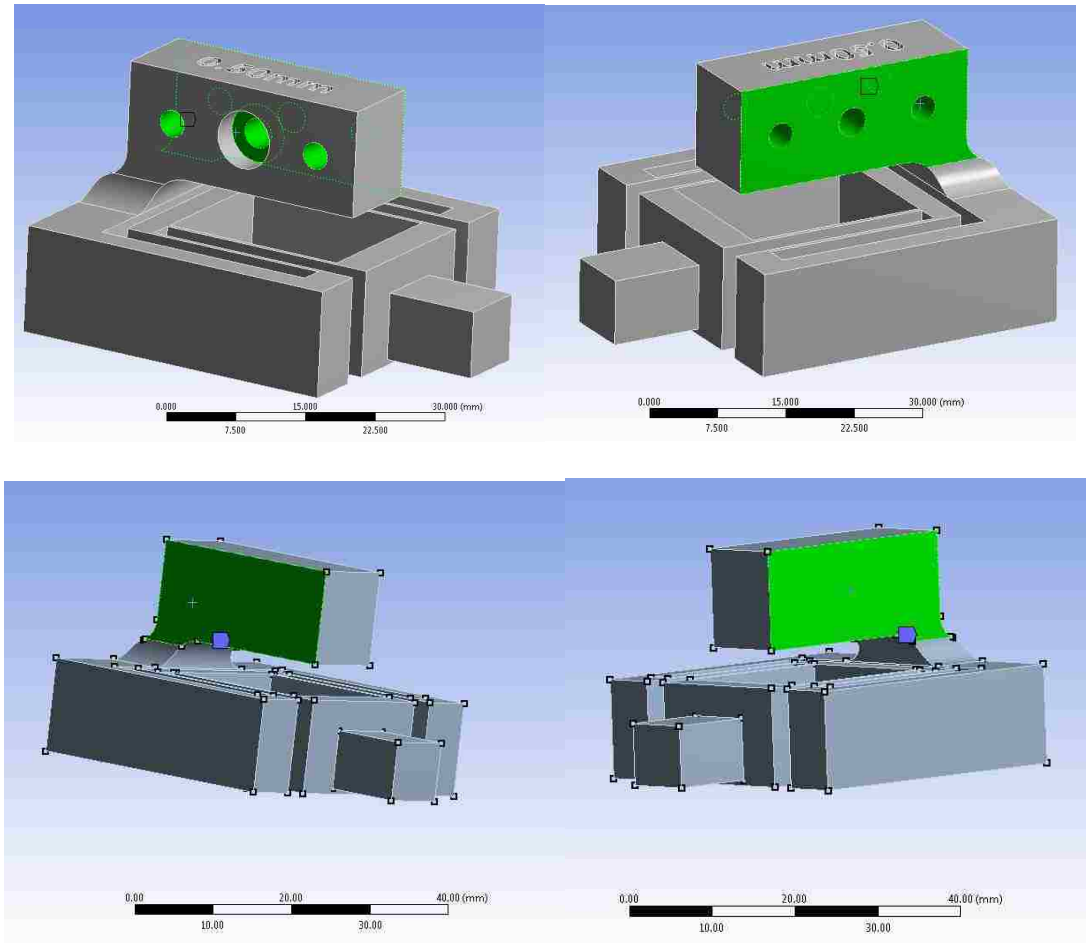

Figure 20 – ANSYS Simulation Constraints

In order to confirm simulation accuracy, a mesh convergence study was initially performed to determine the level of mesh refinement necessary to generate accurate results while balancing computational load of the simulations. Using the nominal parameters, several mesh refinements were run and the results compared to determine at what level the results converged. Figure 21 shows the results of the convergence study. The modal simulation generated the first six resonant frequencies of the coupon with the nominal parameters for differing mesh densities.

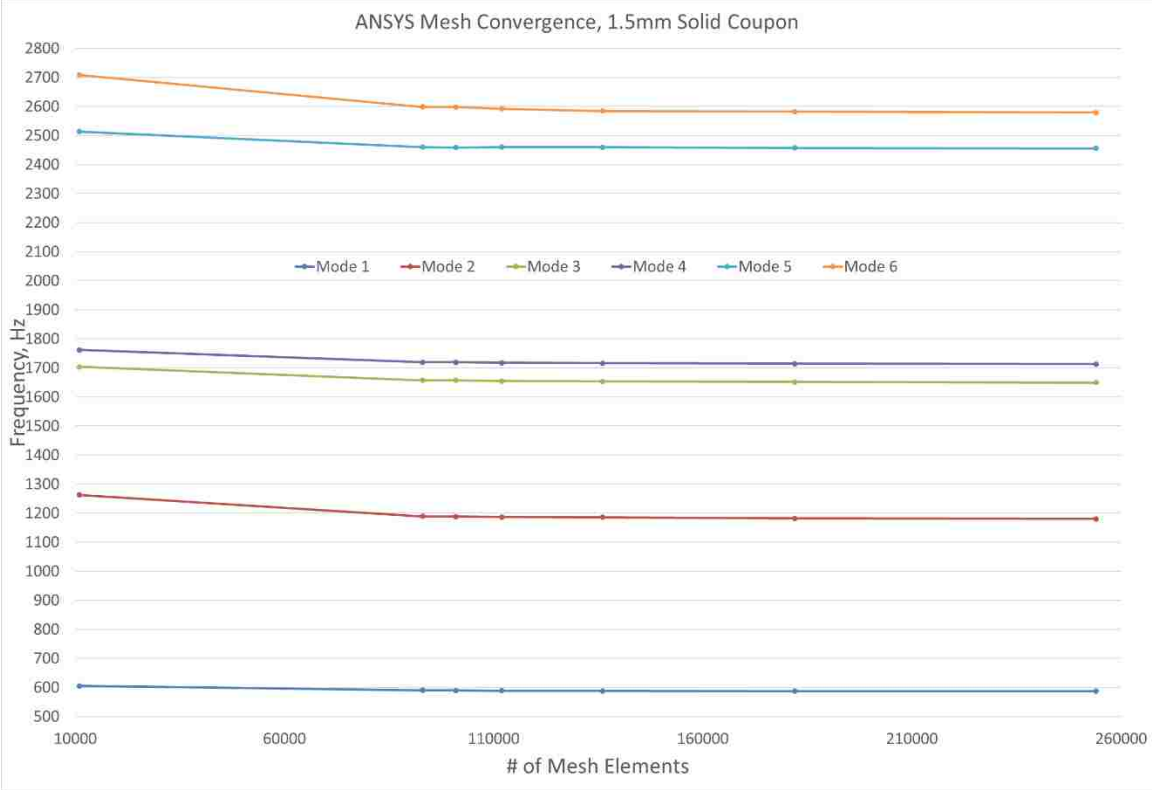

Figure 21 – Mesh Convergence Results

As can be seen by the convergence study plot, the results begin to converge as the number of mesh elements approach ~100,000 elements for the given geometry. As the number of elements increases beyond this threshold, the modal frequencies maintain, particularly for the 1st and 2nd modes that are of greater interest, thus indicating the mesh refinement has reached a level of diminishing returns, and the additional computational time required does not yield a more accurate result. The mesh parameters used at this threshold, and subsequently throughout the remainder of the simulations documented herein, are shown in Table 3.

Details of "Mesh"	
Physics Preference	Mechanical
Relevance	0
Sizing	
Use Advanced Size Function	On: Fixed
Relevance Center	Fine
Initial Size Seed	Active Assembly
Smoothing	Low
Transition	Fast
Min Size	Default (9.6937e-003 mm)
Max Face Size	Default (0.969370 mm)
Max Size	Default (1.93870 mm)
Growth Rate	Default (1.850)
Minimum Edge Length	0.429440 mm

Table 3 – Mesh Parameters

A representative image of the mesh is shown in Figure 22. The mesh was generated using the mesh parameters detailed in Table 3 and the simplified geometry shown in Figure 19, as were used for all ANSYS modal simulations detailed herein.

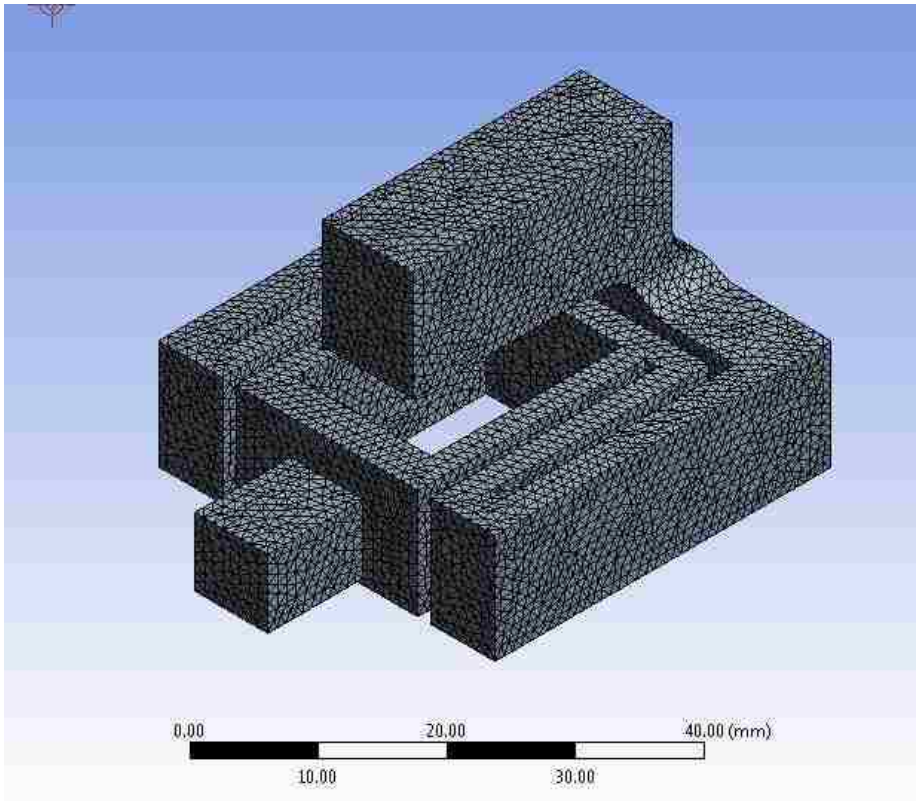

Figure 22 – ANSYS Mesh

5.3 Modal Parameter Sweeps

Initial simulations were performed by sweeping the model parameters detailed in Table 2. From this simulation data, 3-dimensional surfaces were generated by plotting pairs or parameters with the calculated resonant frequencies. Because three parameters were used and the difficulty in graphically representing a 4-dimensional plot, the parameters were grouped to produce the most useful graphical representations, while the additional parameter was fixed at the nominal value, unless otherwise noted. The first 8 vibrational modes were calculated in the simulation in order to observe any behavior that may have been of interest, although the higher mode shapes would be difficult to identify experimentally. Each modal frequency was plotted as a surface, with the modes being organized by increasing natural frequency. For example, the surface plot shown in Figure 23 displays the first 8 modal surfaces created by sweeping both the cantilever thickness and the bulk density of the coupon. This surface plot contains the first eight resonant modes, with the first mode having the lowest frequency (surface nearest the origin plane) and each subsequent mode increasing in frequency. Figure 24 contains a similar surface plot, but with the Young's modulus of the material being a swept parameter along with the cantilever thickness. These surface plots provided the operational space that the experiments were expected to stay within, and gave insight into the modal behavior as these parameters were varied across a significant range of values.

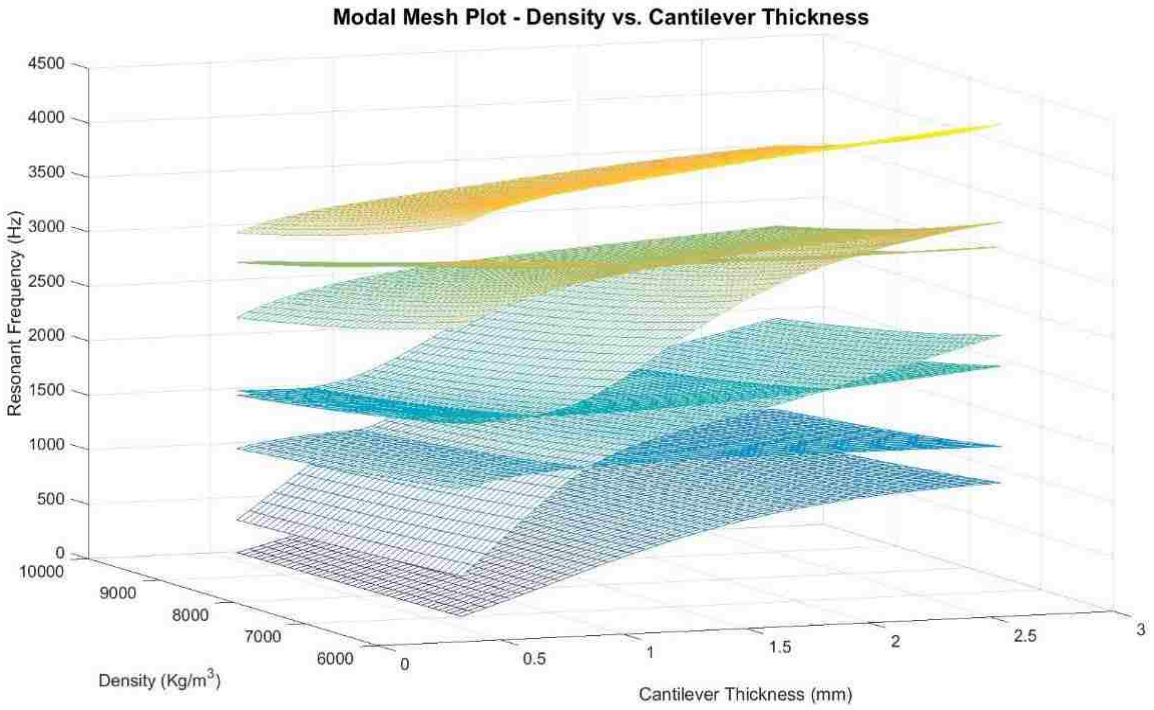

Figure 23 – Density vs. Cantilever Thickness Surface – Modal Surface Plot

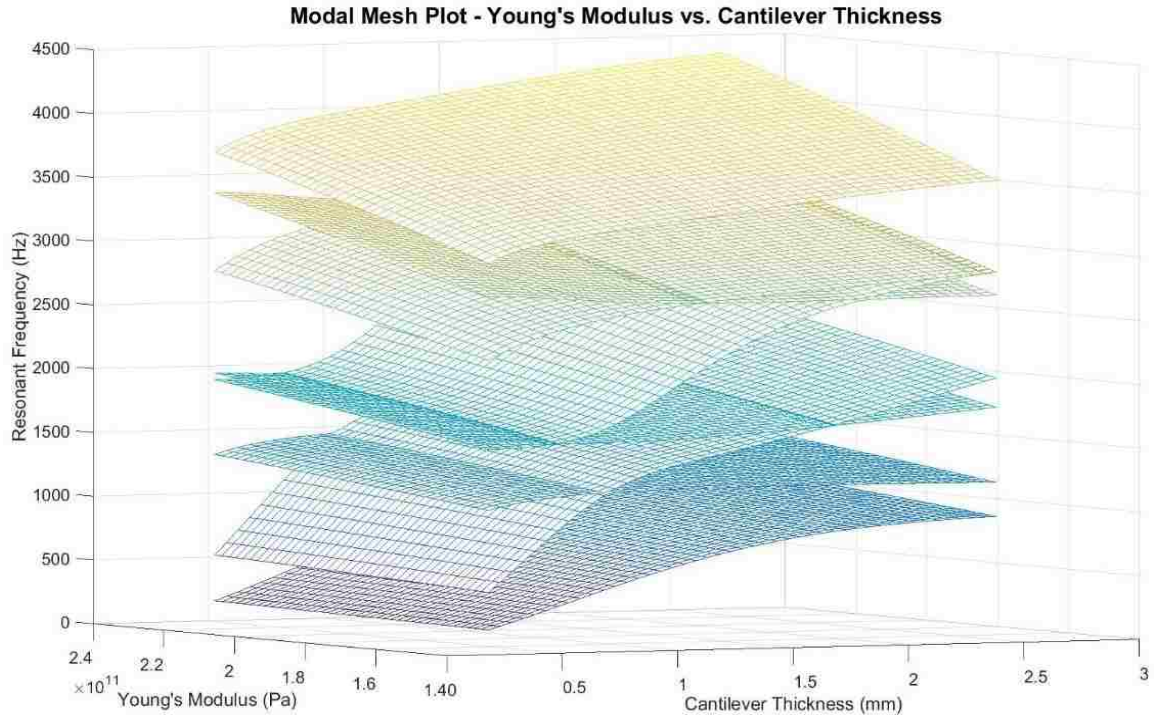

Figure 24 – Young's Modulus vs. Cantilever Thickness – Modal Surface Plot

While the first mode shape for all of the cantilever thicknesses evaluated in this study remained constant, the higher mode shapes changed frequency rank as the cantilever thickness increased. This can be seen in the two simulation sweeps for which either density or Young's modulus was wept against the cantilever thickness, shown in Figure 23 and Figure 24 respectively. Each individual surface represents a particular mode shape, and the intersections of the particular modal frequency surfaces represent the point where a particular mode shape's resonant frequency increased to the point of overtaking the previously higher mode. During simulation, the modes for a single cantilever thickness were identified by their particular resonant frequency rank, rather than any particular mode shape. Figure 25 shows the modal surface plot sweeping both density and Young's modulus for a single cantilever thickness of 0.50mm.

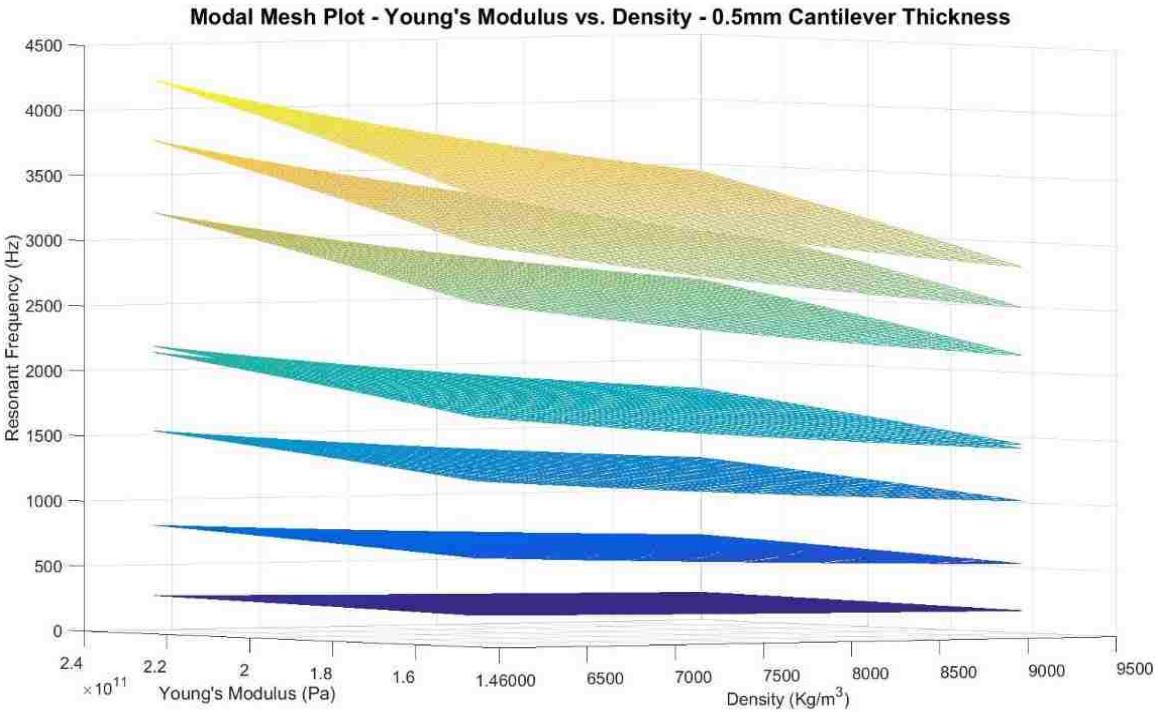

Figure 25 – Young's Modulus vs. Density – 0.5mm Cantilever – Modal Surface Plot

Specifically, the second mode shape for the 0.50mm cantilever thickness corresponds to the third mode shape for the 1.00mm and 1.50.mm cantilever thicknesses, and furthermore corresponds to the fourth mode shape for the 2.00mm and 2.50mm cantilever thicknesses. The first mode shape, which is consistent across each of the cantilever thicknesses used herein, is of primary interest for this study and can be seen in Figure 26. The second mode shape, (2^{nd} mode for the 0.5mm cantilevers, 3^{rd} mode for the 1.0mm & 1.5mm cantilevers and the fourth mode for the 2.0mm and 2.5mm cantilevers) is also of interest. Similar to the 1^{st} mode, it can be observed at the nose of the coupon, and is shown in Figure 27. For completeness, the subsequent mode shapes for the 0.50mm cantilever thickness are shown in Appendix A.3. The 1^{st} and 2^{nd} mode shapes will be the primary focus of this study.

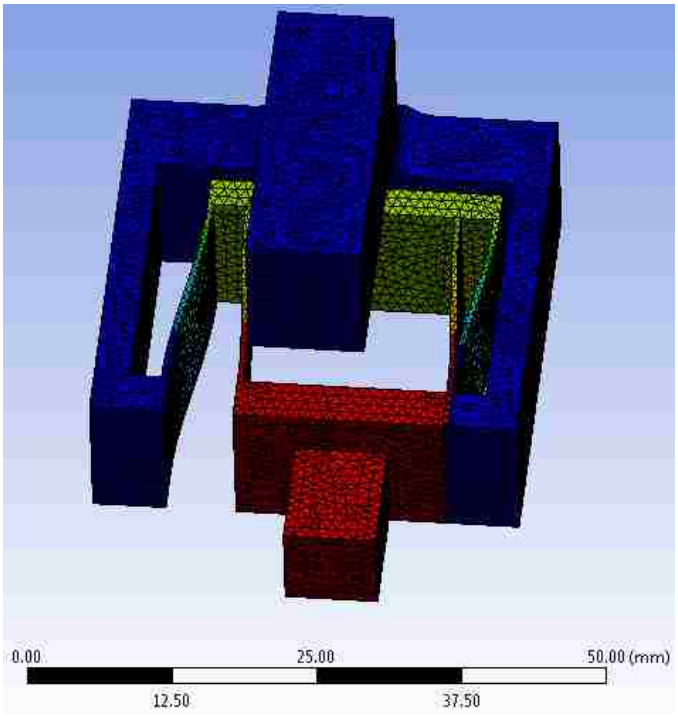

Figure 26 -1st Mode shape – 0.50mm Cantilever Thickness (4.2e-4 Scale)

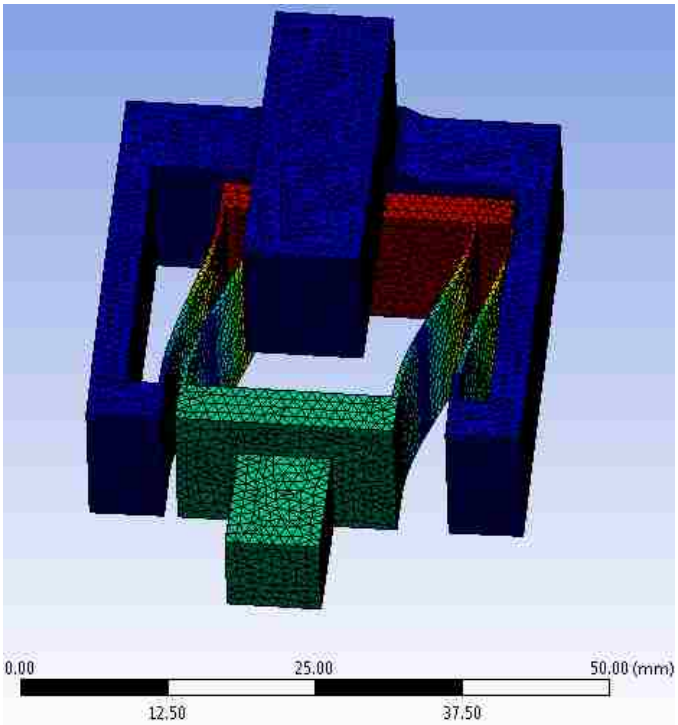

Figure 27 - 2nd Mode shape – 0.50mm Cantilever Thickness (3.4e-4 Scale)

As can be seen in the figures above, the first and second modes are of particular interest, as is to be expected given the geometric design of the coupons, because their motion occurs in the plane parallel to the bottom plane of the coupon. This allows for the use of the LDV to pick up these two modes with a single measurement point. It may also be possible to correlate material properties using the subsequent modes as well, but limitations in experimental setup and orientation of observation limit the collection of these higher modes from this experiment. The simulations were carried out to include the greater mode shapes in order to observe any advantageous modal behavior that may occur at these higher modes, with the potential to guide future work in this area of non-destructive material property characterization.

CHAPTER 6: Results

This chapter documents the data collected during experimentation, the simulation data, and the comparison between the two. As described previously, the first and second mode shapes shown in Figure 26 & Figure 27 were the focus of this study due to the constraints of the experimental setup and the ability to identify these lower frequency modes. The simulations were performed prior to physical experimentation, thus the parameter ranges were not ideal, based on the modal frequencies observed. Also, as stated above, the dimensions of the cantilevers were assumed as nominal based on digital image inspection of a small number of parts and the tolerance expectations of the DMLS process.

6.1 Resonant Frequencies

Using the velocity data collected for each coupon and the fft algorithm in MATLAB, the frequency domain response was calculated. From each of these frequency domain plots, the peaks, which correspond to a resonant frequency were identified. In general, each subsequent run for each coupon produced identical resonant frequencies, and those were identified by extracting the location of each peak. Figure 28 shows the frequency domain plot for the 0.5mm flat cantilever #1 for reference while the remaining frequency domain plots can be seen in Appendix A.4. As the cantilever thickness increased and thus the force required to displace the cantilevers increased, the noise observed in the lower frequency regions increased, as can be seen in Figure 29, showing the frequency domain for the 2.0mm angled coupon #1. A best effort was made to identify the local peaks corresponding to the resonant frequencies from these plots with increased noise. It is hypothesized that the noisy response for the thicker cantilevers was due to the vibration induced in the fixture, but additional work would be needed to identify the frequency response of the fixture.

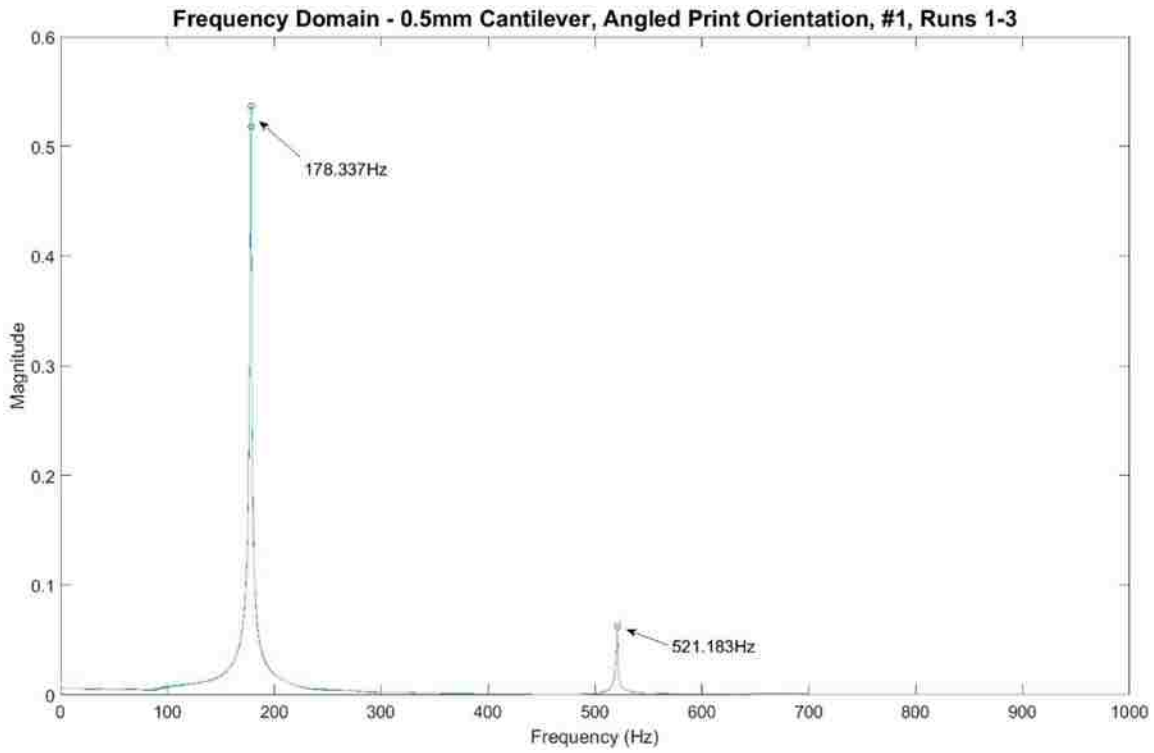

Figure 28 – Frequency Domain with Resonant Frequencies – 0.5mm Flat #1, Runs 1-3

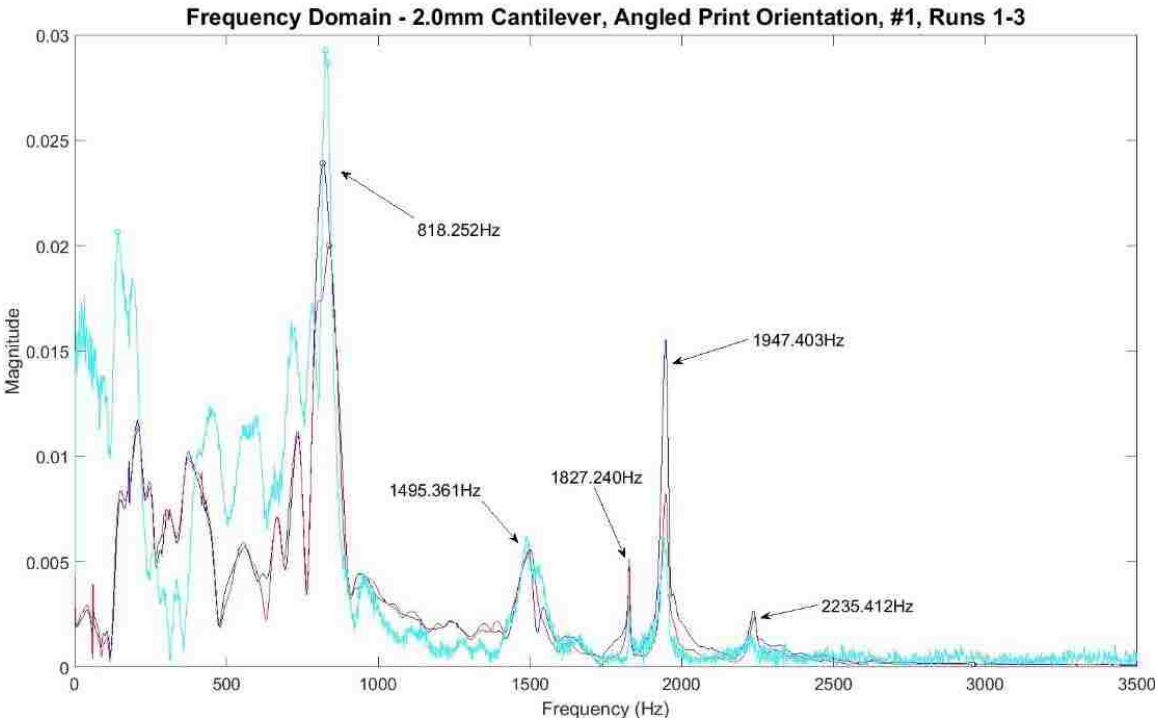

Figure 29 – Frequency Domain with Resonant Frequencies – 2.0mm Angled #1, Runs 1-3

The resonant frequencies were identified for each coupon, and the values plotted for each set of coupons to display the range of resonant frequencies identified for both the first and second modes. Figure 30 shows the identified first mode resonant frequencies for each coupon set while Figure 31 plots the second mode resonant frequencies.

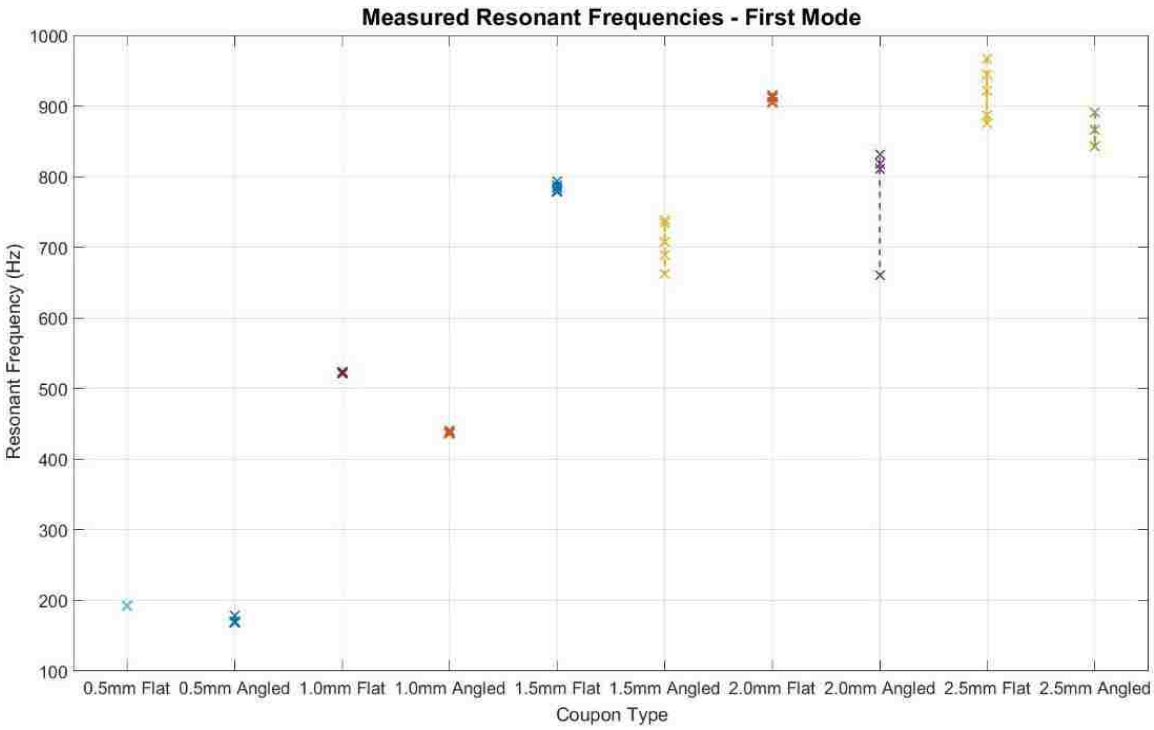

Figure 30 – First Mode Resonant Frequencies for each Coupon Type

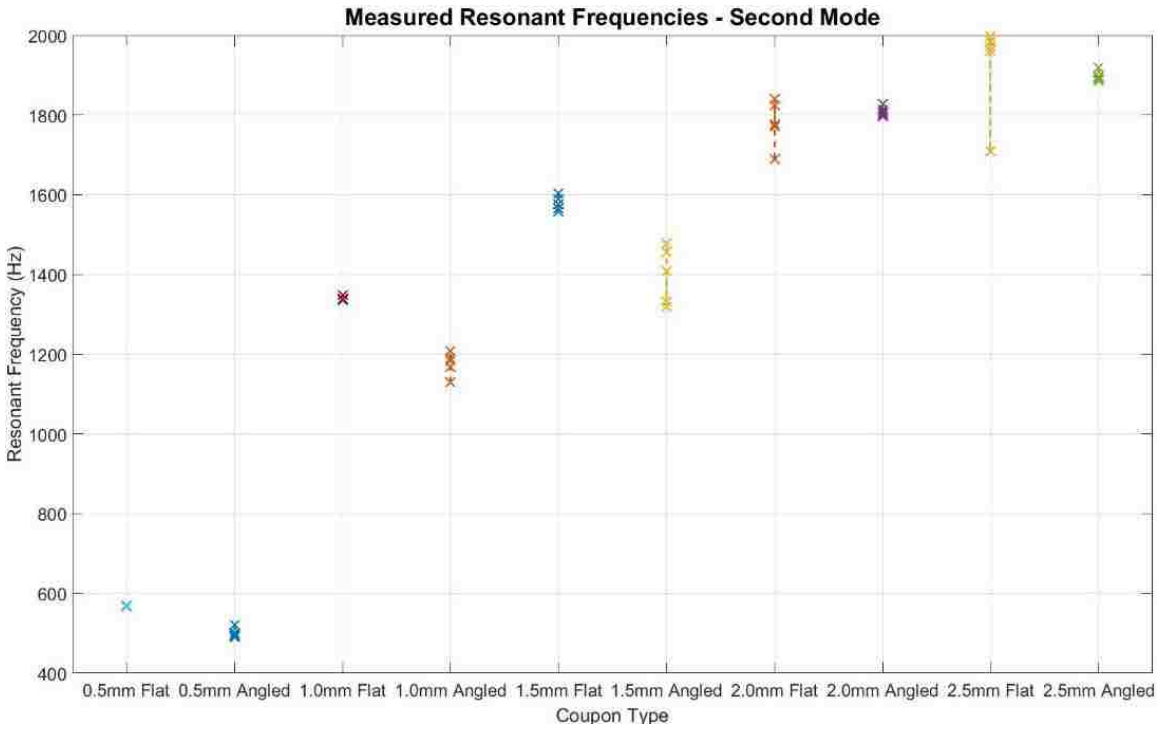

Figure 31 – Second Mode Resonant Frequencies for each Coupon Type

From these plots, it can be seen that as the cantilever thickness increases, the uncertainty in the resonant frequencies increases, as explained above. Also, it can be noted that the angled print orientation also produced a greater variance in resonant frequencies for nearly each cantilever thickness. The uncertainty is relatively consistent between the first and second modes, suggesting that there is coupon-to-coupon variance, rather than error in identifying the modal frequencies. Most resonant frequencies were easy to identify, as can be seen in the frequency domain plots in Appendix A.4, save a handful of noisy low-frequency regions, which suggests these frequencies are accurate for each given coupon.

6.2 Mass & Density

The coupons were weighed and the volume measured such that the density could be calculated. The Archimedes method used to measure part volume is described in a previous chapter. A portion of the mass and density measurements and calculations can be seen in

Table 4, while the complete dataset can be found in Appendix A.1. The table with the density of DI water versus temperature can also be found in Appendix A.2.

Coupon	Dry Mass (g)	"Wet" Mass (g)	Buoyant Force (g)	Water Temp (°C)	Density of Water (g/cm^3)	Vol. of Coupon (cm^3)	Density of Coupon (kg/m^3)
Angled 0.5mm #1	91.517	79.959	11.558	21.7	0.997837	11.58305415	7900.938634
Angled 0.5mm #2	91.485	79.939	11.546	21.7	0.997837	11.57102813	7906.384717
Angled 0.5mm #3	91.515	79.97	11.545	21.7	0.997837	11.57002597	7909.662456
Angled 0.5mm #4	91.677	80.126	11.551	21.7	0.997837	11.57603897	7919.54832
Angled 0.5mm #5	91.535	79.987	11.548	21.8	0.997815	11.57328763	7909.161415

Table 4 – Archimedes Density Measurements

Table 5 contains some of the relevant statistics from mass and density measurements.

Flat Orientation	Nominal CAD Volume (cm^3)	Average Measured Volume (cm^3)	Volume Delta (cm^3)	Average Density (kg/m^3)
0.5mm	12.13	12.00865509	0.121344905	7902.085795
1.0mm	12.69	12.52886373	0.161136269	7922.299523
1.5mm	13.25	13.11661796	0.13338204	7907.947425
2.0mm	13.81	13.69943139	0.110568611	7902.83673
2.5mm	14.37	14.15109401	0.21890599	7906.072937
	Average Volume Delta		0.147236443	
Angled Orientation				
0.5mm	12.13	11.57468697	0.55531303	7909.139109
1.0mm	12.69	12.05572488	0.634275123	7909.019599
1.5mm	13.25	12.63397664	0.616023356	7908.155475
2.0mm	13.81	13.18236483	0.627635173	7911.396514
2.5mm	14.37	13.74349289	0.626507115	7900.63141
	Average Volume Delta		0.611950759	
		Total Population		7908.12008
		Nearest Sim Density Parameter		7948.7179

Table 5 – Coupon Density Data

With the density across the entire population of coupons being grouped very tightly, the average value was taken and the simulation data was taken from the nearest data point from the density parameter sweep. The parameter values, shown in Appendix A.7 show the nearest density parameter points of 7869.23 kg/m^3 and 7948.71kg/m^3.

6.3 Young's Modulus Determination

The Young's modulus values from simulation data for the density parameter points above was extracted for each cantilever thickness and used for the subsequent data comparisons between experimental result and simulated resonance. The range of the Young's modulus parameter set used for the simulations, in some cases, did not extend out to the intersection point for some cantilever types, so the simulated data was linearly extrapolated. In the plots below, the ANSYS simulated data for each given density is represented by the solid line (towards the upper extrema) while the data points that were extrapolated from this data are represented by the dashed portions of the lines for each given density. Interpolation between these two density curves provides the approximate measured density of the parts used during experimentation, based on the measured density.

Figure 32 and Figure 33 represent the 0.5mm cantilever thickness, both the flat and angled print orientations, using the first and second modes, respectively. The sloped lines represent the simulation (and extrapolated) data for the two nearest density points used during the simulation. The parallel horizontal lines represent the resonant frequencies identified for each coupon type from experimental data. The point at which these lines intersect theoretically coincides with the Young's modulus for that particular coupon. The remaining correlation plots can be seen in Appendix A.5.

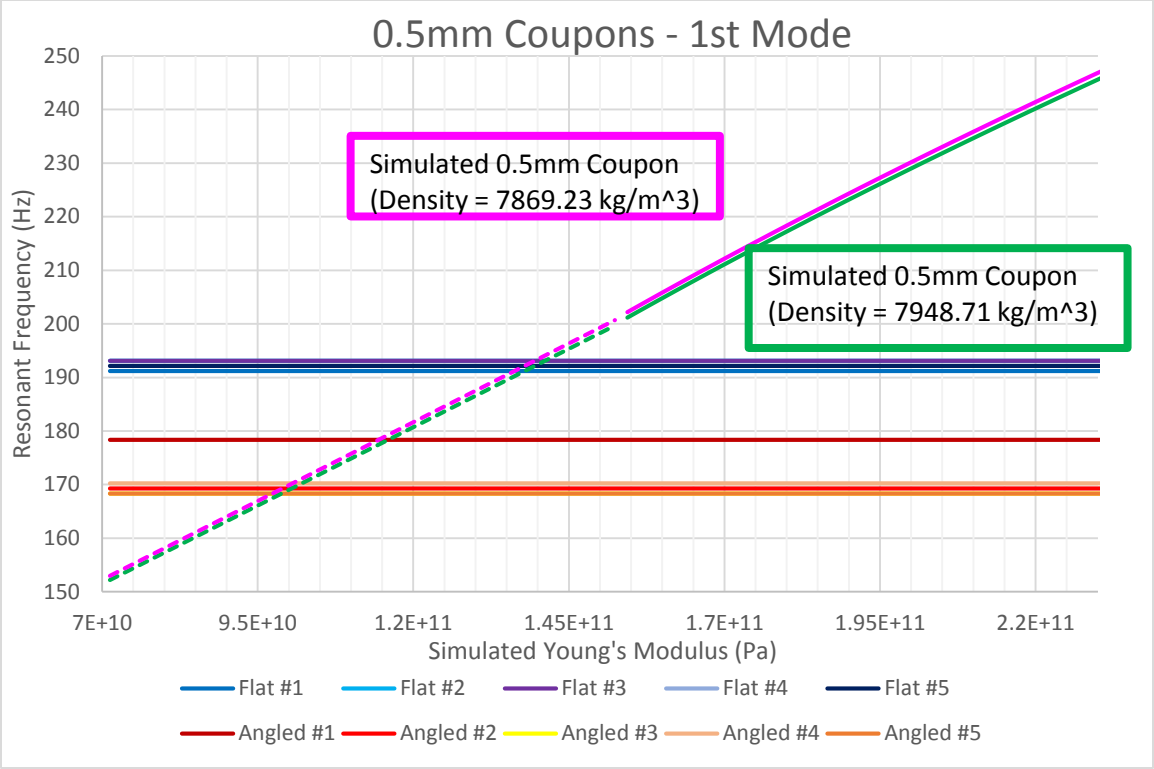

Figure 32 – Correlation between Simulation & Experimental Data – 0.5mm, First Mode

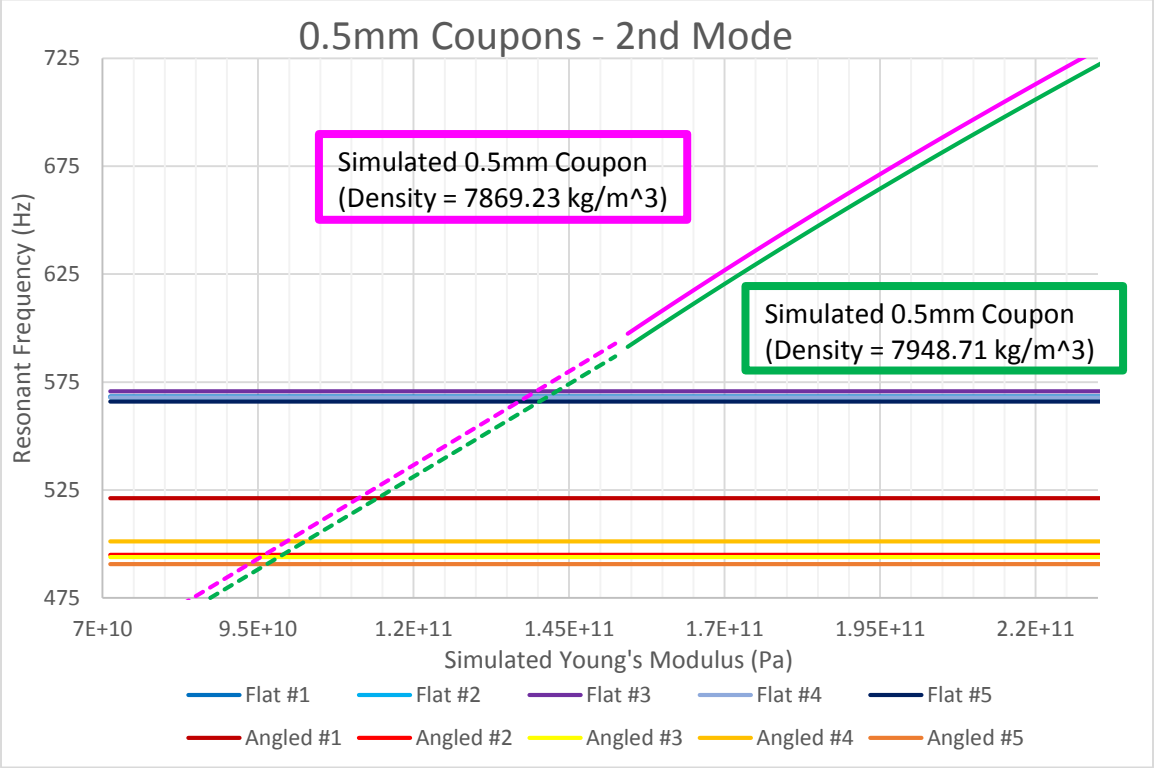

Figure 33 – Correlation between Simulation & Experimental Data – 0.5mm, Second Mode

By identifying the points at which the experimental resonant frequencies intersect with the simulation data, the theoretical Young's modulus is subsequently identified. The individual values can be found in Appendix A.6. Figure 34 plots this theoretical Young's modulus for each coupon type based on the simulated density of 7869.23 kg/m^3, showing the range of values based on each particular coupon, and for both the first and second modes individually. Figure 35 plots the similar values determined from the density value of 7948.71 kg/m^3.

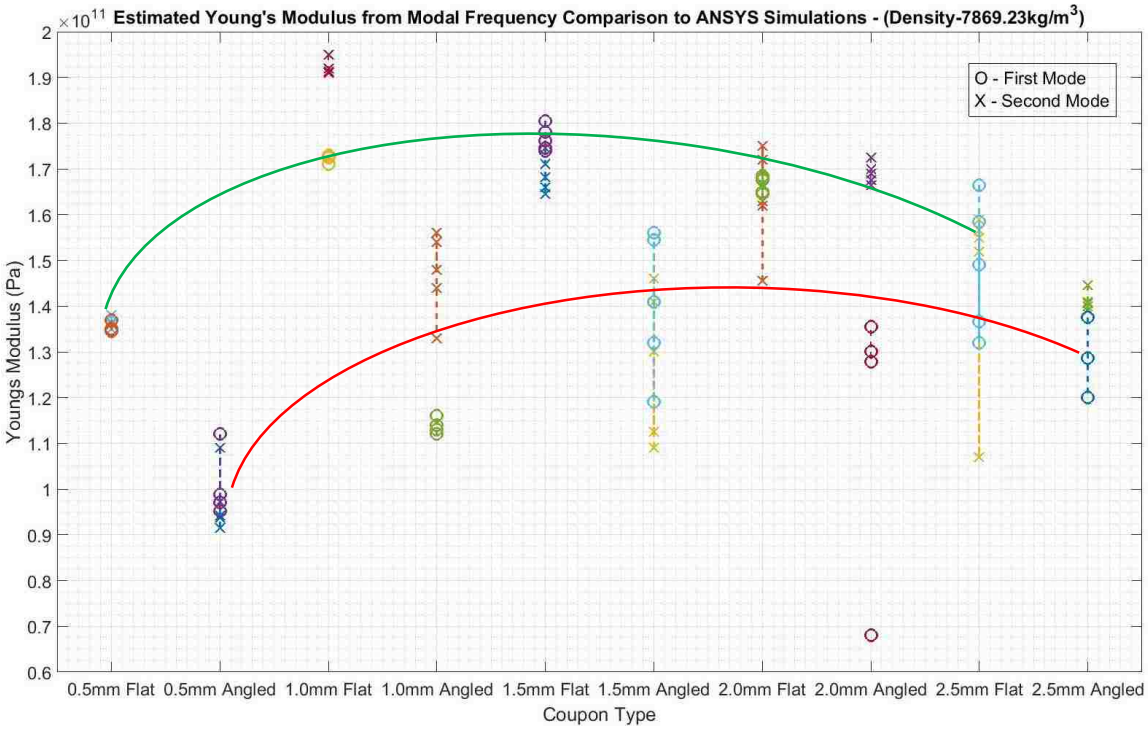

Figure 34 – Theoretical Young's Modulus for each Coupon Type, First & Second Modes (Density=7869.23 kg/m^3) Approximate Trend Lines - Green-Flat, Red-Angled

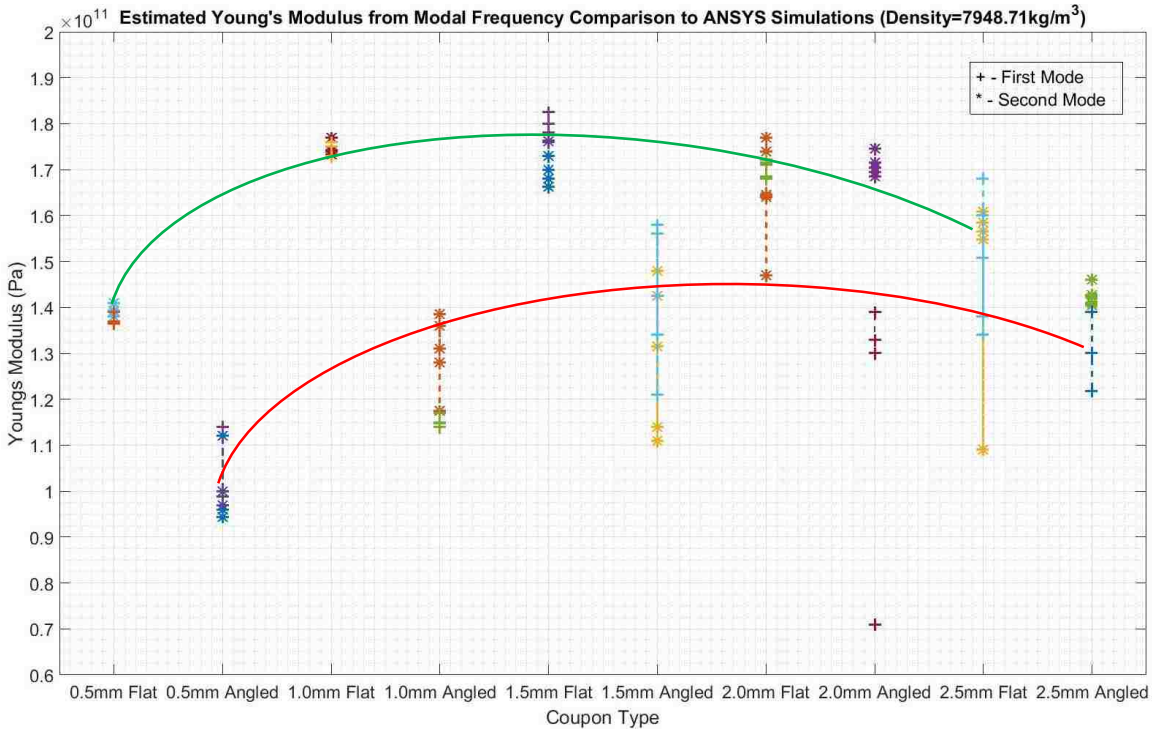

Figure 35 - Theoretical Young's Modulus for each Coupon Type, First & Second Modes (Density=7948.71 kg/m^3) Approximate Trend Lines - Green-Flat, Red-Angled

Note the differences in Young's modulus for the 1.0mm flat and 1.0mm angled between the two densities. This stark difference is due to the intersection between the experimental resonant frequency and the simulation parameter sweep occurring at the point where extrapolation begins, which can be seen in the plots in Appendix A.5. This is likely an artifact of the linear extrapolation, and thus the difference should not be considered significant in the scope of this study. All other coupon types show the expected shift due between the two density values used in simulation.

CHAPTER 7: Research Summary & Conclusions

Observing the predicted Young's modulus in Figure 34 and Figure 35, the variation across the suite of coupons is evident. The nominal Young's modulus for wrought 316L generally ranges from 1.9e11 Pa - 2.1e11 Pa (nominal used for simulations 1.93e11 Pa). The predicted Young's modulus for each coupon set is well below the nominal value, as is generally expected for AM materials. The future of AM parts is not wholly dependent on reaching material property levels equivalent to their wrought counterparts, but rather confidence and predictability of their true material properties. The results from this study show that the use of modal frequency analysis can be used as a tool to quantify the functional material properties of actual parts produced using AM. Most importantly, the testing of these parts was wholly non-destructive, allowing further use, whether for more robust datasets, or for direct comparison after post-processing.

Non-destructive evaluation of AM parts will be key to the early adoption into high-consequence applications, facilitating 100% acceptance testing. Refinement of this modal frequency technique would potentially provide a means of quantifying the properties of as-printed parts. This research shows the viability of the application of this technique for the purpose of qualifying AM produced hardware.

7.1 Results Summary

Comparison of the experimental data to the simulated data produced a result in line with what was expected for this initial research. The Young's modulus values predicted with the simulation parameter sweeps and extrapolations align with initial engineering judgement towards the performance of AM parts. While significantly lower than nominal wrought values, the agreement between multiple coupons of the same pedigree also points

to the validity of the experiment. The variation across both print orientation and coupon thickness is to be expected, but again the ability to identify these differences with the modal frequency technique has been demonstrated.

The experimental setup provided an acceptable platform for many of the tests. The collection of data for the coupons was adequate for the frequencies that were expected, and the LDV was an ideal method for observation, given the non-contact interface, the adjustability and ease of use. The fixturing of the coupons worked well, though the introduction of noise within some of the stiffer coupons may suggest that improvements may need to be made to characterize the thicker cantilevers with greater confidence.

There is also a distinct shift in the predicted Young's modulus between the two print orientations. As anisotropies are a known artifact of AM processes, this may not be surprising, but the ability to detect this delta through modal frequency analysis is important to the development of AM qualification. The increasing standard deviation with cantilever thickness that can be seen is likely due to the increased noise from the fixturing that was observed as the cantilever thickness increased.

7.2 MFT Conclusions

As was noted previously, the use of modal frequencies to determine Young's modulus is not an entirely new concept, and has been applied in quality control, acceptance and materials testing. The application to AM parts is, however, relatively unexplored. The initial results of this study show that the sensitivity of the modal frequencies to changes in material properties introduced by the AM processes can prove valuable in the quest to better understanding AM parts and qualification of AM parts for high-consequence end users.

The use of laser Doppler vibrometry was key to the success of the experiments, as the non-contact measurement of the vibrational response allowed for the large displacement excitation to be accurate and sampled at a rate well above the expected natural frequencies. The use of this technology in future qualification of as-printed parts will be key, as vibration of multiple features can be easily observed without the need for additional fixtures or experimental setups.

The suite of coupons used provided a wide range of scenarios to test in order to vet the MFT process with respect to AM. Comparison between the print orientations provided a direct means to observe the anisotropies along the build planes. The MFT coupled with the FEA simulations was able to detect these differences across the entire range of cantilever thicknesses tested. While these coupons were designed specifically with this testing in mind, the results are not unique to this geometry. Coupled with accurate simulation results, the material properties of unique geometries could similarly be determined.

Using the MFT in addition to process control efforts with respect to AM can accelerate the qualification of AM parts and expand the tools available for testing. Many observations were made about the suite of coupons within this research that were exposed by the use of MFT.

7.3 AM Print Conclusions

The experimental results show that while the values for Young's modulus that were determined by comparison to the simulated results deviate from the wrought values and show variation between coupon types, there is close grouping for each coupon type. This grouping of each type suggest that there are distinct differences in the functional material properties between these groups, rather than gross inaccuracies introduced by the testing

methodology. These variations are precisely what need to be better understood in order to advance the acceptance of AM parts.

The first primary delta that can be observed in the data is the consistently lower young's modulus values of the angled print orientation when compared to the flat print orientation coupons of equal thickness. This orientation dependence is likely due to the positioning of the continuous "strands" or lengths of powder that are sintered continuously. While other research and process development suggests that there is adequate re-melting between slices, a fibrous behavior may still be present. This may induce a fiber-matrix composite-like behavior and contribute to the anisotropy introduced by the print orientation. Particularly for the case of the cantilever coupons, the displacement observed for the flat oriented coupons occurs in-plane with the continuous path of the sintering. This would potentially render the interactions between the sintered layers less significant when compared to the angled print orientation. For the angled configuration, the individual layers traverse the cantilever beams at a 45-degree angle, thus the interactions between each sintered layer would be significant with respect to the first and second mode displacement of the coupons. Similar to composite behavior, the strength of a material is greater when stressed parallel to the reinforcing fibers. When loaded at 45 degrees to the fiber orientation, the shear between the fibers and matrix dominate the strength performance, thus the observed properties would be weaker in that loading direction relative to the loading along the fibers. Perhaps this is a similar phenomenon being observed in the print orientation dependency.

Another significant observation in the Young's moduli determined for each coupon type is the trend as the cantilever thickness increases. As the thickness increases from 0.5mm it

appears that the observed modulus also increases. This trend seems to hold for both print orientations. The modulus increases up until the 1.5mm cantilever thickness, and as the thickness increases beyond that, the modulus begins to fall towards the modulus observed in the 0.5mm cantilevers. One hypothesis explaining this change in observed modulus is that the "wall" material has differing properties from that of the "body" of the printed material, and the ratio between them has a quantitative effect on the functional material properties of the AM part. As the material is sintered, the cooling process is influenced by the presence of surrounding material (or lack of). The "wall" material, or material that makes up the outer surfaces of the part, are directly exposed to un-sintered powder on one surface while it solidifies, while the "body" material, or the interior of the part, is potentially re-melted as the adjacent material is sintered as the laser follows the rastered toolpath. There are likely several unknown factors contributing to this delta in Young's modulus with increasing cantilever thickness in addition to this presented hypothesis.

The approximate trend lines demonstrate the delta between the two orientations, and the appearance of a convergence as the cantilever thickness increases can be noted. This would suggest that the print orientation differences may be less significant as feature size increases. While the trend appears in both the flat and the angled print orientation, the deviation in measured frequencies and thus the determined Young's moduli increases with cantilever thickness. Due to this increase in uncertainty, drawing conclusions from this observation is likely speculation. Whether this is a product of the "wall" versus "body" material thoughts described above, or due to some alternate phenomenon, this is an area that would need additional testing in order to improve understanding.

7.3 Suggestions for Future Work

The results of the research conducted within the scope of this thesis explored the application of MFT to the qualification and understanding of AM material properties. The initial conclusions show the viability of the application of this technology to the field, but many areas could be explored in order to increase the accuracy of the determinations and the effectiveness of the MFT.

Within this experiment, the primary source of error appears to be the introduction of noise into the time domain signals either from inadequate fixturing or from other sources. The use of more rigid fixtures would likely improve the ability to accurately determine the resonant frequencies, particularly when testing stiff samples that require higher force excitations. Considerations should be made to fixture vibrations for future MFT application.

The MFT relies heavily on the accuracy of the FEA results. Higher resolution modal simulations and parameter sweeps would allow for a more accurate Young's modulus determination. Also, incorporating potential anisotropies into the FEA model could help predict the anisotropies observed through experimentation.

The dimensions of the cantilever coupons were taken as nominal after preliminary measurements taken with digital image correlation. While this assumption likely did not affect the conclusions made in this thesis, this is a particular area that could increase the accuracy of the correlations to the simulated resonant frequencies. The cantilever thickness, in particular, would greatly influence the natural frequencies. In addition to the spatial dimensions, the measurement of the material density should be considered. The coupons were assumed homogeneous, which is potentially not the case.

REFERENCES

1. Conner, Brett P., *Making sense of 3-D printing: Creating a map of additive manufacturing products and services*, Additive Manufacturing, 2014. 1-4: p. 64-76.

2. Mellor, Stephen, *Additive manufacturing: A framework for implementation*, International Journal of Production Economics, 2014. 149: p. 194-201.

3. Guo, Nannan, *Additive manufacturing: technology, applications and research needs*, Front. Mech. Eng., 2013. 8(3): p. 215-243.

4. Huang, Yong, *Additive Manufacturing: Current State, Future Potential, Gaps and Needs, and Recommendations*, Journal of Manufacturing Science and Engineering, 2015. Vol. 137.

5. Yang, Sheng, *Additive manufacturing-enabled design theory and methodology: a critical review*, International Journal for Advanced Manufacturing Technology, 2015. 80: p.327-342.

6. Achillas, Ch., *A methodological framework for the inclusion of modern additive manufacturing into the production portfolio of a focused factory, Journal of Manufacturing Systems*, 2015. 37: p. 328-339.

7. Frazier, William E., *Metal Additive Manufacturing: A Review*, JMEPEG, 2014. 23: p. 1917-1928.

8. Seifi, Mohsen, *Overview of Materials Qualification Needs for Metal Additive Manufacturing*, The Minerals, Metals & Materials Society, 2016.

9. Gao, Wei, *The status, challenges, and future of additive manufacturing in engineering*, Computer-Aided Design, 2015. 69: p. 65-89.

10. Monzon, M.D., *Standardization in additive manufacturing: activities carried out by international organizations and projects*, International Journal of Advanced Manufacturing Technology, 2015. 76: p. 1111-1121.

11. Martukanitz, Richard, *Toward an integrated computational system for describing the additive manufacturing process for metallic materials*, Additive Manufacturing, 2014. 1-4: p 52-63.

12. King, W.E., *Laser powder bed fusion additive manufacturing of metals: physics, computational, and materials challenges*, Applied Physics Reviews, 2015. 2: 041304

13. Guan, Kai, *Effects of processing parameters on tensile properties of selective laser melted 304 stainless steel*, Materials and Design, 2013. 50: p. 581-586.

14. Meier, H., *Experimental studies on selective laser melting of metallic parts*, Mat.-wiss. u. Werkstofftech, 2008. 39, No. 9: p. 665-670

15. Thompson, Scott M., *An overview of Direct Laser Deposition for additive manufacturing; Part I: Transport phenomena, modeling and diagnostics*, Additive Manufacturing, 2015. 8: p. 36-62

16. Shamsaei, Nima, *An overview of Direct Laser Deposition for additive manufacturing; Part II: Mechanical behavior, process parameter optimization and control*, Additive Manufacturing, 2015. 8: p. 12-35

17. Nelaturi, Saigopal, *Representation and analysis of additively manufactured parts*, Computer-Aided Design, 2015. 67-68: p. 13-23

18. Zheng, B., *Thermal Behavior and Microstructure Evolution during Laser Deposition with Laser-Engineered Net Shaping: Part II. Experimental Investigation and Discussion*, Metallurgical and Materials Transactions A, 2008. 39A: p. 2237-2245

19. Hu, Dongming, *Sensing, modeling and control for laser-based additive manufacturing*, International J. of Machine Tools & Manufacture, 2003. 43: p. 51-60

20. Slotwinksi, John, *Applicability of Existing Materials Testing Standards for Additive Manufacturing Materials*, National Institute of Standards and Technology Internal Report, 2014. 8005.

21. Waller, Jess M., *Nondestructive Evaluation of Additive Manufacturing State-of-the-Discipline Report*, NASA/TM, 2014. 218560

22. Galarraga, Haize, *Effects of the microstructureand porosity on properties of Ti-6Al-4V ELI alloy fabricated by electron beam melting (EBM),* Additive Manufacturing, 2016. 10: p. 47-57.

23. Mani, Mahesh, *Measurement Science Needs for Real-time Control of Additive Manufacturing Powder Bed Fusion Processes*, NIST Internal Report, 2015. 8036.

24. Slotwinski, J.A., *Characterization of Metal Powders Used for Additive Manufacturing*, Journal of Research of the National Institute of Standards and Technology, 2014. 119: p. 406-493

25. Slotwinski, John, *Mechanical Properties Testing for Metal Parts Made via Additive Manufacturing: A Review of the State of the Art of Mechanical Property Testing*, National Institute of Standards and Technology Internal Report, 2012. 7847.

26. Migliori, A., *Resonant ultrasound spectroscopic techniques for measurement of the elastic moduli of solids*, Physica B, 1993. 183: p. 1-24

27. Mogliori, Albert, *Resonant ultrasound spectroscopy for materials studies and non-destructive testing*, Ultrasonics, 1996. 34: p. 473-476

28. Leisure, R. G., *Resonant ultrasound spectroscopy*, Journal of Physics: Condensed Matter, 1997. 9: 6001-6029.

29. Tariq, Fawad, *Characterization of Material Properties of 2xxx Series Al-Alloys by Non Destructive Testing Techniques*, Journal of NDE, 2012. 31: p. 17-33.

30. Nahvi, H., *Crack detection in beams using experimental modal data and finite element model*, International Journal of Mechanical Sciences, 2005. 47: p. 1477-1497

31. Kim, Jeong-Tae, *Damage identification in beam-type structures: frequency-based method vs mode-shape-based method*, Engineering Structures, 2003. 25: p 57-67

32. Bejger, A., *Identification of structural defects of metal composite castings with the use of elastic waves*, Archives of Metallurgy and Materials, 2011. 56: p. 129-133

33. Prucha, Thomas E., *New Approach in Non-Destructive Evaluation Techniques for Automotive Castings*, SAE Technical Paper Series, 2003-01-0436.

34. Uhlmann, Eckhart, *Additive manufacturing of titanium alloy for aircraft components*, Procedia CIRP, 2015. 35: p. 55-60

35. Mukherjee, T., *Printability of alloys for additive manufacturing*, Scientific Reports, 2016. 6: 19717.

36. Baufeld, Bernd, *Mechanical Properties of INCONEL 718 Parts Manufactured by Shaped Metal Deposition (SMD)*, JMEPEG, 2012. 21: p. 1416-1421

37. Tolosa, Itziar, *Study of mechanical properties of AISI 316 stainless steel processed by "selective laser melting", following different manufacturing strategies*, International Journal of Manufacturing Technology, 2010. 51: p. 639-647

38. Luecke, William E., *Mechanical Properties of Austenitic Stainless Steel Made by Additive Manufacturing*, Journal of Research of the National Institute of Standards and Technology, 2014. 119: p. 398-418

39. Mertens, A., *Microstructures and Mechanical Properties of Stainless Steel AISI 316L Processed by Selective Laser Melting,* Materials Science Forum, 2014. 783-786: p. 898-903.

40. Everhart, Wes, *The effect of surface finish on tensile behavior of additively manufactured tensile bars*, Journal of Material Science, 2016. 51: p. 3836-3845

41. Wang, James C., *Young's modulus of porous materials*, Journal of Materials Science, 1984. 19: p. 801-808

42. Buchaillot, Lionel, *Silicon Nitride This Films Young's Modulus Determination by an Optical Non Destructive Method*, Japan J. of Applied Physics, 1997. 36: p. 794-797

43. Roebben, G., *Impulse excitation apparatus to measure resonant frequencies, elastic moduli, and internal friction at room and high temperature*, Review of Scientific Instruments, 1997. 68: p. 4511-4515

44. Burdzik, R., *Method of assessing the impact of material properties on the propagation of vibrations excited with a single force impulse*, Archives of Metallurgy and Materials, 2012. 57: p. 409-416

45. Schwarz, Jim, *Process Compensated Resonant Testing in Manufacturing Process Control*, Materials Evaluation, 2005.

46. Zeng, Du-Juan, *Resonant frequency-based method for measuring the Young's moduli of nanowires*, Physical Review, 2007. B76: 075417

47. Digilov, Rafael M., *Flexural Vibration Test of a Beam Elastically Restrained at one End: A New Approach for Young's Modulus Determination,* Advances in Materials Science and Engineering, 2013. Article ID 329530.

APPENDIX

A.1 Mass, volume and density data

Density Measurements							
Cantilever	Dry Mass (g)	Wet Mass (g)	Delta (g)	Temp (°C)	DI Density (g/cm^3)	Part Density (kg/m^3)	Part Volume (cm^3)
Flat 0.5mm #2	95.268	83.185	12.083	21.6	0.99786	7867.593022	12.10891307
Flat 0.5mm #3	95.004	83.022	11.982	21.7	0.997837	7911.743144	12.00797325
Flat 0.5mm #4	94.44	82.533	11.907	21.7	0.997837	7914.313117	11.93281067
Flat 0.5mm #5	94.857	82.898	11.959	21.7	0.997837	7914.693897	11.98492339
Angled 0.5mm #1	91.517	79.959	11.558	21.7	0.997837	7900.938634	11.58305415
Angled 0.5mm #2	91.485	79.939	11.546	21.7	0.997837	7906.384717	11.57102813
Angled 0.5mm #3	91.515	79.97	11.545	21.7	0.997837	7909.662456	11.57002597
Angled 0.5mm #4	91.677	80.126	11.551	21.7	0.997837	7919.54832	11.57603897
Angled 0.5mm #5	91.535	79.987	11.548	21.8	0.997815	7909.161415	11.57328763
Flat 1.0mm #1	98.681	86.264	12.417	21.9	0.997792	7929.702211	12.44447741
Flat 1.0mm #2	99.37	86.857	12.513	21.9	0.997792	7923.806524	12.54068984
Flat 1.0mm #3	99.214	86.721	12.493	21.9	0.997792	7924.032297	12.52064559
Flat 1.0mm #4	99.847	87.263	12.584	21.9	0.997792	7916.921315	12.61184696
Flat 1.0mm #5	99.174	86.675	12.499	21.9	0.997792	7917.035267	12.52665886
Angled 1.0mm #1	95.203	83.197	12.006	21.9	0.997792	7912.109926	12.03256791
Angled 1.0mm #2	95.602	83.536	12.066	21.9	0.997792	7905.76088	12.09270068
Angled 1.0mm #3	95.758	83.685	12.073	21.9	0.997792	7914.069936	12.09971617
Angled 1.0mm #4	95.129	83.126	12.003	22	0.99777	7907.761587	12.02982651
Angled 1.0mm #5	95.053	83.056	11.997	22	0.99777	7905.395666	12.0238131

Flat 1.5mm #1	101.641	88.836	12.805	22	0.99777	7919.901645	12.83361897
Flat 1.5mm #2	104.167	91.033	13.134	21.9	0.997792	7913.583011	13.16306405
Flat 1.5mm #3	103.862	90.76	13.102	21.9	0.997792	7909.683461	13.13099323
Flat 1.5mm #4	104.515	91.296	13.219	21.9	0.997792	7888.965193	13.24825214
Flat 1.5mm #5	104.437	91.259	13.178	21.9	0.997792	7907.603817	13.20716141
Angled 1.5mm #1	99.415	86.875	12.54	21.9	0.997792	7910.32629	12.56774959
Angled 1.5mm #2	100.034	87.42	12.614	22	0.99777	7912.710019	12.64219209
Angled 1.5mm #3	100.124	87.494	12.63	22	0.99777	7909.796	12.65822785
Angled 1.5mm #4	99.954	87.327	12.627	22	0.99777	7898.242067	12.65522114
Angled 1.5mm #5	100.03	87.412	12.618	22.1	0.997747	7909.702997	12.64649255
Flat 2.0mm #1	107.247	93.722	13.525	22.1	0.997747	7911.672644	13.55554063
Flat 2.0mm #2	109.073	95.292	13.781	22.1	0.997747	7896.905778	13.8121187
Flat 2.0mm #3	108.517	94.794	13.723	21.8	0.997815	7890.394983	13.75305042
Flat 2.0mm #4	108.594	94.889	13.705	21.9	0.997792	7906.18201	13.7353276
Flat 2.0mm #5	107.888	94.277	13.611	21.9	0.997792	7909.028234	13.64111959
Angled 2.0mm #1	103.981	90.875	13.106	21.9	0.997792	7916.329159	13.13500208
Angled 2.0mm #2	104.448	91.273	13.175	21.9	0.997792	7910.237481	13.20415477
Angled 2.0mm #3	104.384	91.219	13.165	21.9	0.997792	7911.395376	13.19413264
Angled 2.0mm #4	104.145	91.015	13.13	21.9	0.997792	7914.321998	13.15905519
Angled 2.0mm #5	104.496	91.306	13.19	22	0.99777	7904.698553	13.21947944
Flat 2.5mm #1	109.49	95.678	13.812	21.7	0.997837	7910.018327	13.84194012
Flat 2.5mm #2	112.388	98.182	14.206	21.8	0.997815	7894.018881	14.23710808
Flat 2.5mm #3	113.029	98.772	14.257	21.8	0.997815	7910.642606	14.28821976

Flat 2.5mm #4	112.61	98.404	14.206	21.8	0.997815	7909.611935	14.23710808
Angled 2.5mm #1	108.133	94.508	13.625	21.8	0.997815	7919.026011	13.65483582
Angled 2.5mm #2	108.523	94.795	13.728	21.8	0.997815	7887.957259	13.75806136
Angled 2.5mm #3	109.04	95.266	13.774	21.8	0.997815	7899.066909	13.80416209
Angled 2.5mm #4	108.561	94.863	13.698	21.8	0.997815	7908.000746	13.72799567
Angled 2.5mm #5	108.652	94.91	13.742	21.9	0.997792	7889.106126	13.77240948

A.2 Density of Deionized Water for varying temperatures

Density of Deionized Water for Varying Temperatures (°C)										
	0	0.1	0.2	0.3	0.4	0.5	0.6	0.7	0.8	0.9
15	0.9991	0.9991	0.9991	0.9991	0.9990	0.9990	0.9990	0.9990	0.9990	0.9990
16	0.9989	0.9989	0.9989	0.9989	0.9989	0.9989	0.9988	0.9988	0.9988	0.9988
17	0.9988	0.9988	0.9987	0.9987	0.9987	0.9987	0.9987	0.9987	0.9986	0.9986
18	0.9986	0.9986	0.9986	0.9985	0.9985	0.9985	0.9985	0.9985	0.9984	0.9984
19	0.9984	0.9984	0.9984	0.9983	0.9983	0.9983	0.9983	0.9983	0.9982	0.9982
20	0.9982	0.9982	0.9982	0.9981	0.9981	0.9981	0.9981	0.9981	0.9980	0.9980
21	0.9980	0.9980	0.9979	0.9979	0.9979	0.9979	0.9979	0.9978	0.9978	0.9978
22	0.9978	0.9977	0.9977	0.9977	0.9977	0.9977	0.9976	0.9976	0.9976	0.9976
23	0.9975	0.9975	0.9975	0.9975	0.9974	0.9974	0.9974	0.9974	0.9973	0.9973
24	0.9973	0.9973	0.9972	0.9972	0.9972	0.9972	0.9971	0.9971	0.9971	0.9971
25	0.9970	0.9970	0.9970	0.9970	0.9969	0.9969	0.9969	0.9969	0.9968	0.9968
26	0.9968	0.9968	0.9967	0.9967	0.9967	0.9966	0.9966	0.9966	0.9966	0.9965
27	0.9965	0.9965	0.9965	0.9964	0.9964	0.9964	0.9963	0.9963	0.9963	0.9963
28	0.9962	0.9962	0.9962	0.9961	0.9961	0.9961	0.9961	0.9960	0.9960	0.9960
29	0.9959	0.9959	0.9959	0.9959	0.9958	0.9958	0.9958	0.9957	0.9957	0.9957
30	0.9956	0.9956	0.9956	0.9956	0.9955	0.9955	0.9955	0.9954	0.9954	0.9954

A.3 Mode Shapes

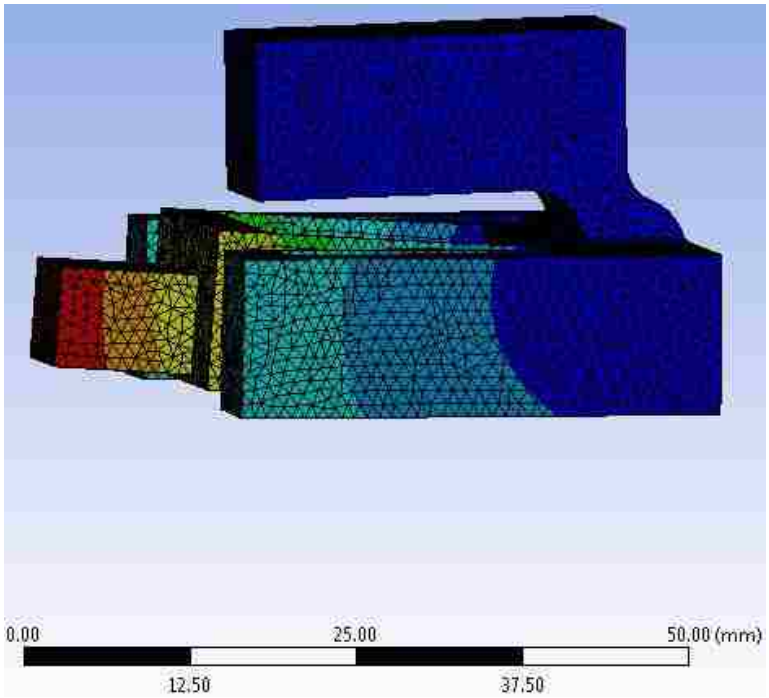

3rd Mode shape – 0.50mm Cantilever Thickness (3e-4 Scale)

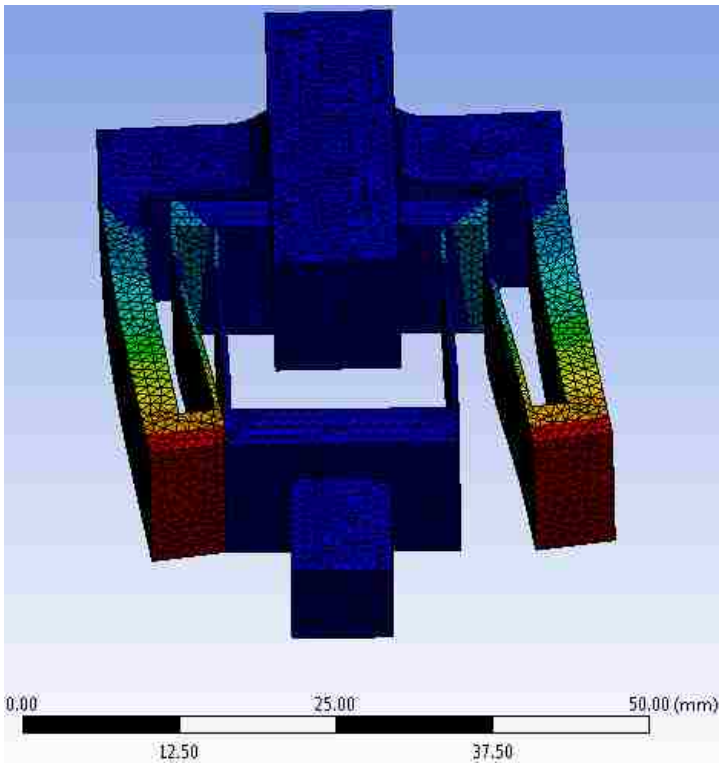

4th Mode shape – 0.50mm Cantilever Thickness (2.8e-4 Scale)

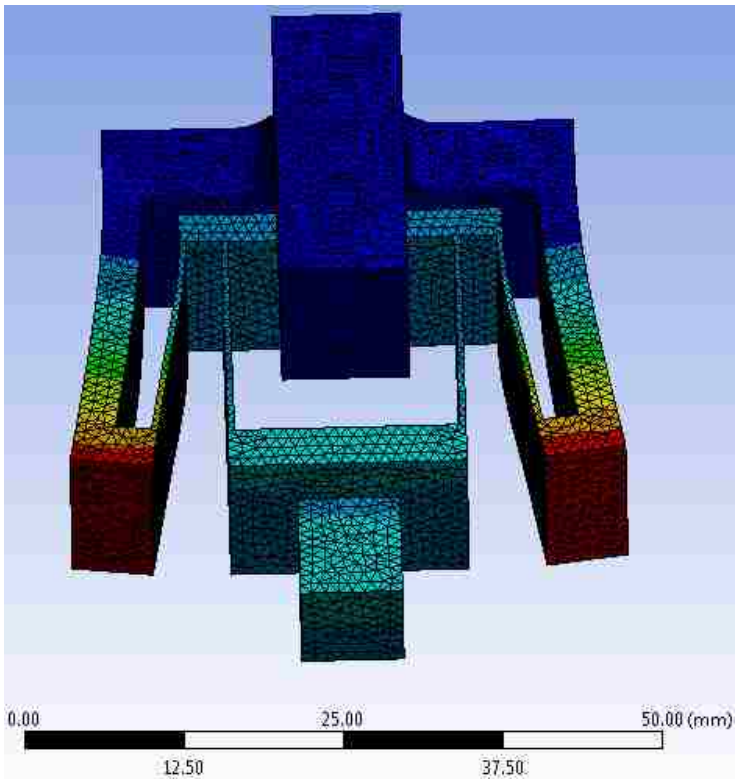

5th Mode shape – 0.50mm Cantilever Thickness (2.9e-4 Scale)

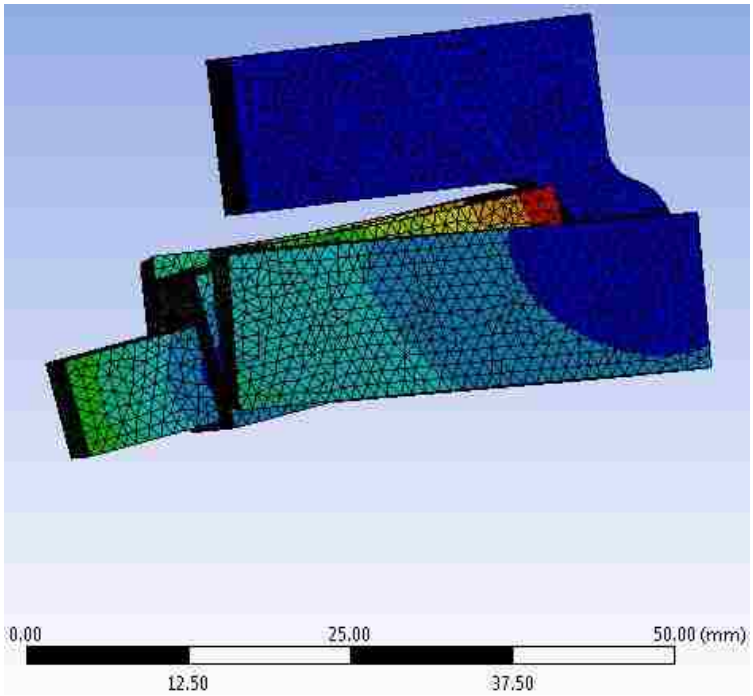

6th Mode shape – 0.50mm Cantilever Thickness (3.4e-4 Scale)

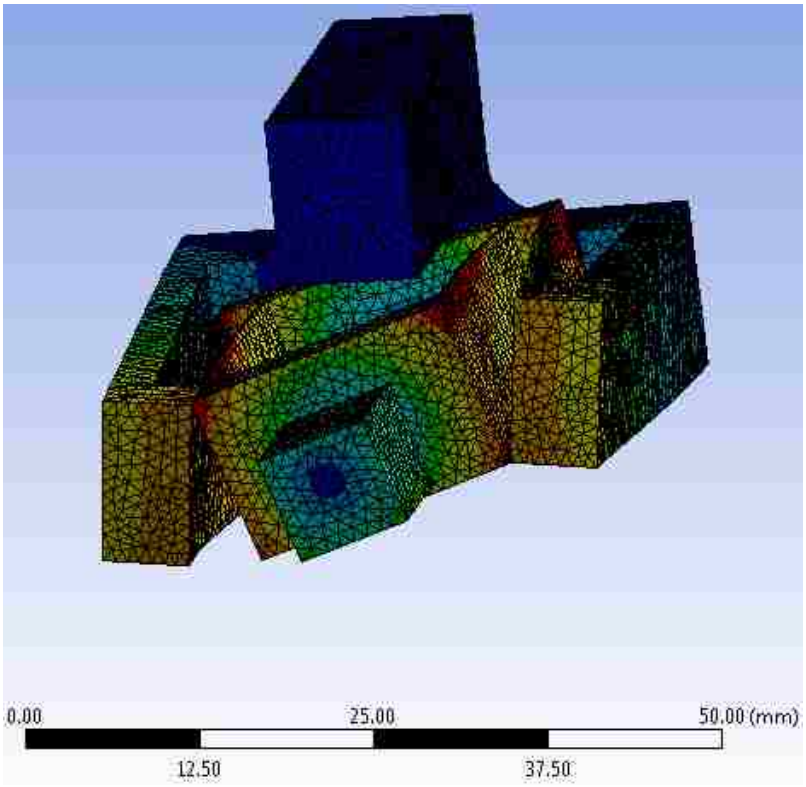

7th Mode shape – 0.50mm Cantilever Thickness (4.3e-4 Scale)

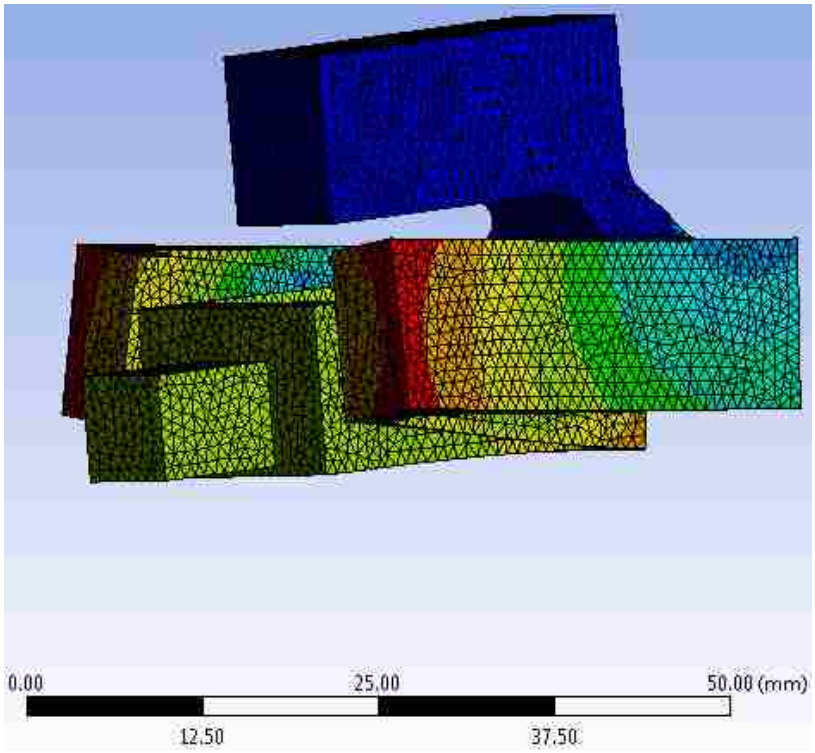

8th Mode shape – 0.50mm Cantilever Thickness (5.3e-4 Scale)

A.4 Frequency Domain Plots with Modal Frequencies

Angled Print Orientation – 0.5mm Cantilever Thickness –

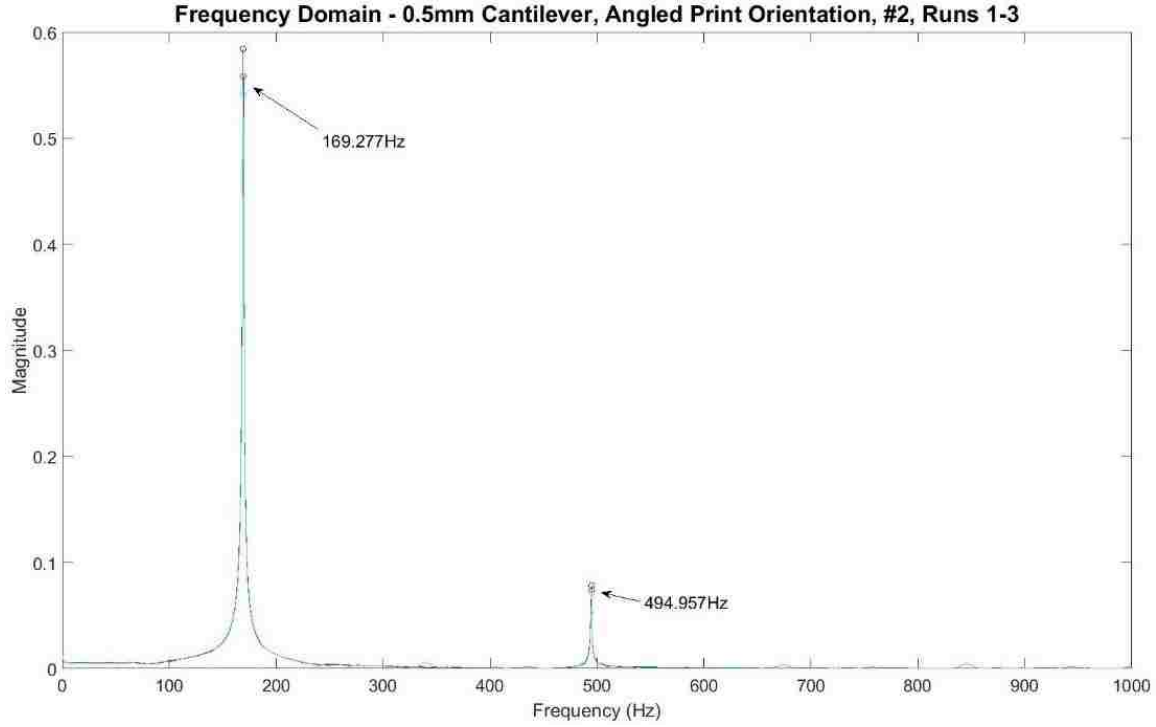

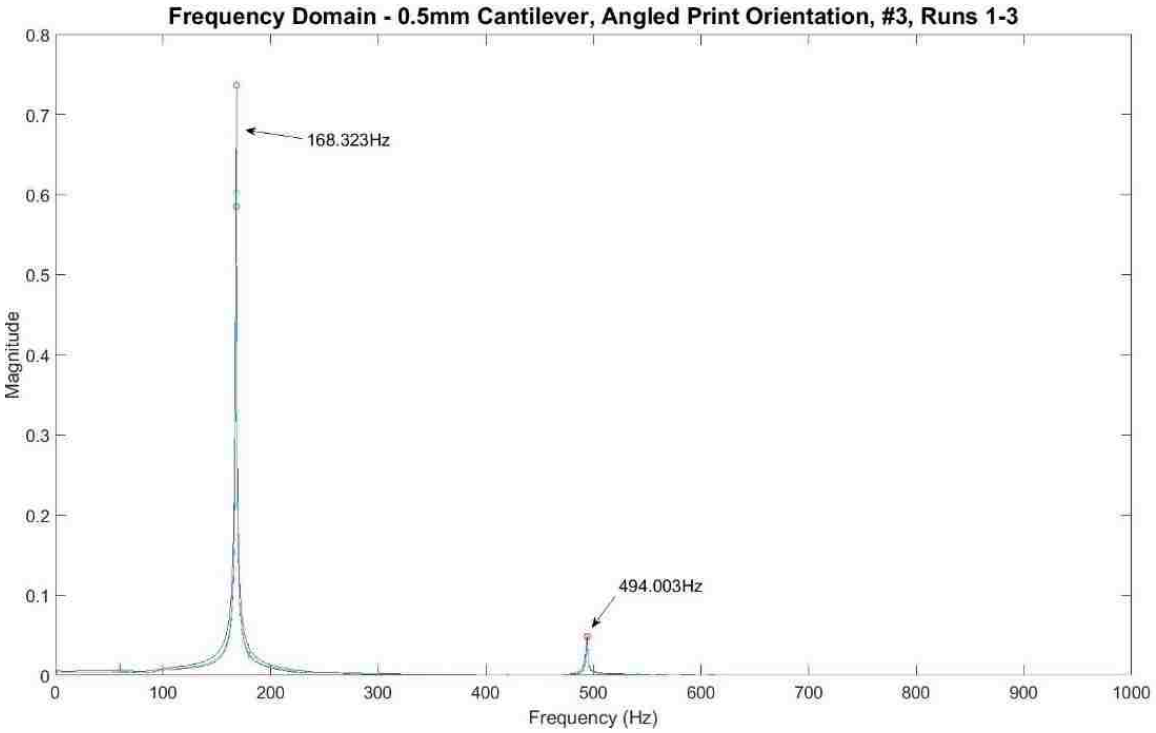

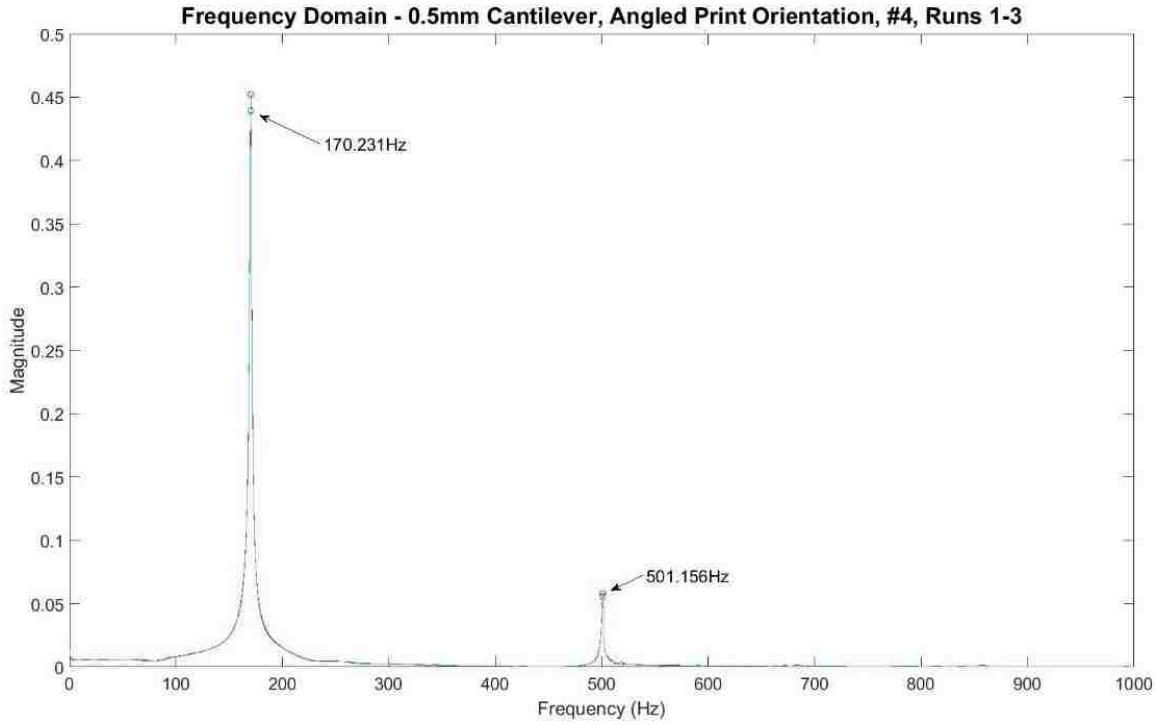
Frequency Domain - 0.5mm Cantilever, Angled Print Orientation, #4, Runs 1-3
170.231Hz
501.156Hz
Magnitude
Frequency (Hz)
0
0.05
0.1
0.15
0.2
0.25
0.3
0.35
0.4
0.45
0.5
0
100
200
300
400
500
600
700
800
900
1000

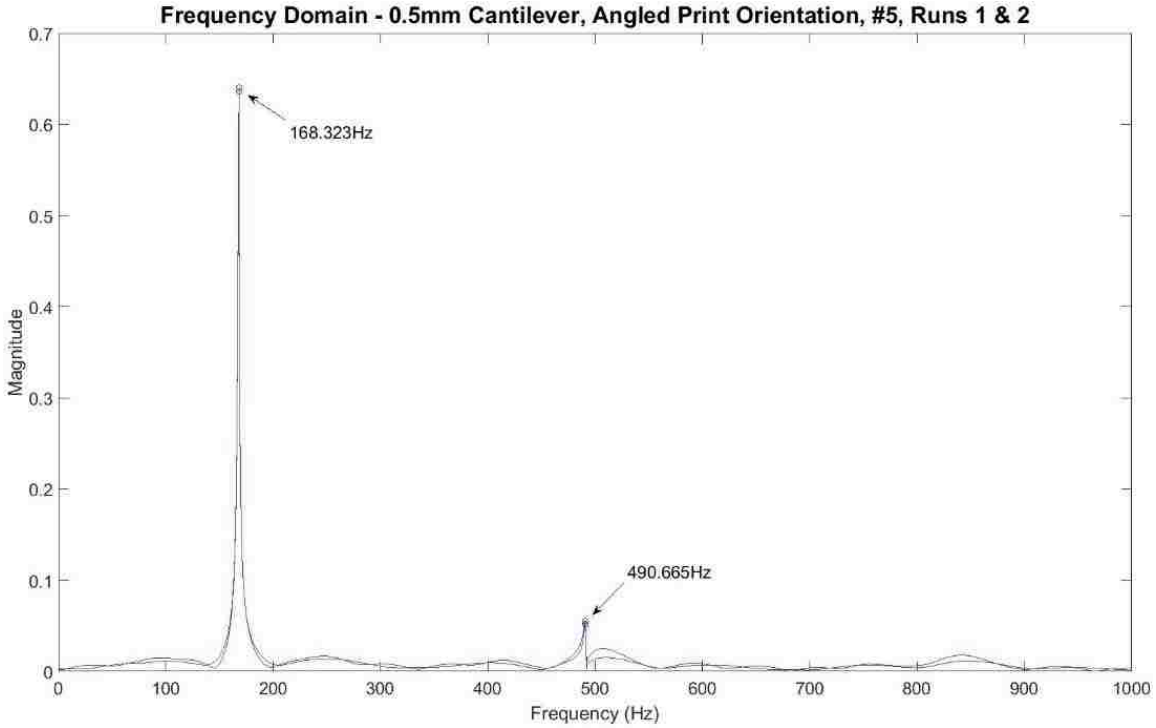
Frequency Domain - 0.5mm Cantilever, Angled Print Orientation, #5, Runs 1 & 2
168.323Hz
490.665Hz
Magnitude
Frequency (Hz)
0
0.1
0.2
0.3
0.4
0.5
0.6
0.7
0
100
200
300
400
500
600
700
800
900
1000

All angled 0.5mm coupons, all runs, overlaid –

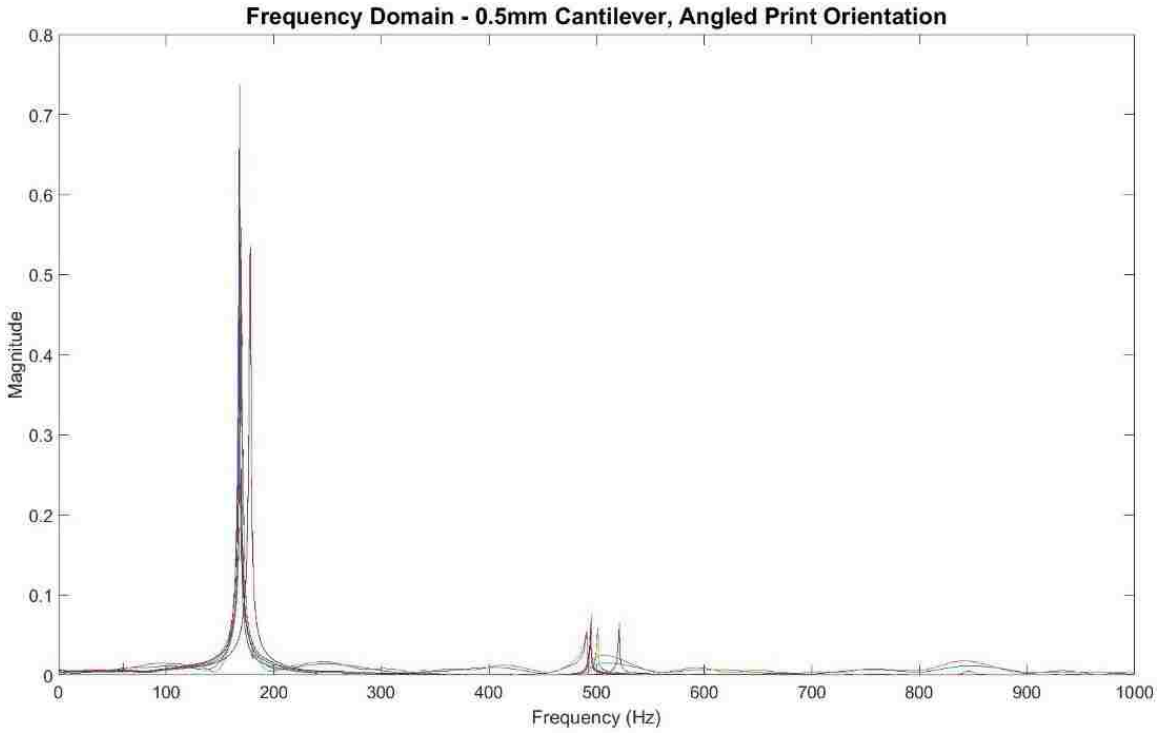

Flat Print Orientation – 0.5mm Cantilever Thickness –

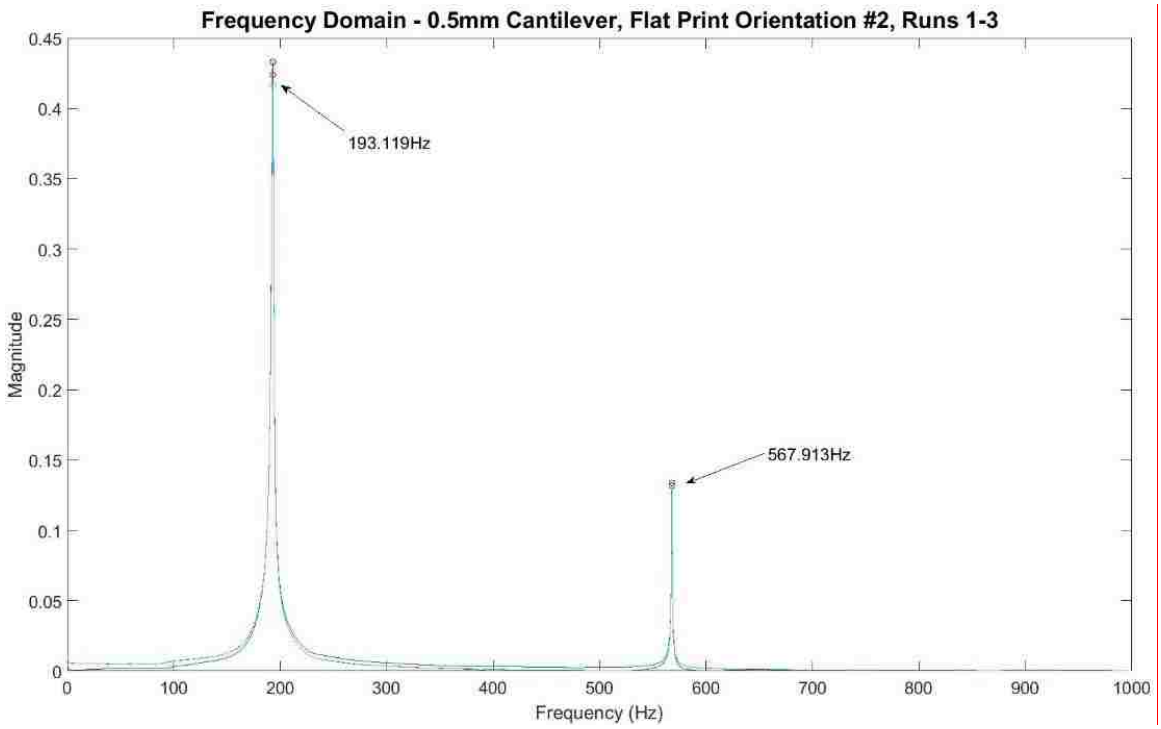

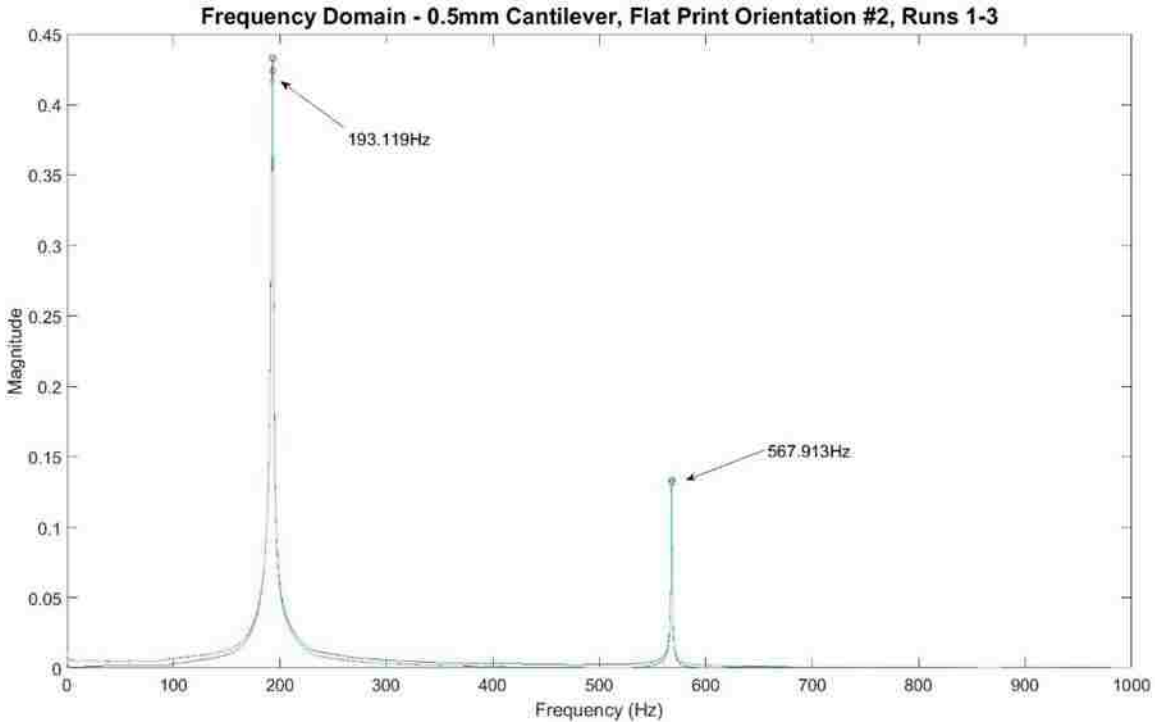
Frequency Domain - 0.5mm Cantilever, Flat Print Orientation #2, Runs 1-3
193.119Hz
567.913Hz
Magnitude
Frequency (Hz)
0.45
0.4
0.35
0.3
0.25
0.2
0.15
0.1
0.05
0
0
100
200
300
400
500
600
700
800
900
1000

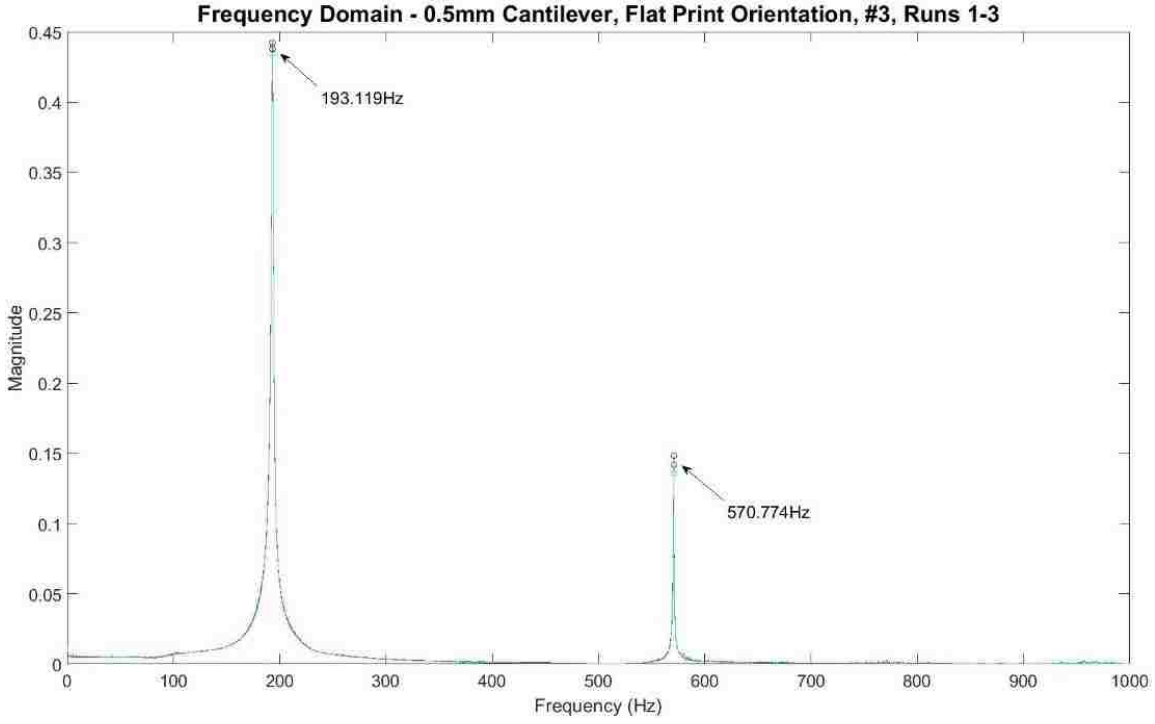
Frequency Domain - 0.5mm Cantilever, Flat Print Orientation, #3, Runs 1-3
193.119Hz
570.774Hz
Magnitude
Frequency (Hz)
0.45
0.4
0.35
0.3
0.25
0.2
0.15
0.1
0.05
0
0
100
200
300
400
500
600
700
800
900
1000

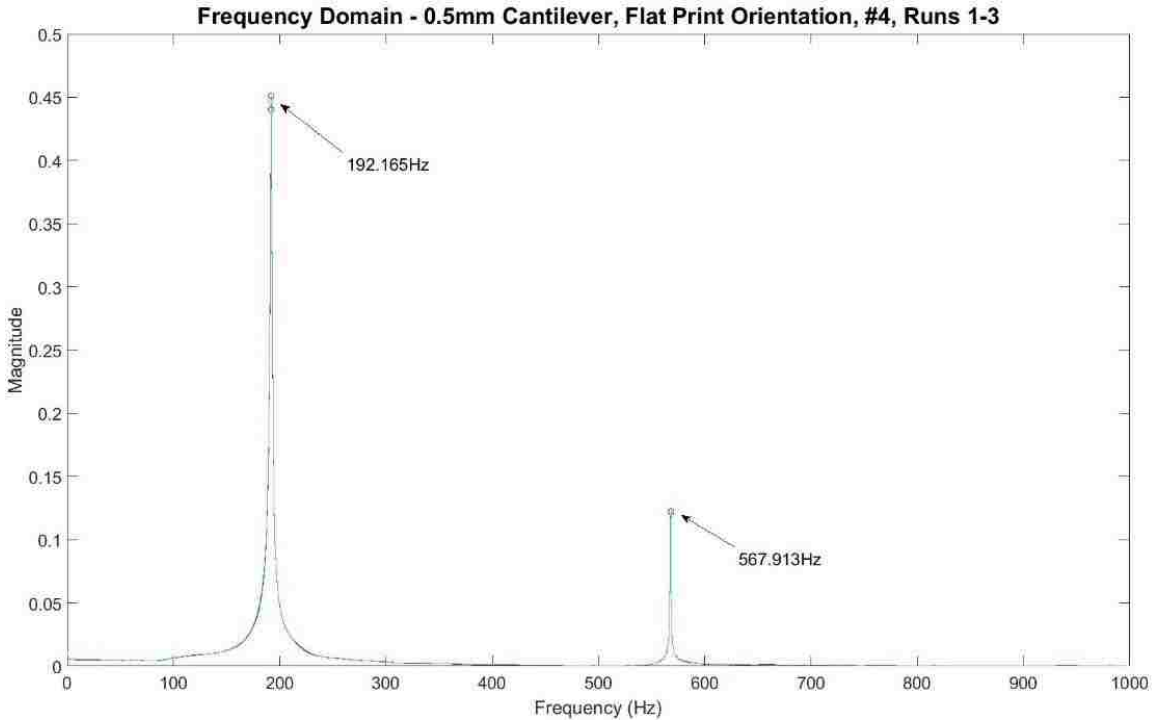
Frequency Domain - 0.5mm Cantilever, Flat Print Orientation, #4, Runs 1-3
192.165Hz
567.913Hz
Magnitude
Frequency (Hz)
0
0.05
0.1
0.15
0.2
0.25
0.3
0.35
0.4
0.45
0.5
0
100
200
300
400
500
600
700
800
900
1000

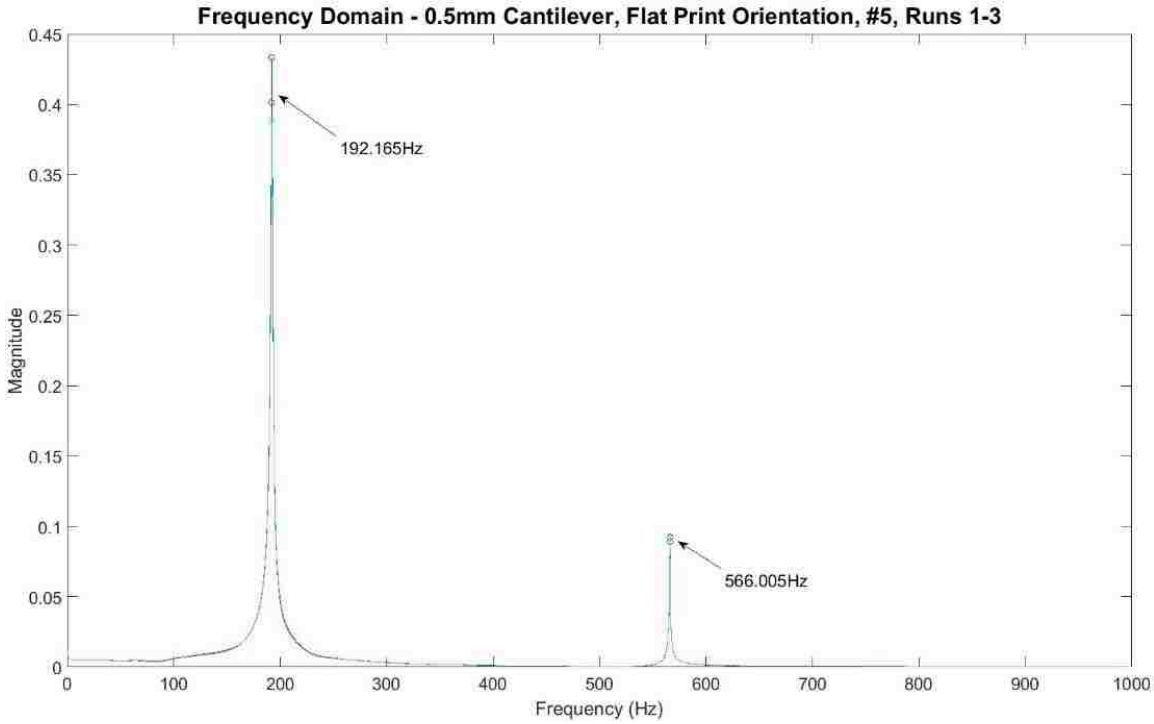
Frequency Domain - 0.5mm Cantilever, Flat Print Orientation, #5, Runs 1-3
192.165Hz
566.005Hz
Magnitude
Frequency (Hz)
0
0.05
0.1
0.15
0.2
0.25
0.3
0.35
0.4
0.45
0
100
200
300
400
500
600
700
800
900
1000

All flat 0.5mm coupons, all runs, overlaid –

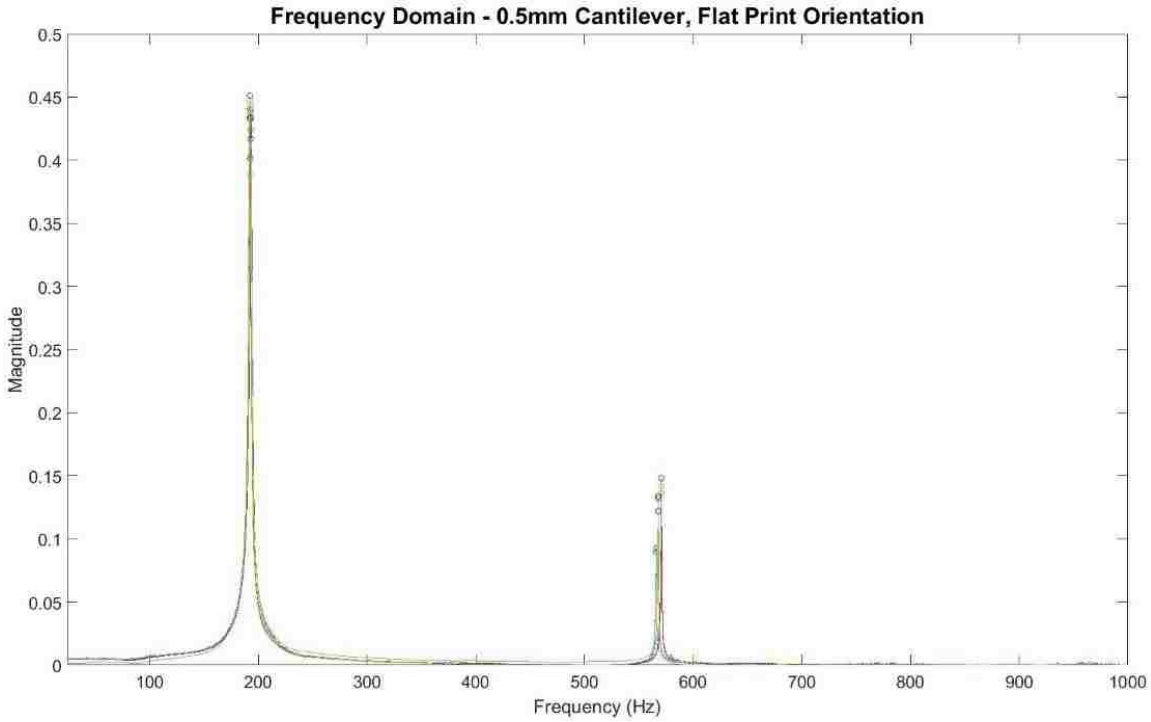

Angled Print Orientation – 1.0mm Cantilever Thickness –

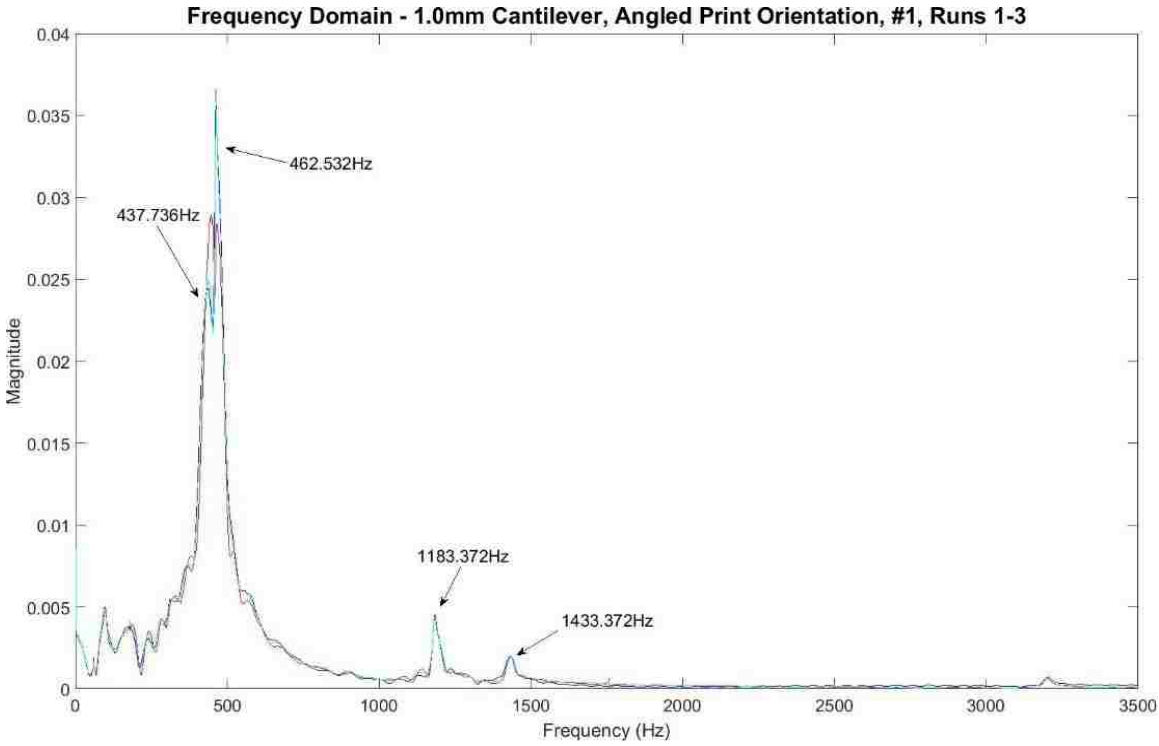

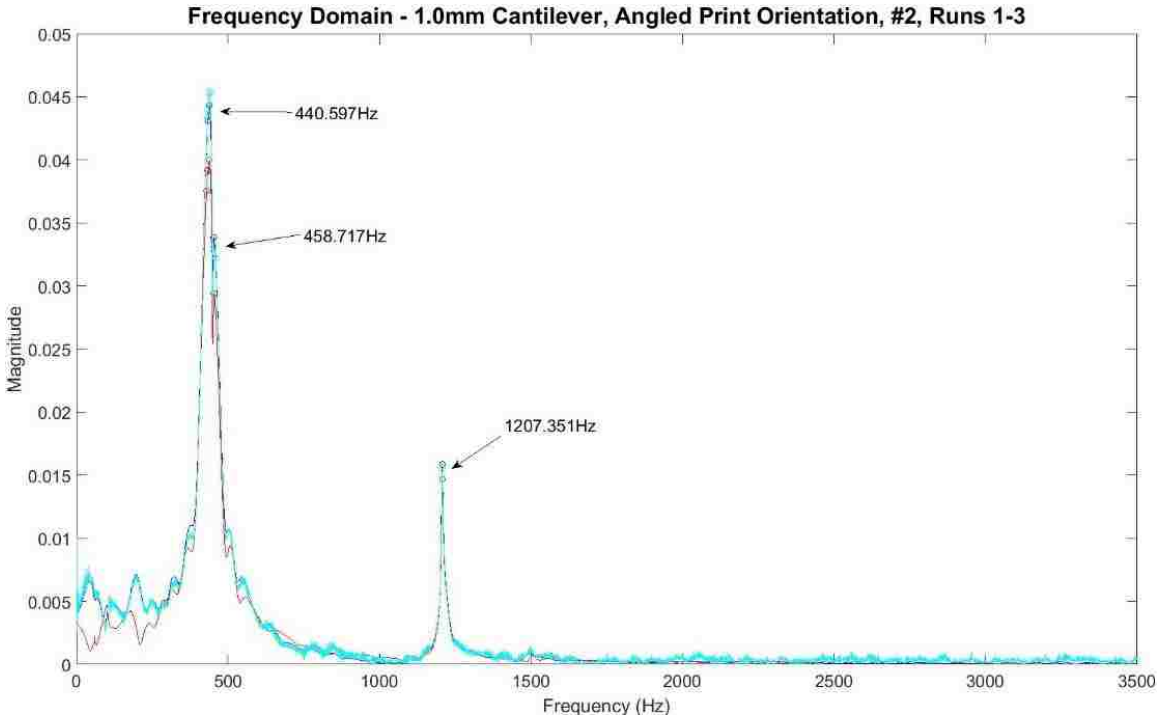
Frequency Domain - 1.0mm Cantilever, Angled Print Orientation, #2, Runs 1-3
440.597Hz
458.717Hz
1207.351Hz
Magnitude
Frequency (Hz)
0.05
0.045
0.04
0.035
0.03
0.025
0.02
0.015
0.01
0.005
0
0
500
1000
1500
2000
2500
3000
3500

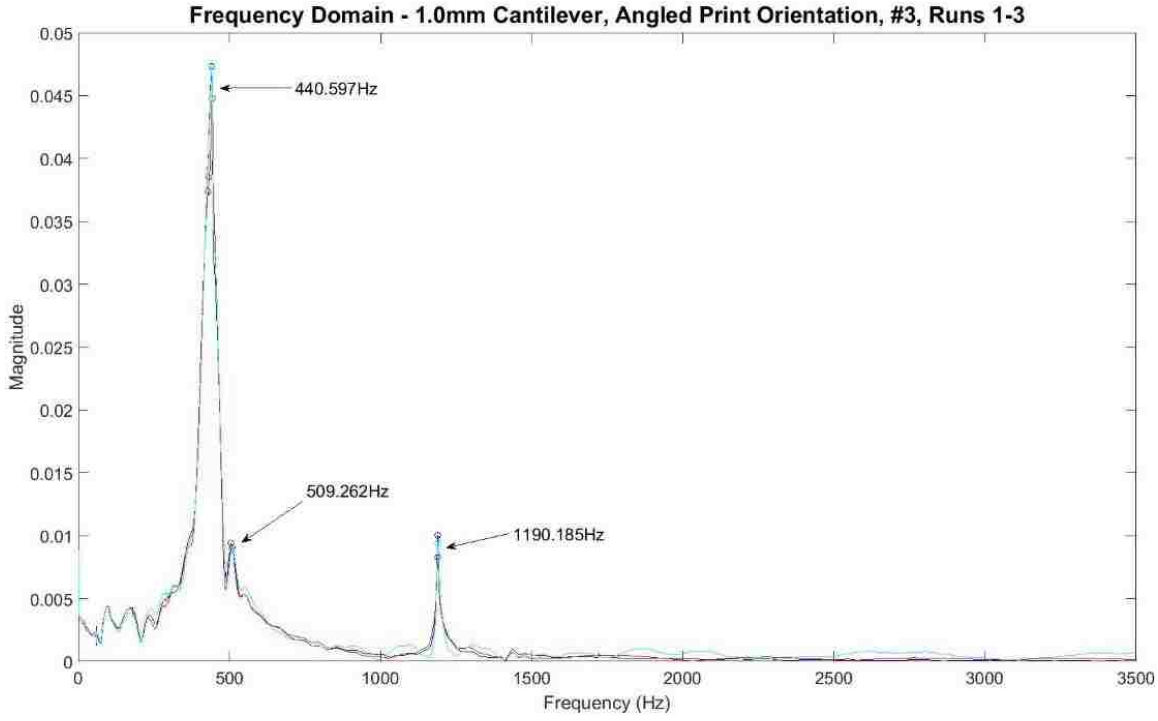
Frequency Domain - 1.0mm Cantilever, Angled Print Orientation, #3, Runs 1-3
440.597Hz
509.262Hz
1190.185Hz
Magnitude
Frequency (Hz)
0.05
0.045
0.04
0.035
0.03
0.025
0.02
0.015
0.01
0.005
0
0
500
1000
1500
2000
2500
3000
3500

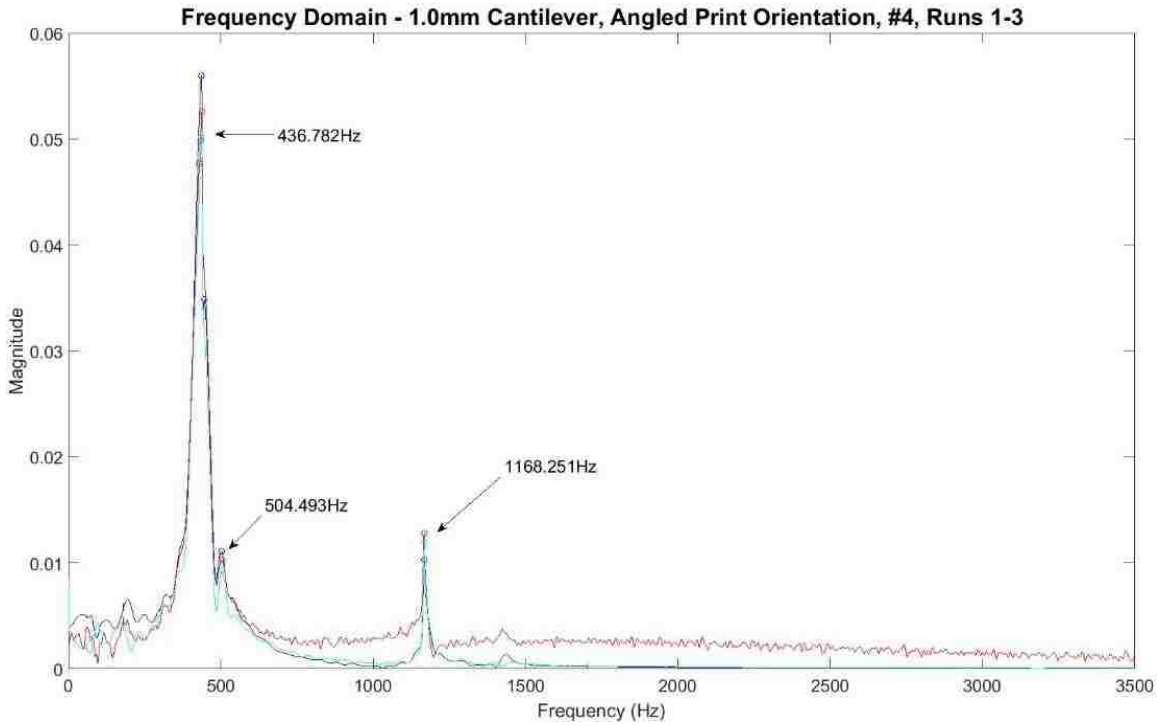
Frequency Domain - 1.0mm Cantilever, Angled Print Orientation, #4, Runs 1-3
436.782Hz
504.493Hz
1168.251Hz
Magnitude
Frequency (Hz)
0.06
0.05
0.04
0.03
0.02
0.01
0
0
500
1000
1500
2000
2500
3000
3500

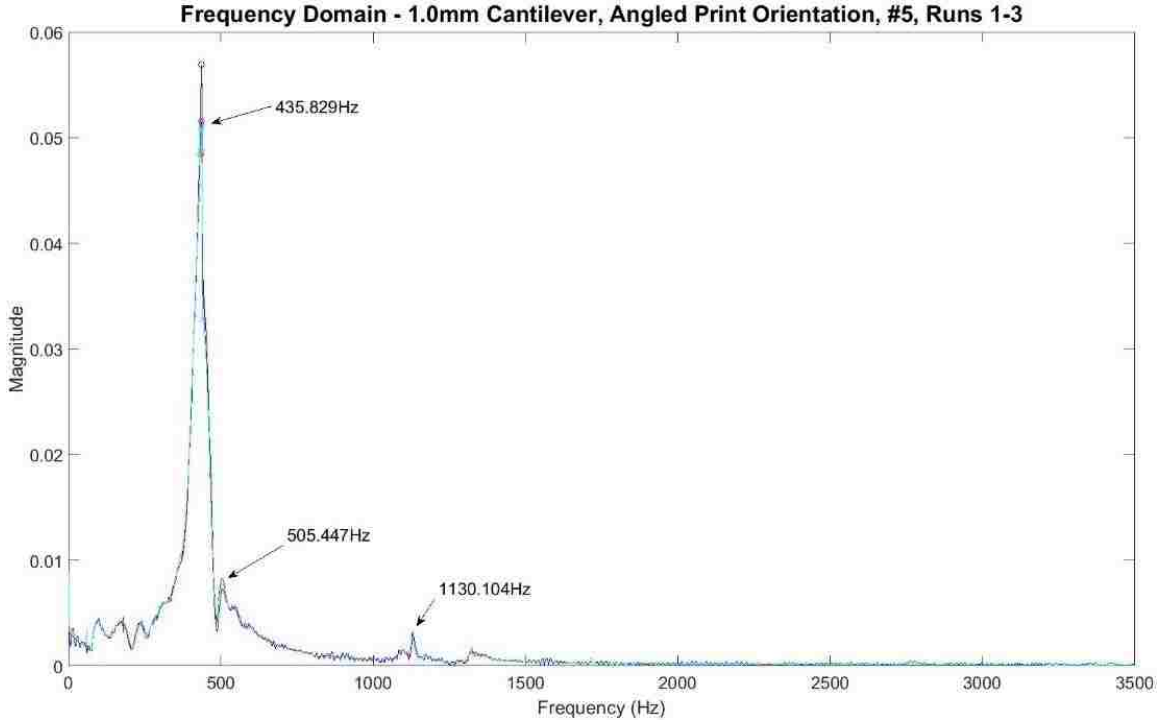
Frequency Domain - 1.0mm Cantilever, Angled Print Orientation, #5, Runs 1-3
435.829Hz
505.447Hz
1130.104Hz
Magnitude
Frequency (Hz)
0.06
0.05
0.04
0.03
0.02
0.01
0
0
500
1000
1500
2000
2500
3000
3500

All angled 1.0mm coupons, all runs, overlaid –

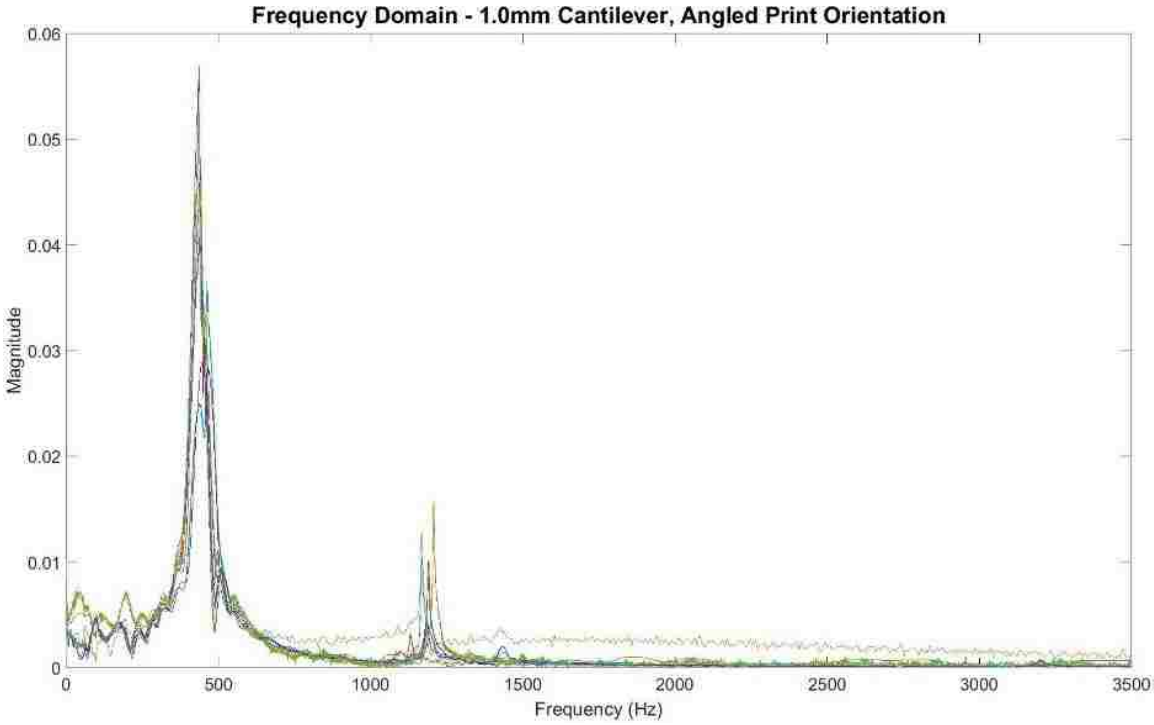

Flat Print Orientation, 1.0mm Cantilever Thickness –

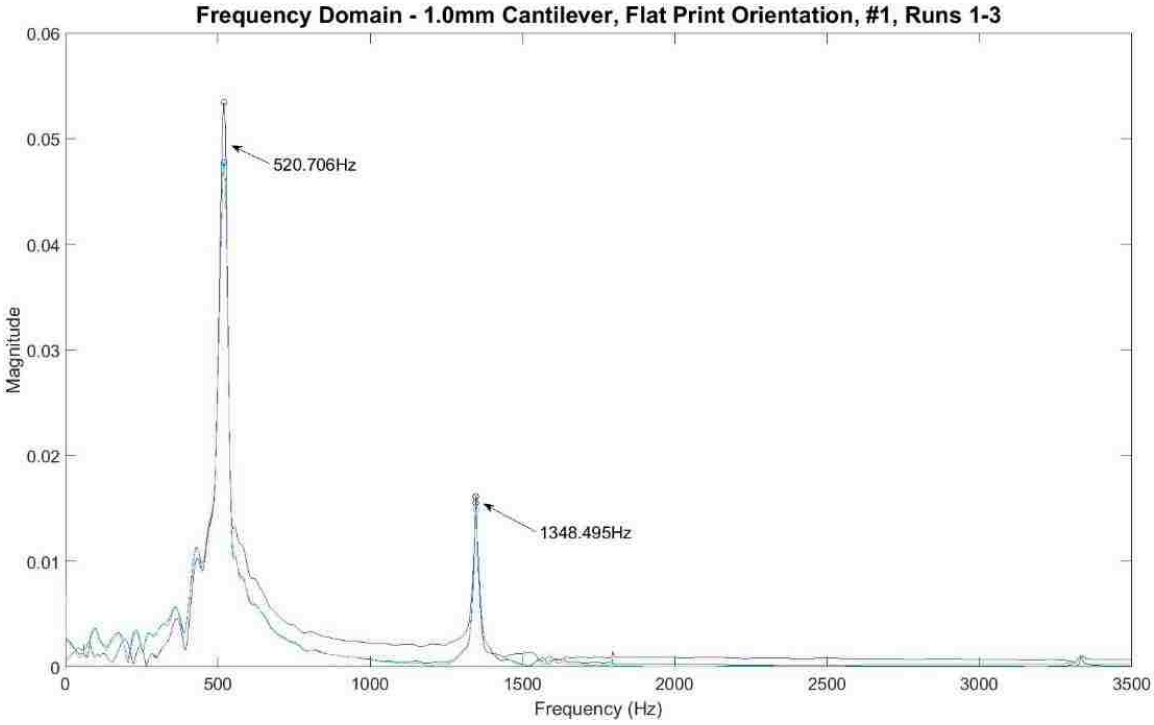

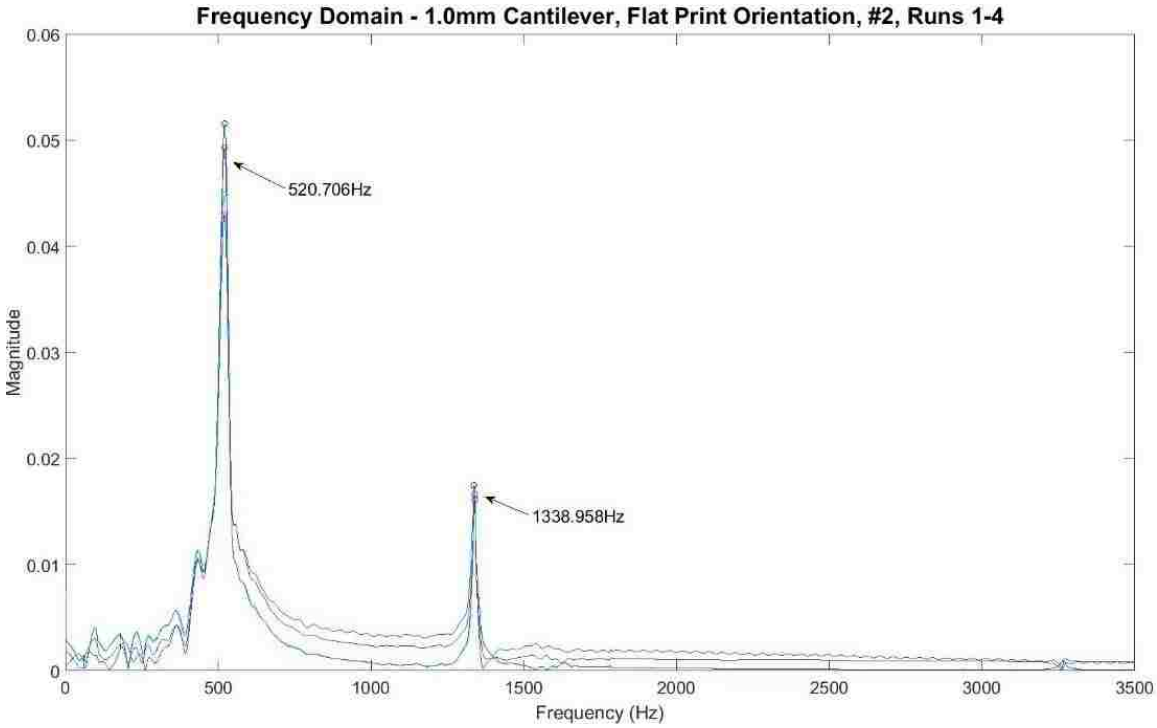
Frequency Domain - 1.0mm Cantilever, Flat Print Orientation, #2, Runs 1-4
520.706Hz
1338.958Hz
Magnitude
Frequency (Hz)
0.06
0.05
0.04
0.03
0.02
0.01
0
0
500
1000
1500
2000
2500
3000
3500

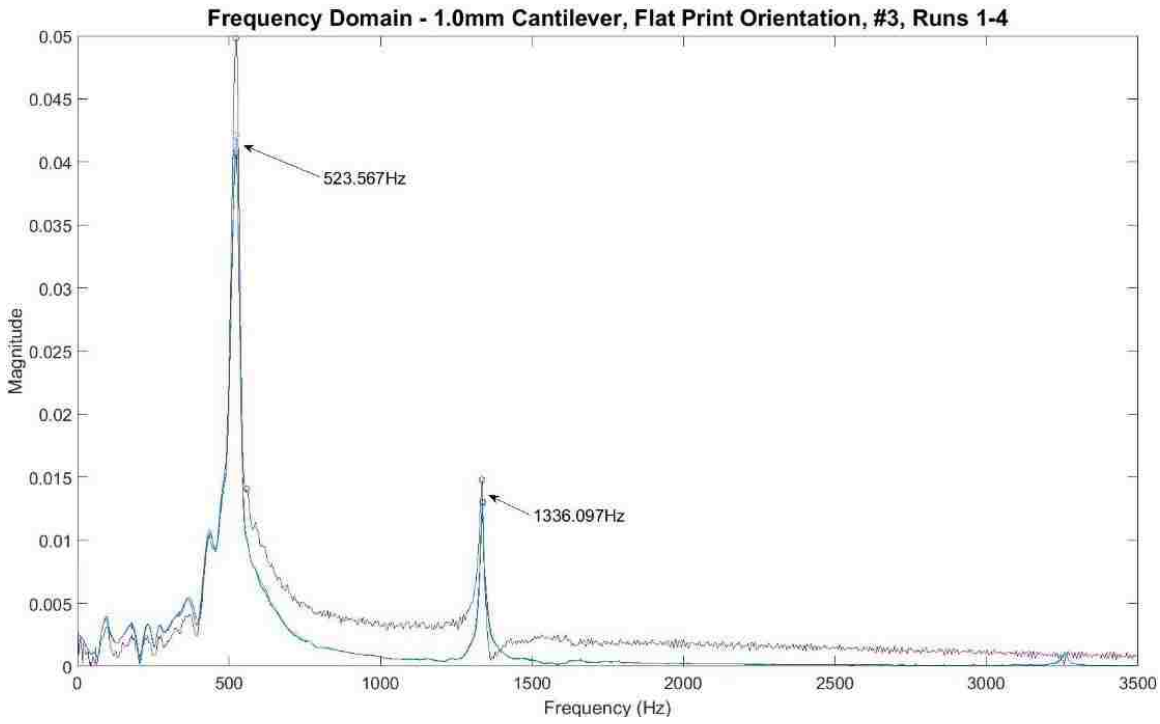
Frequency Domain - 1.0mm Cantilever, Flat Print Orientation, #3, Runs 1-4
523.567Hz
1336.097Hz
Magnitude
Frequency (Hz)
0.05
0.045
0.04
0.035
0.03
0.025
0.02
0.015
0.01
0.005
0
0
500
1000
1500
2000
2500
3000
3500

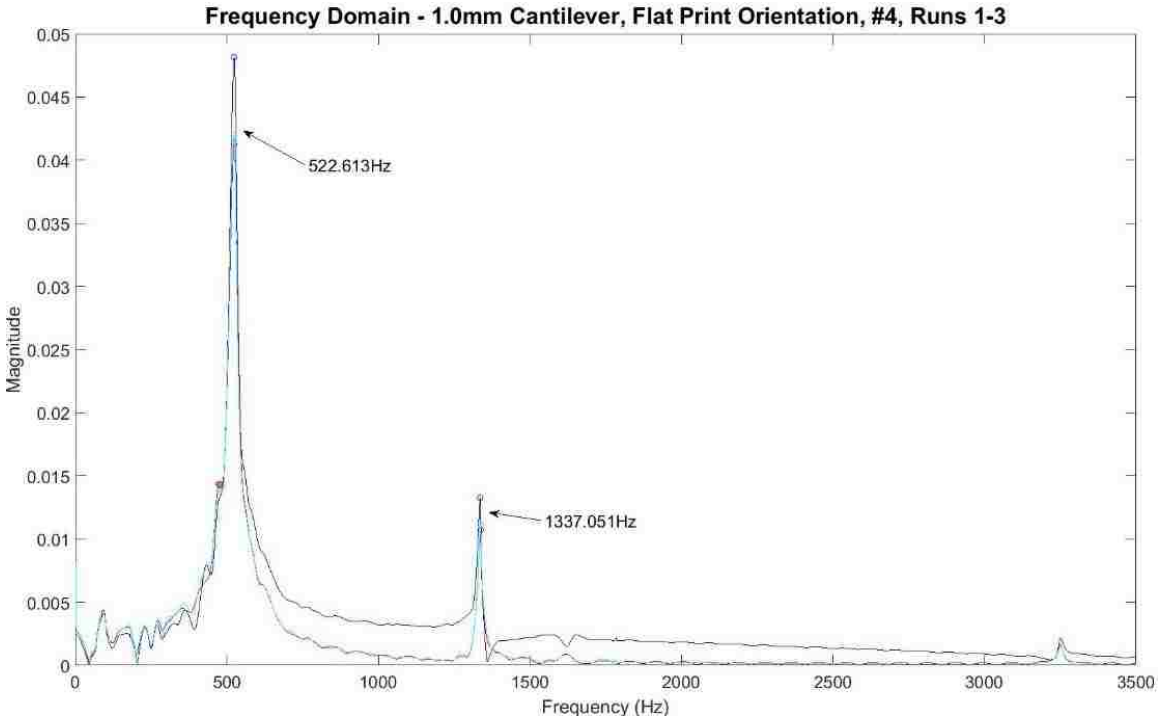
Frequency Domain - 1.0mm Cantilever, Flat Print Orientation, #4, Runs 1-3
522.613Hz
1337.051Hz
Magnitude
Frequency (Hz)
0.05
0.045
0.04
0.035
0.03
0.025
0.02
0.015
0.01
0.005
0
0
500
1000
1500
2000
2500
3000
3500

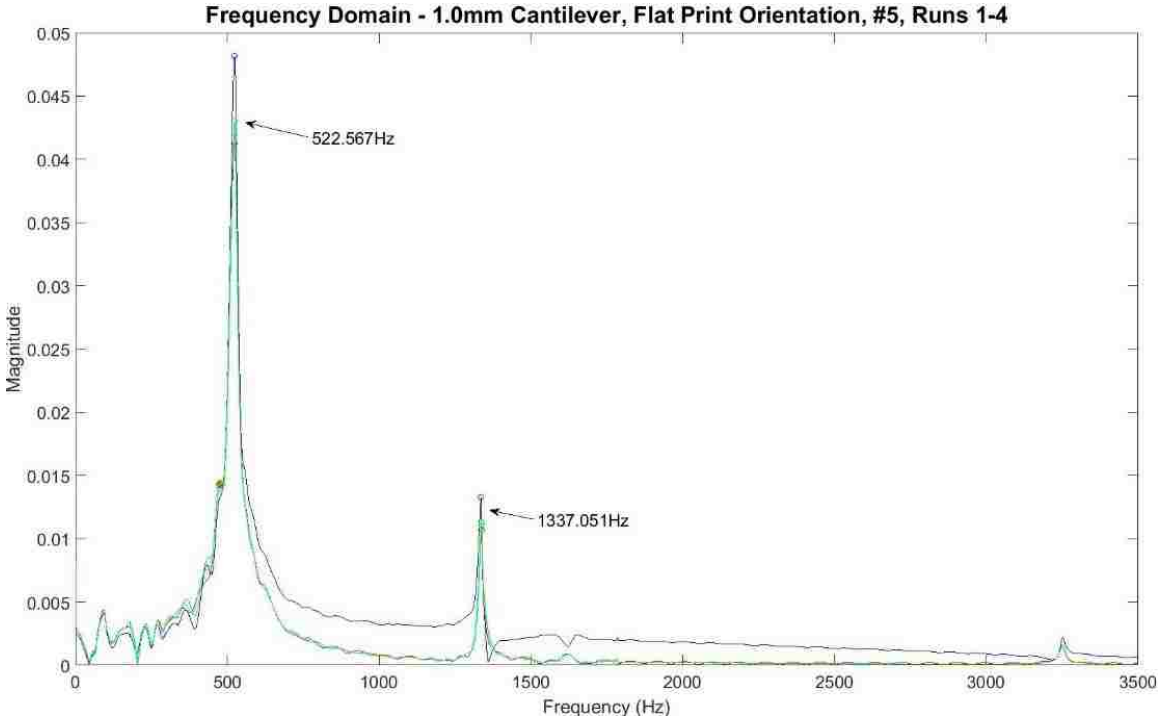
Frequency Domain - 1.0mm Cantilever, Flat Print Orientation, #5, Runs 1-4
522.567Hz
1337.051Hz
Magnitude
Frequency (Hz)
0.05
0.045
0.04
0.035
0.03
0.025
0.02
0.015
0.01
0.005
0
0
500
1000
1500
2000
2500
3000
3500

All flat 1.0mm coupons, all runs, overlaid –

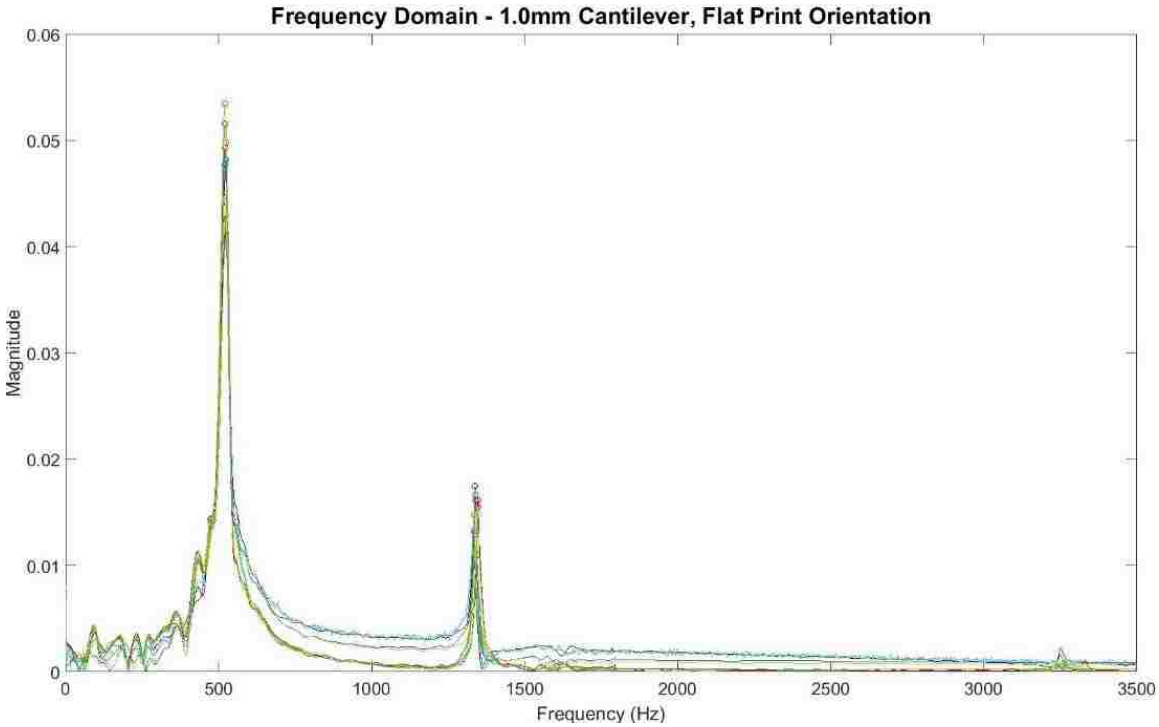

Angled Print Orientation – 1.5mm Cantilever Thickness –

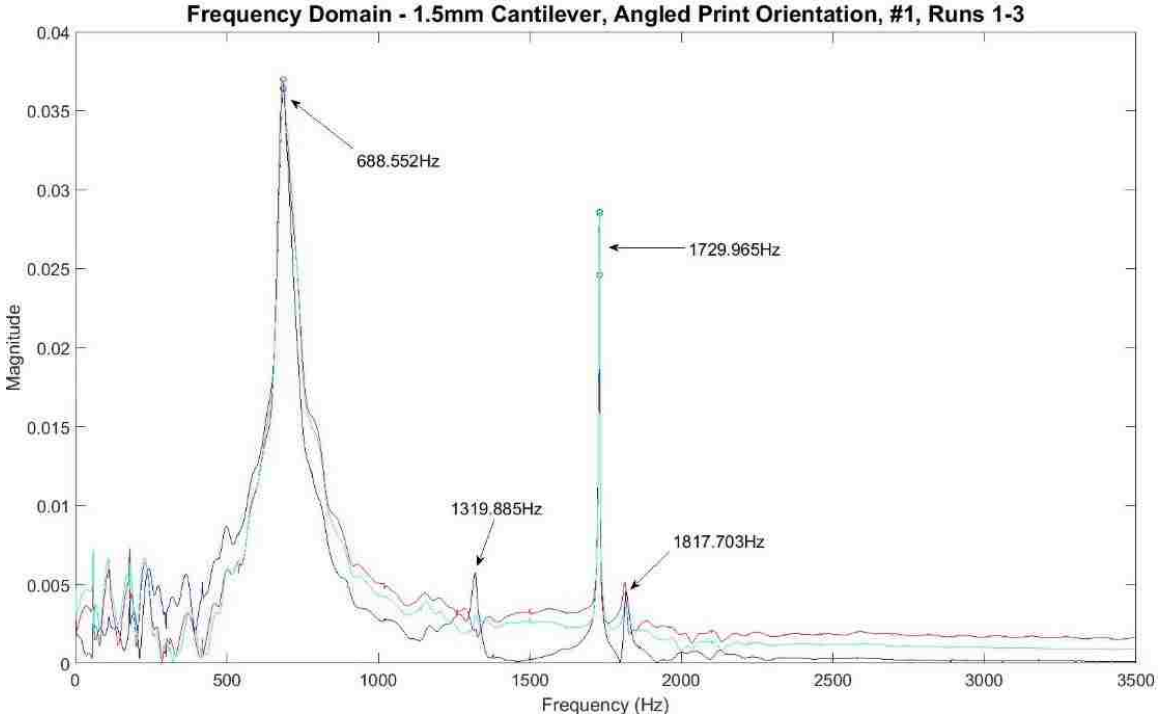

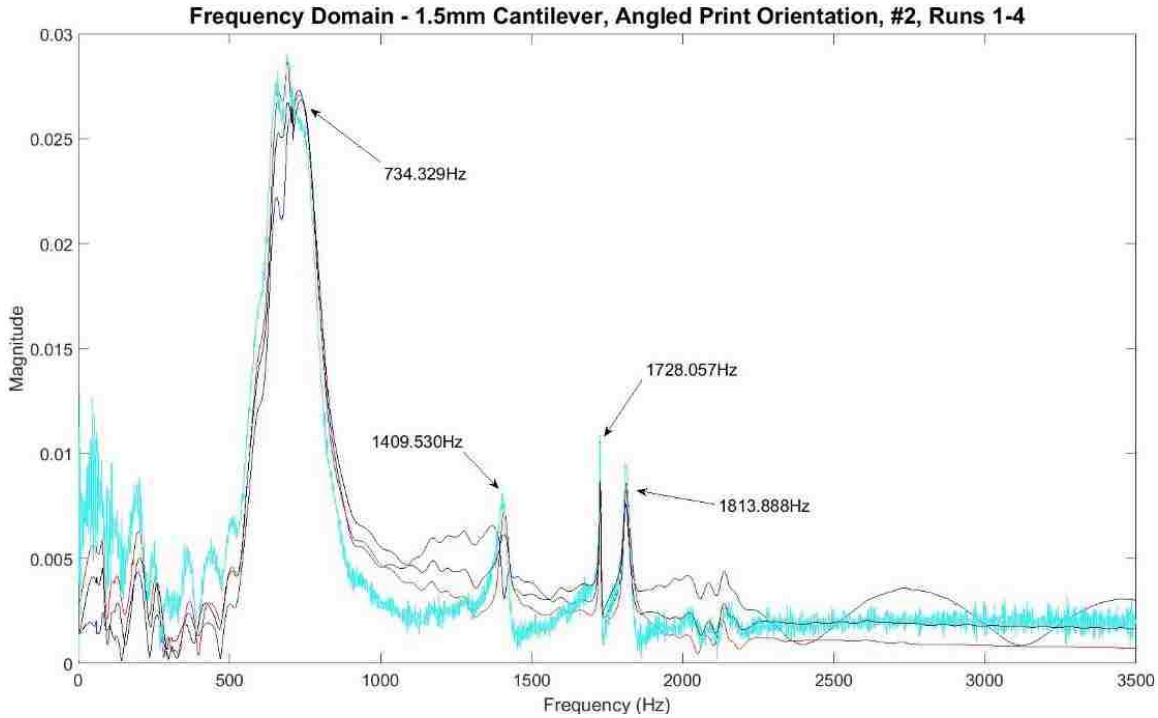
Frequency Domain - 1.5mm Cantilever, Angled Print Orientation, #2, Runs 1-4
734.329Hz
1728.057Hz
1409.530Hz
1813.888Hz
Magnitude
Frequency (Hz)
0.03
0.025
0.02
0.015
0.01
0.005
0
0
500
1000
1500
2000
2500
3000
3500

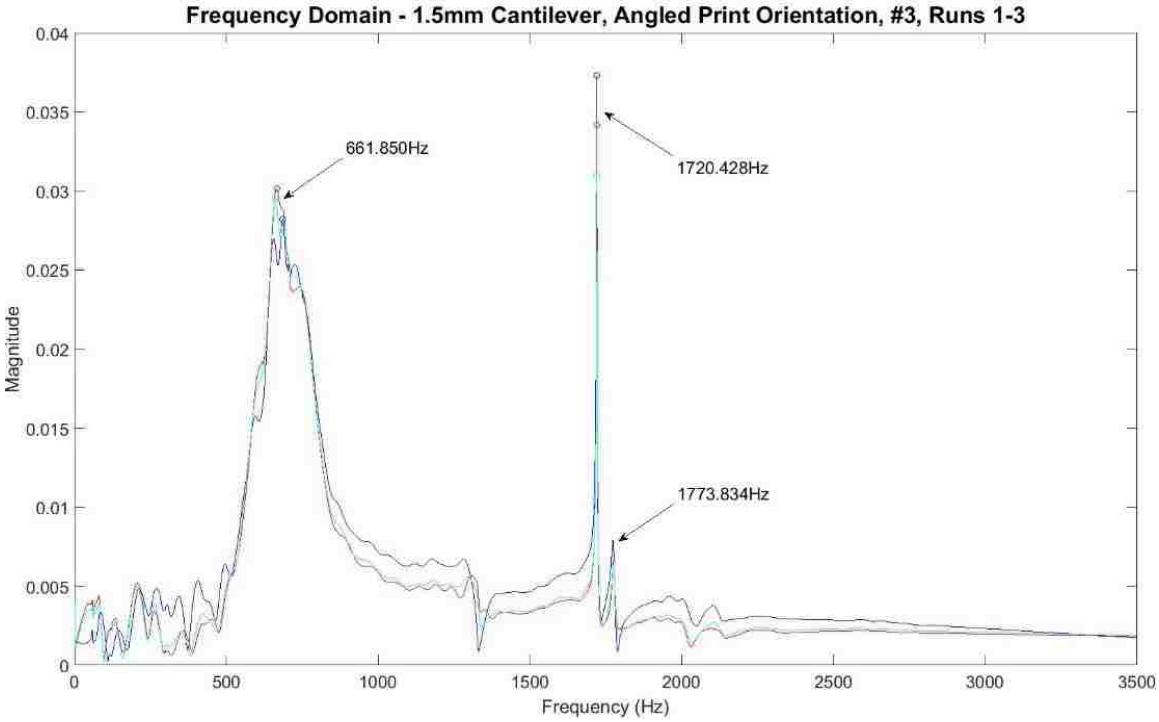
Frequency Domain - 1.5mm Cantilever, Angled Print Orientation, #3, Runs 1-3
661.850Hz
1720.428Hz
1773.834Hz
Magnitude
Frequency (Hz)
0.04
0.035
0.03
0.025
0.02
0.015
0.01
0.005
0
0
500
1000
1500
2000
2500
3000
3500

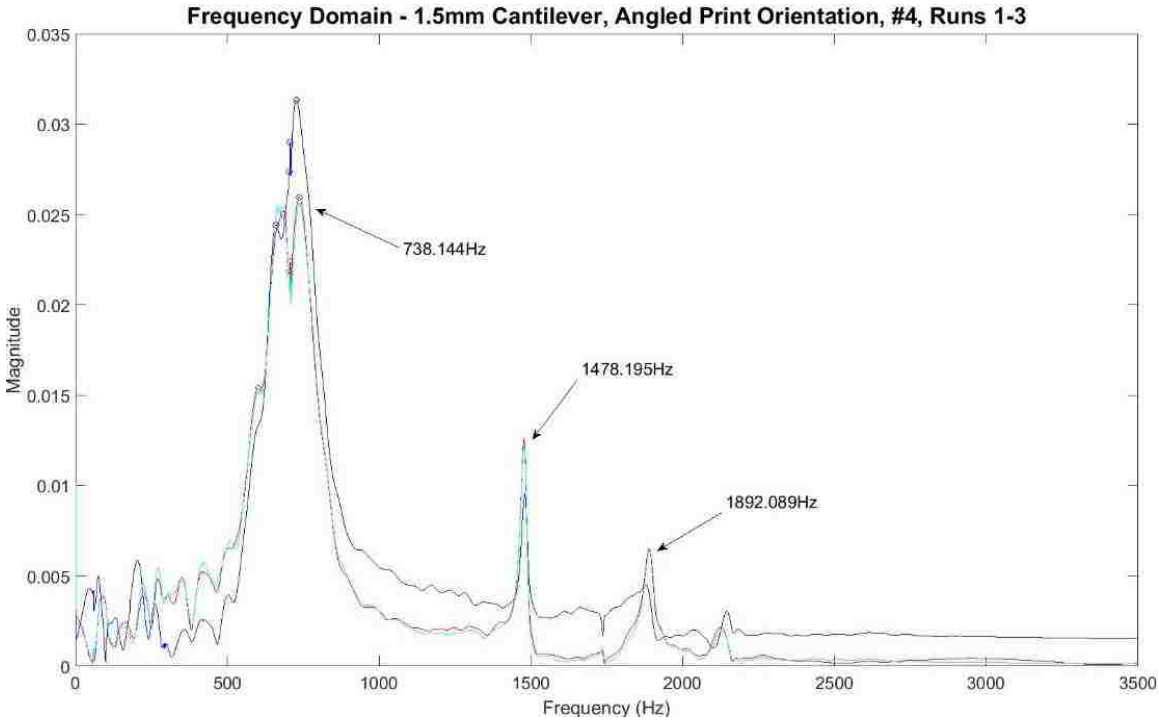
Frequency Domain - 1.5mm Cantilever, Angled Print Orientation, #4, Runs 1-3
Magnitude
Frequency (Hz)
738.144Hz
1478.195Hz
1892.089Hz
0.035
0.03
0.025
0.02
0.015
0.01
0.005
0
0
500
1000
1500
2000
2500
3000
3500

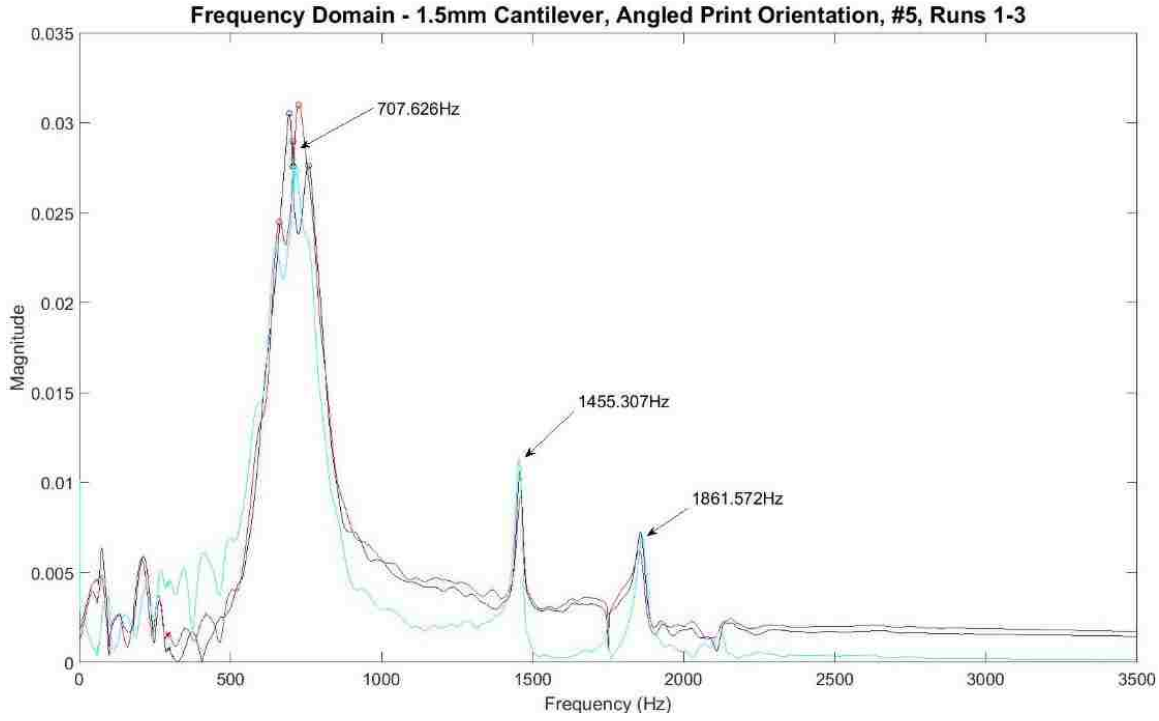
Frequency Domain - 1.5mm Cantilever, Angled Print Orientation, #5, Runs 1-3
Magnitude
Frequency (Hz)
707.626Hz
1455.307Hz
1861.572Hz
0.035
0.03
0.025
0.02
0.015
0.01
0.005
0
0
500
1000
1500
2000
2500
3000
3500

All angled 1.5mm coupons, all runs, overlaid –

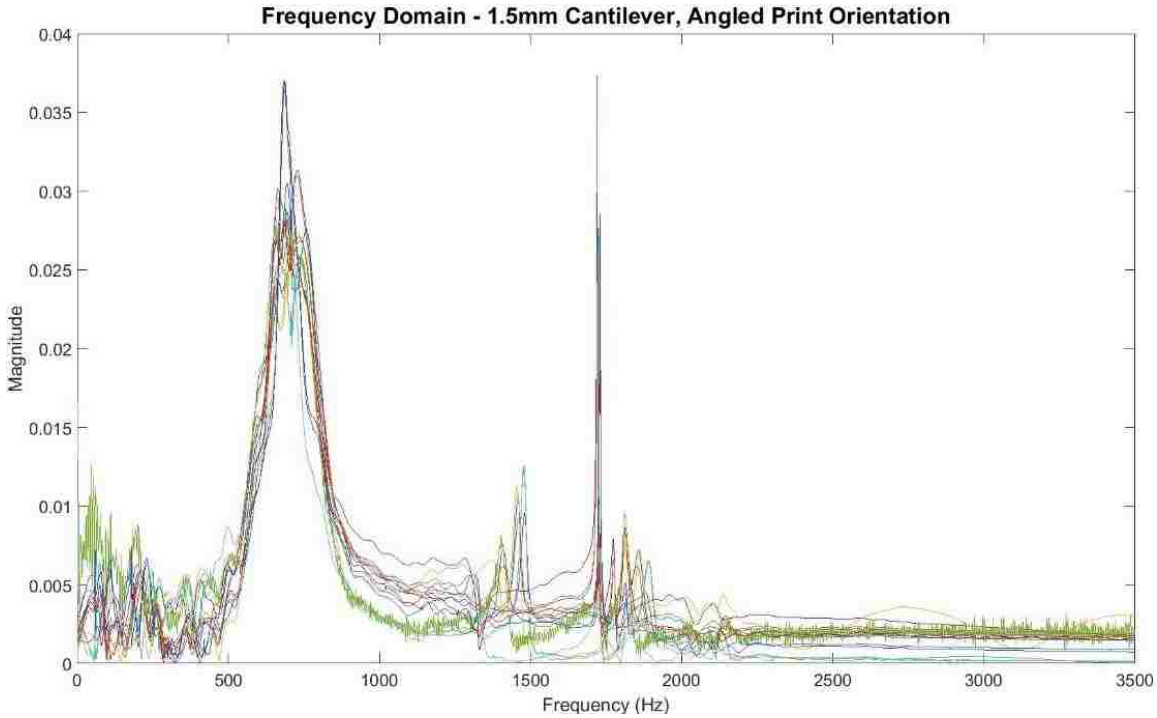

Flat Print Orientation – 1.5mm Cantilever Thickness –

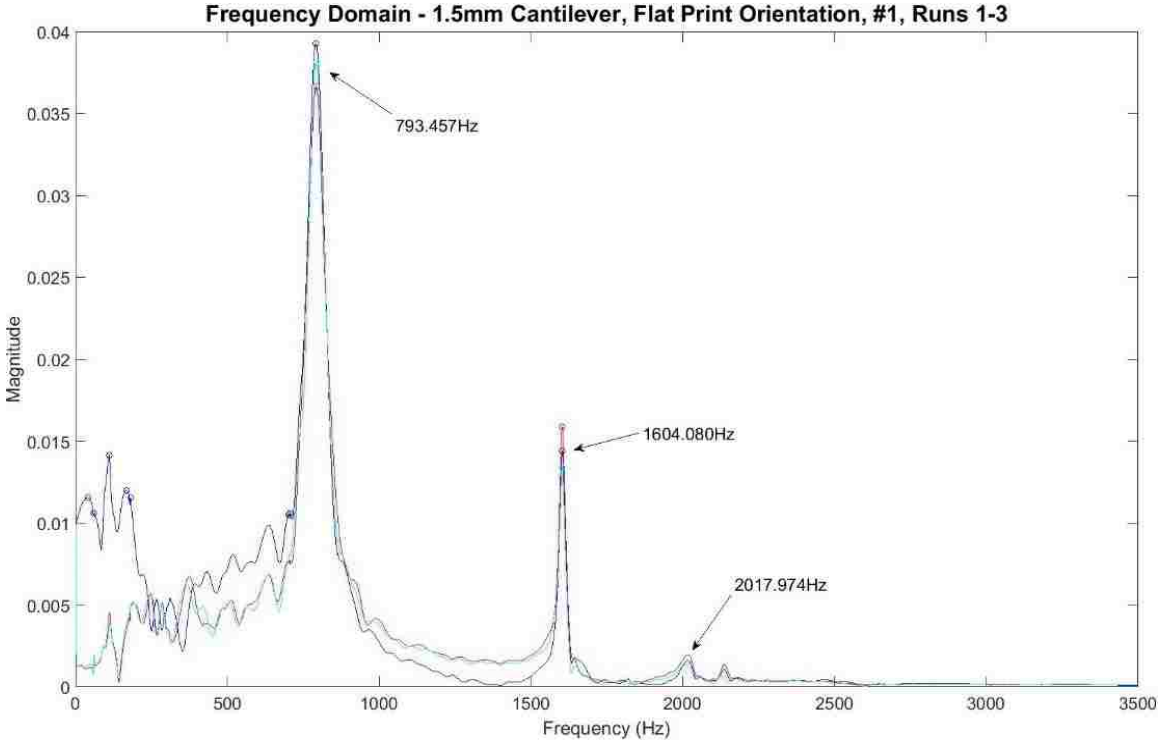

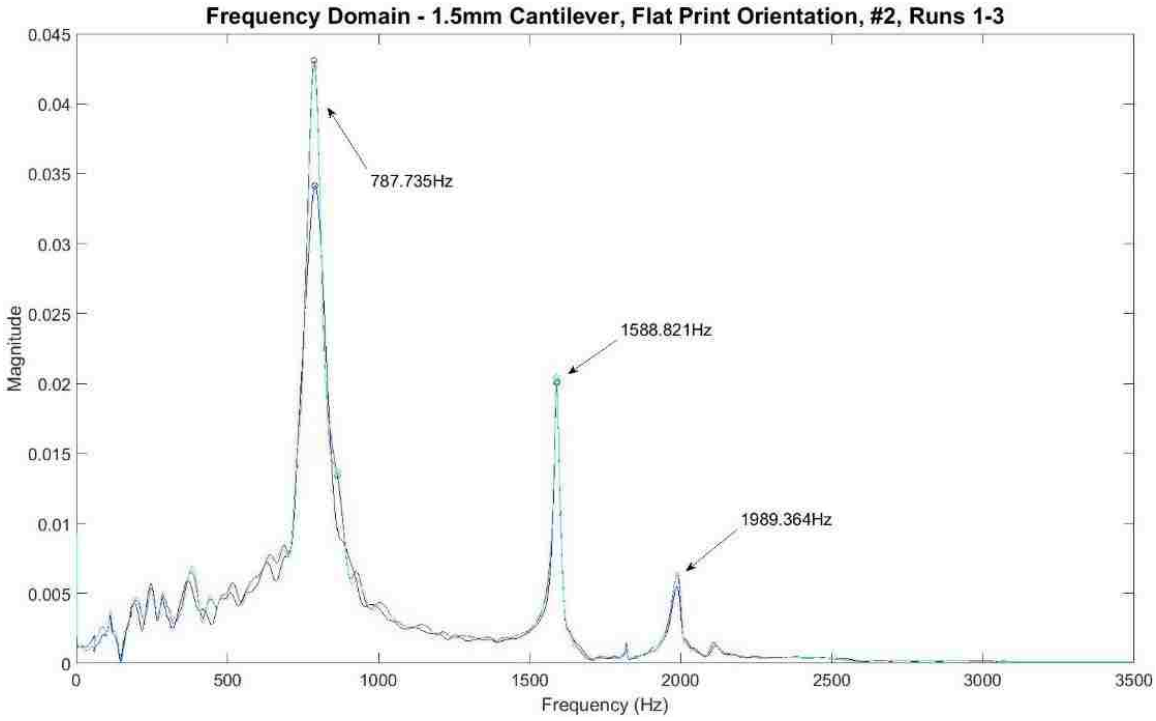
Frequency Domain - 1.5mm Cantilever, Flat Print Orientation, #2, Runs 1-3
787.735Hz
1588.821Hz
1989.364Hz
Magnitude
Frequency (Hz)
0.045
0.04
0.035
0.03
0.025
0.02
0.015
0.01
0.005
0
0
500
1000
1500
2000
2500
3000
3500

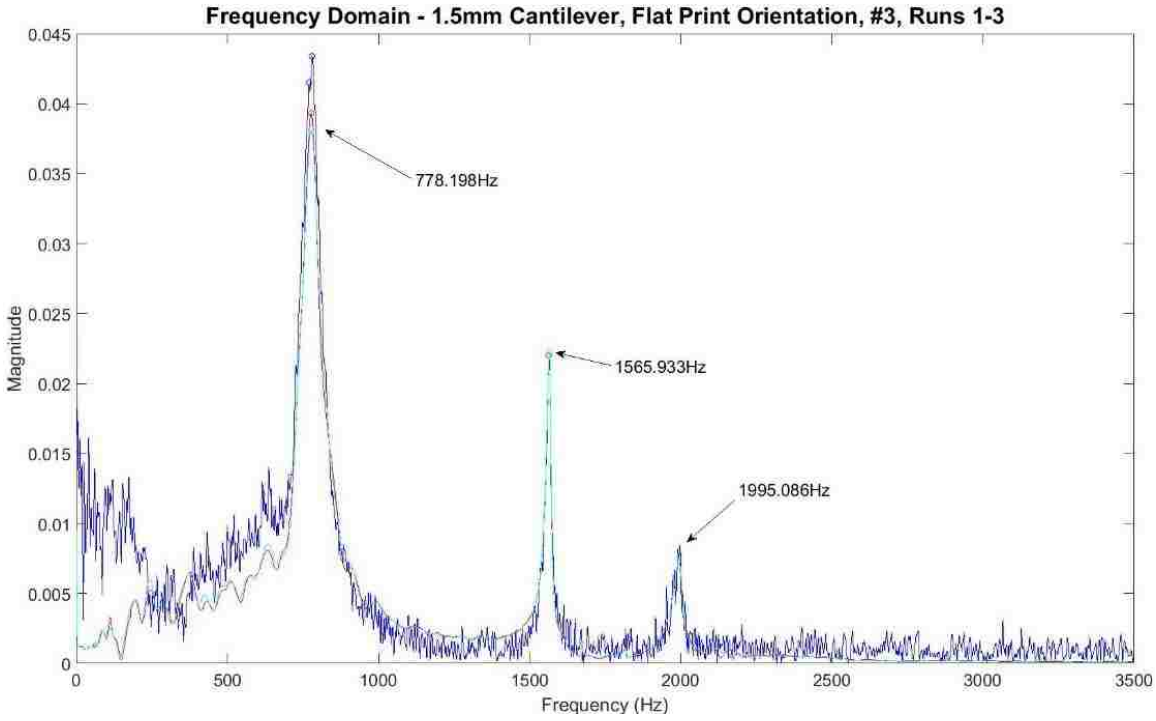
Frequency Domain - 1.5mm Cantilever, Flat Print Orientation, #3, Runs 1-3
778.198Hz
1565.933Hz
1995.086Hz
Magnitude
Frequency (Hz)
0.045
0.04
0.035
0.03
0.025
0.02
0.015
0.01
0.005
0
0
500
1000
1500
2000
2500
3000
3500

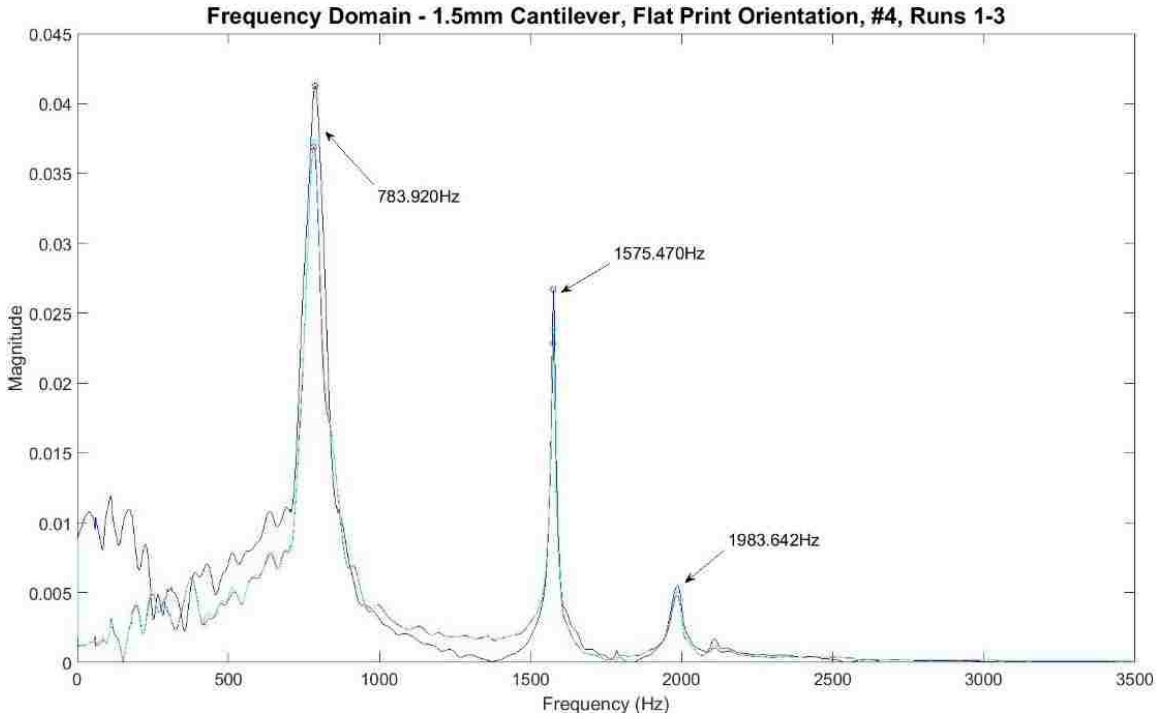
Frequency Domain - 1.5mm Cantilever, Flat Print Orientation, #4, Runs 1-3
783.920Hz
1575.470Hz
1983.642Hz
Magnitude
Frequency (Hz)
0.045
0.04
0.035
0.03
0.025
0.02
0.015
0.01
0.005
0
0
500
1000
1500
2000
2500
3000
3500

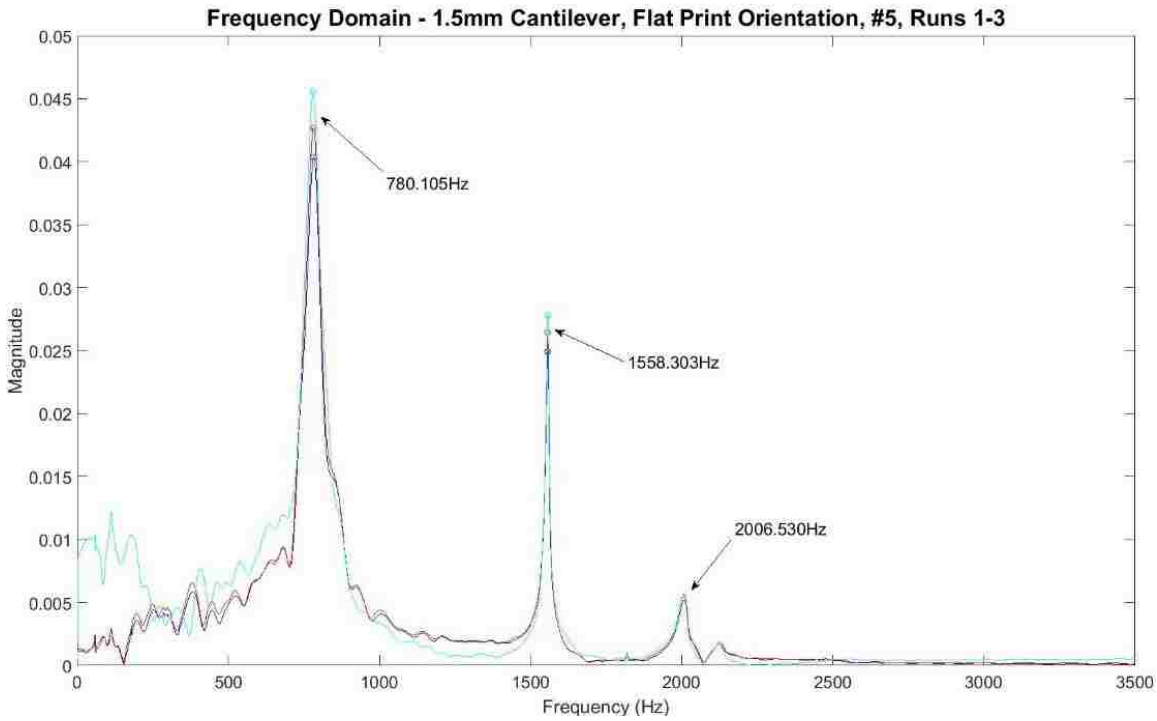
Frequency Domain - 1.5mm Cantilever, Flat Print Orientation, #5, Runs 1-3
780.105Hz
1558.303Hz
2006.530Hz
Magnitude
Frequency (Hz)
0.05
0.045
0.04
0.035
0.03
0.025
0.02
0.015
0.01
0.005
0
0
500
1000
1500
2000
2500
3000
3500

All flat 1.5mm coupons, all runs, overlaid –

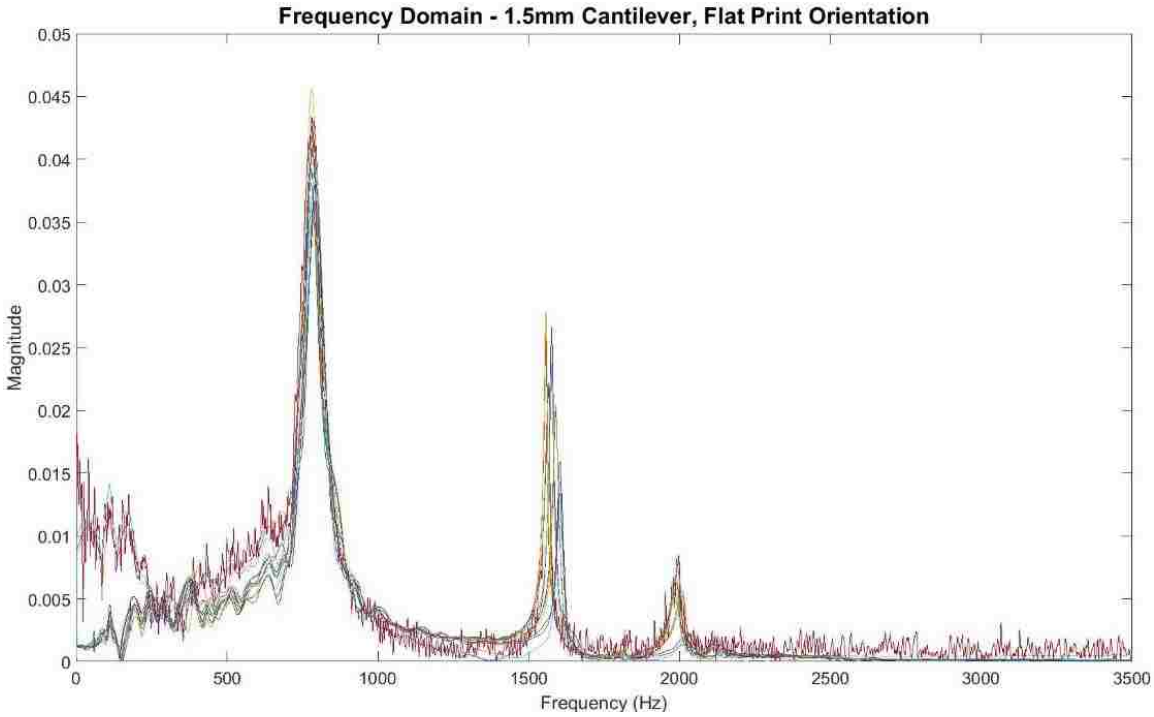

Angled Print Orientation – 2.0mm Cantilever Thickness –

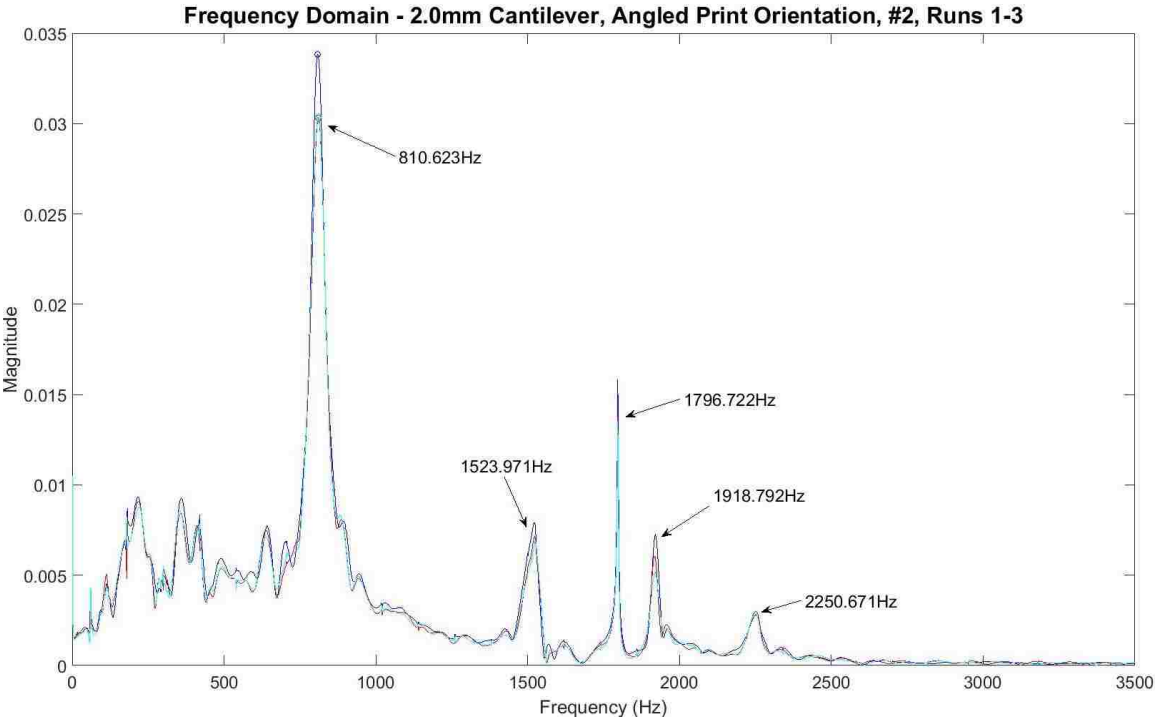

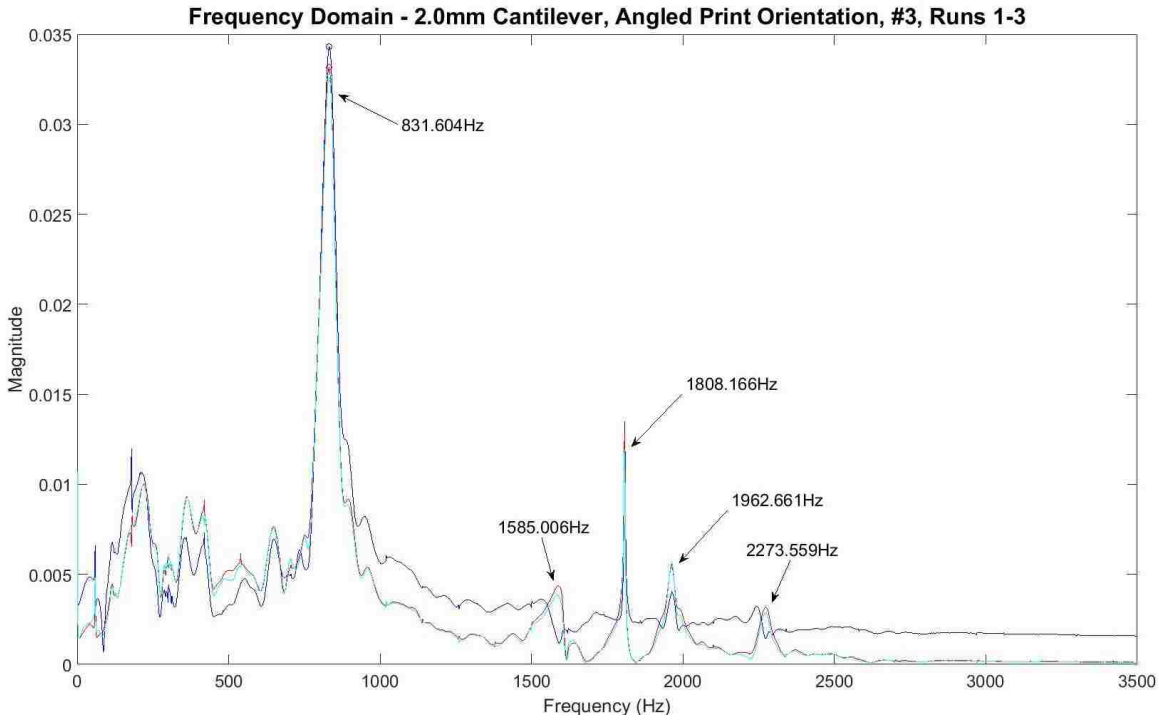
Frequency Domain - 2.0mm Cantilever, Angled Print Orientation, #3, Runs 1-3
Magnitude
Frequency (Hz)
831.604Hz
1808.166Hz
1962.661Hz
1585.006Hz
2273.559Hz
0.035
0.03
0.025
0.02
0.015
0.01
0.005
0
0
500
1000
1500
2000
2500
3000
3500

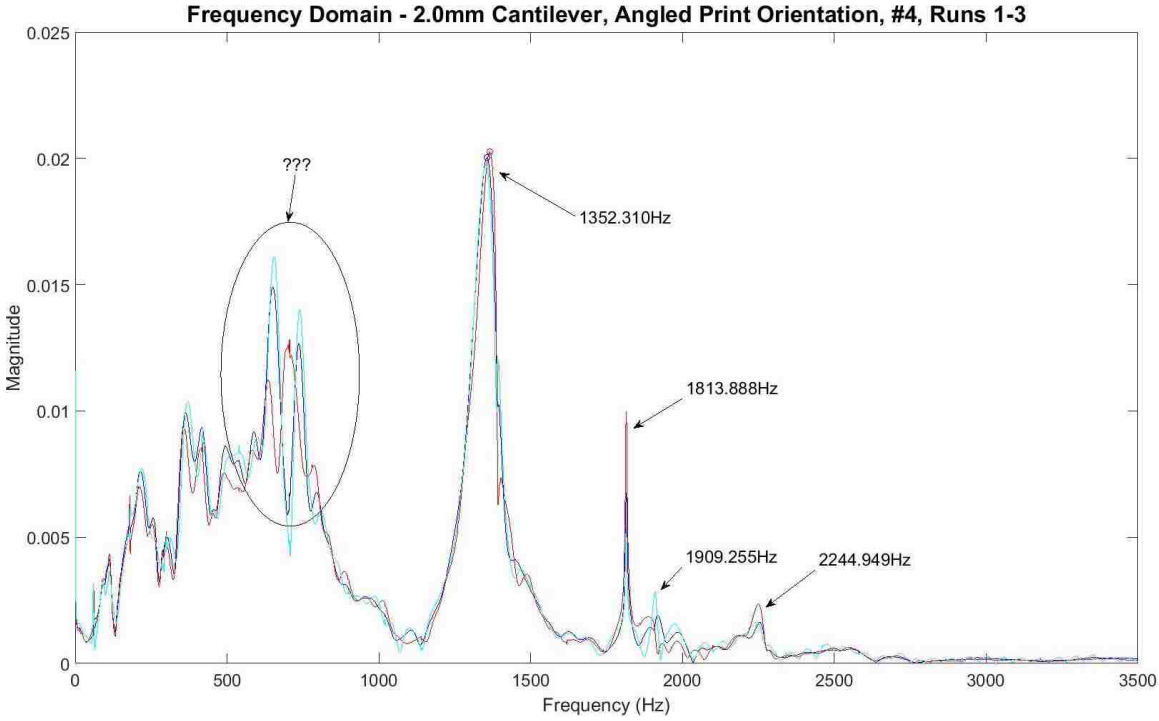
Frequency Domain - 2.0mm Cantilever, Angled Print Orientation, #4, Runs 1-3
Magnitude
Frequency (Hz)
???
1352.310Hz
1813.888Hz
1909.255Hz
2244.949Hz
0.025
0.02
0.015
0.01
0.005
0
0
500
1000
1500
2000
2500
3000
3500

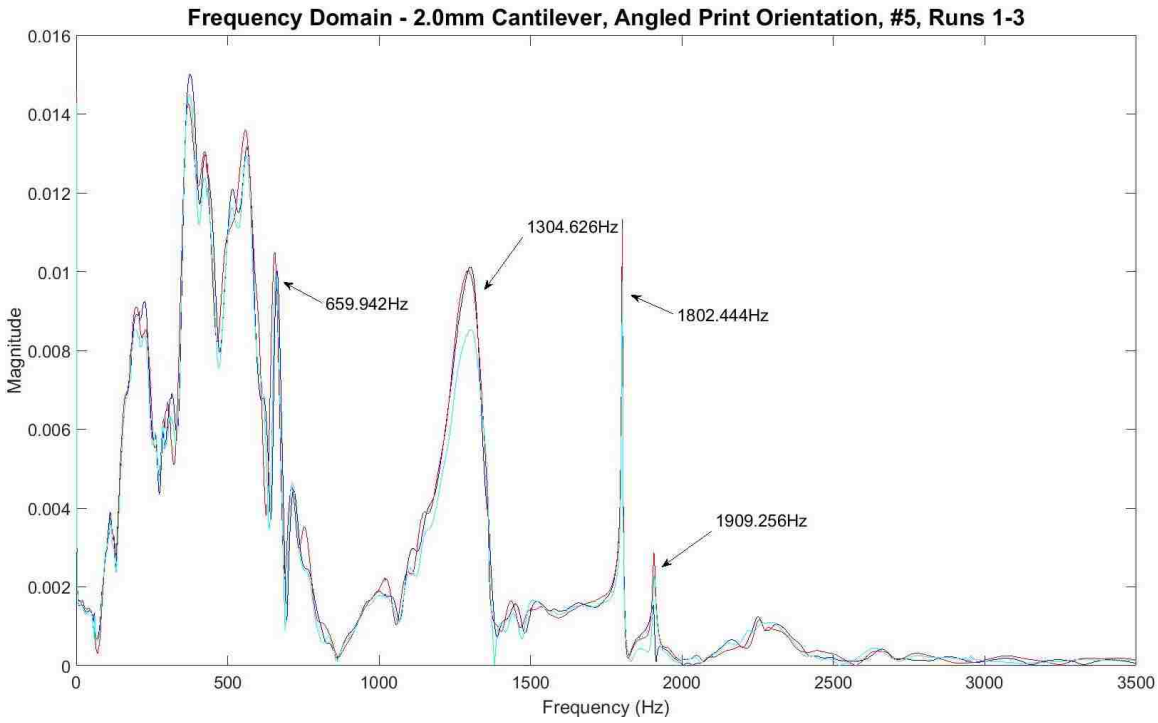

All angled 2.0mm coupons, all runs, overlaid –

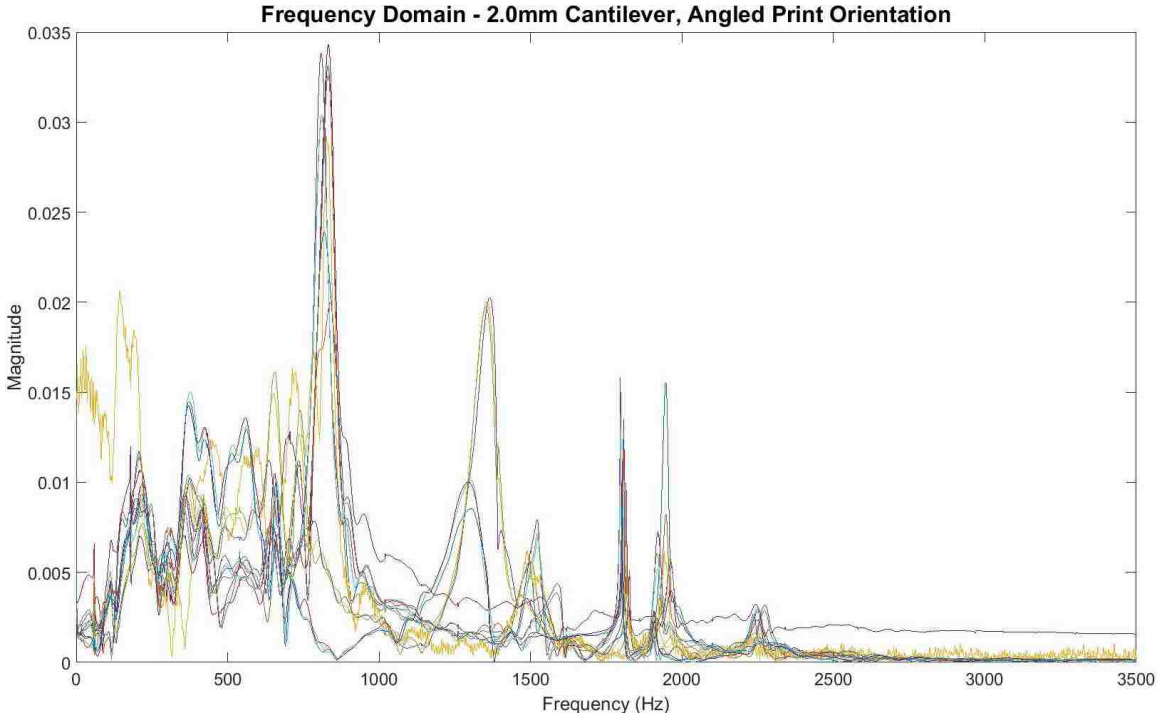

Flat Print Orientation – 2.0mm Cantilever Thickness –

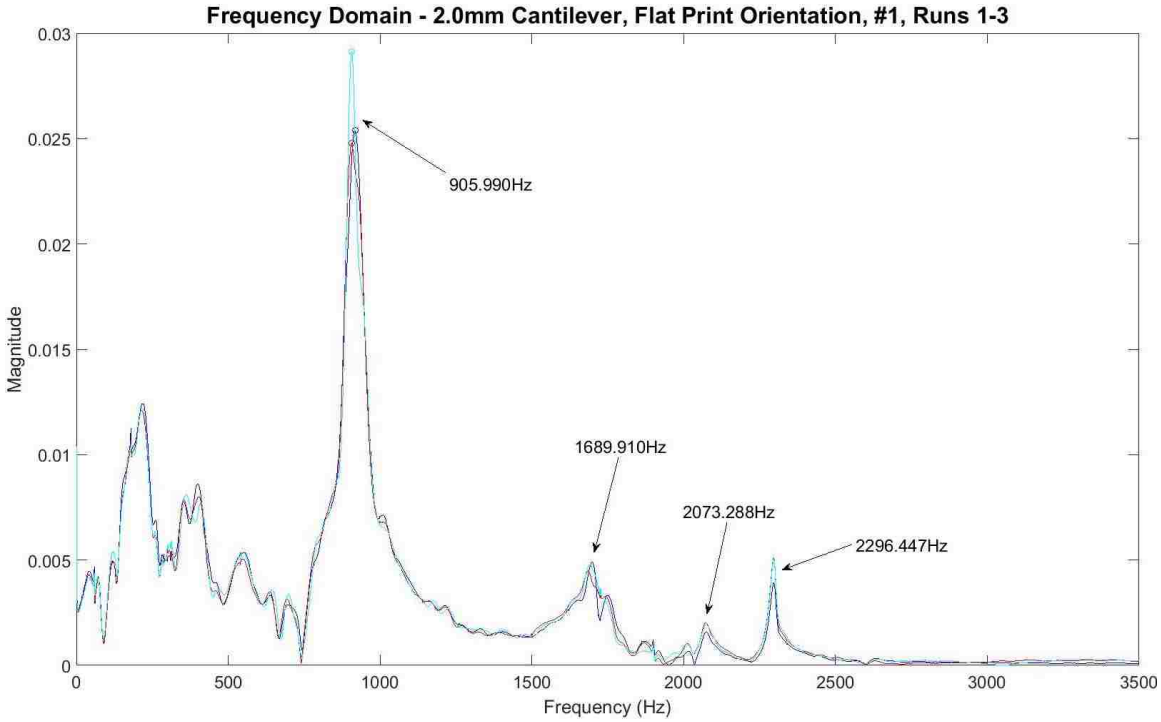

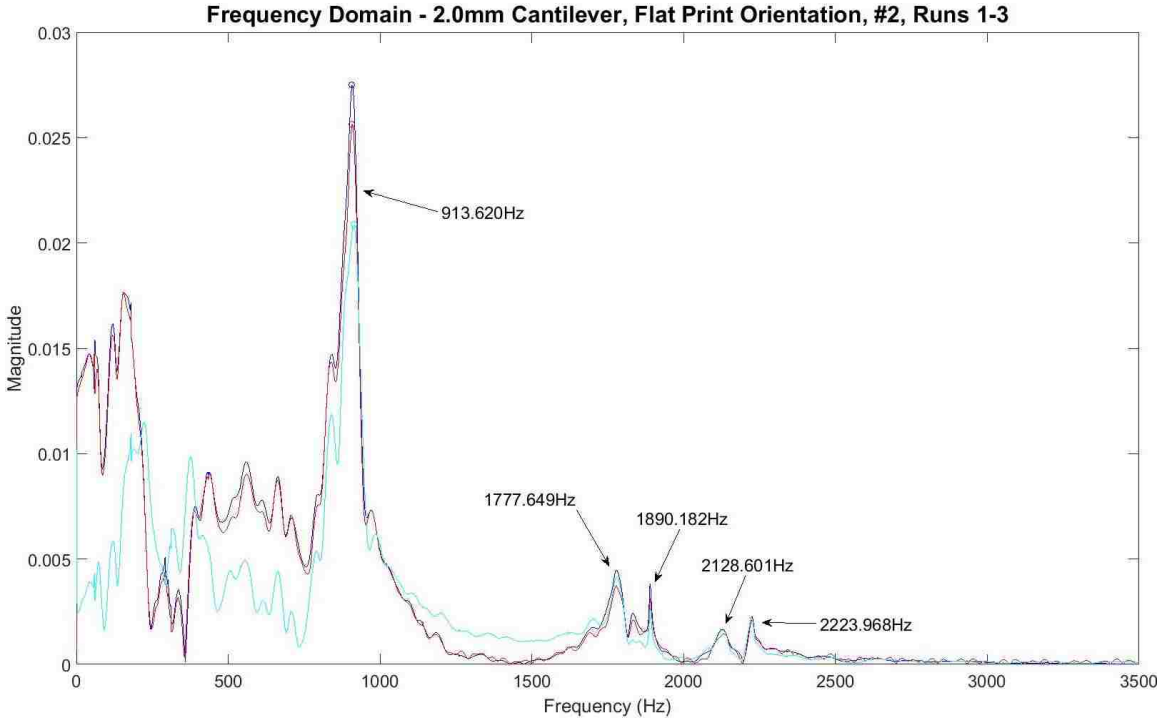

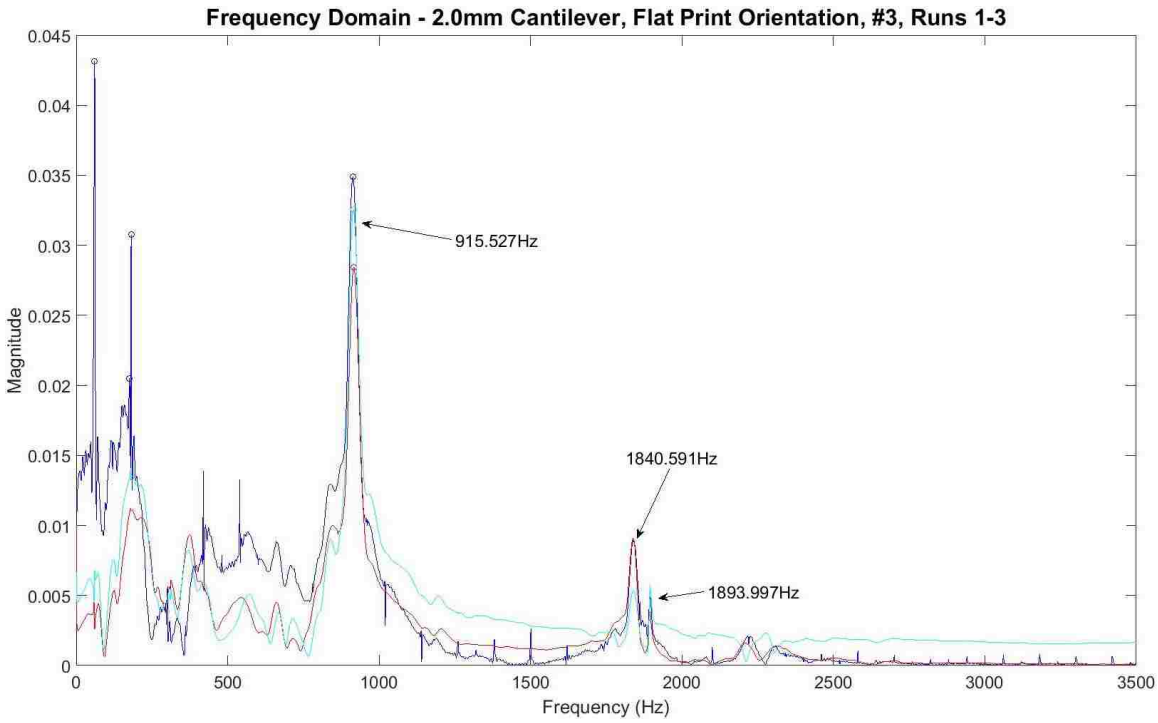
Frequency Domain - 2.0mm Cantilever, Flat Print Orientation, #3, Runs 1-3
Magnitude
Frequency (Hz)
915.527Hz
1840.591Hz
1893.997Hz
0.045
0.04
0.035
0.03
0.025
0.02
0.015
0.01
0.005
0
0
500
1000
1500
2000
2500
3000
3500

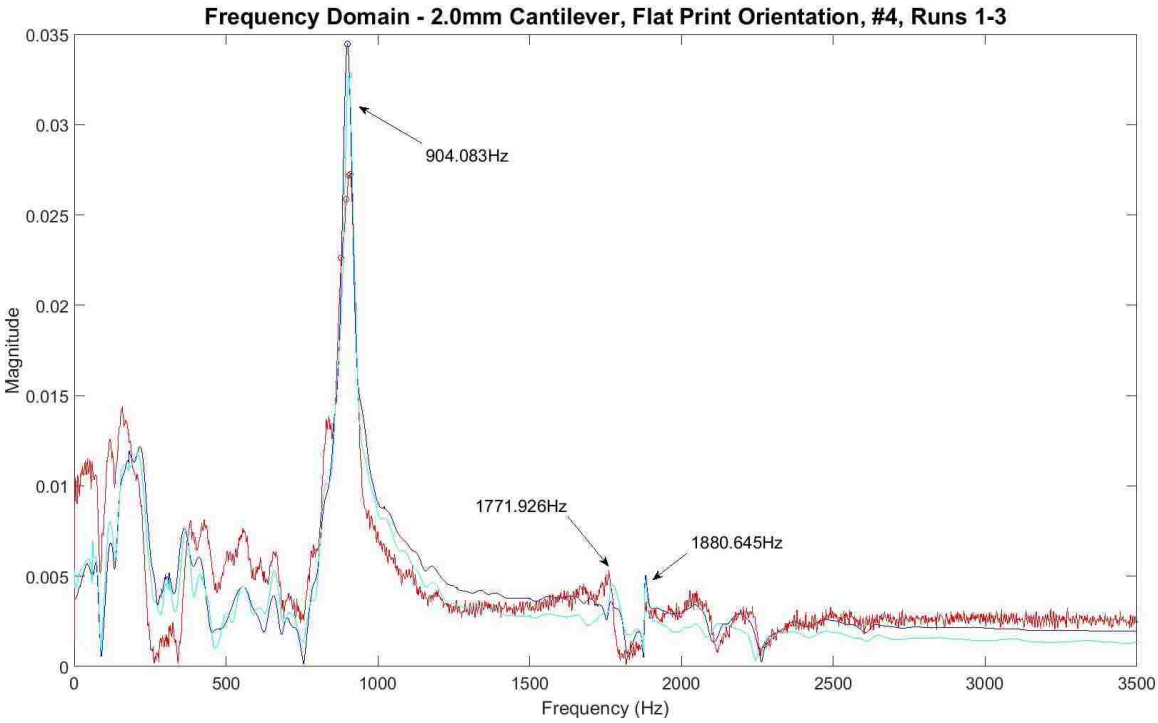
Frequency Domain - 2.0mm Cantilever, Flat Print Orientation, #4, Runs 1-3
Magnitude
Frequency (Hz)
904.083Hz
1771.926Hz
1880.645Hz
0.035
0.03
0.025
0.02
0.015
0.01
0.005
0
0
500
1000
1500
2000
2500
3000
3500

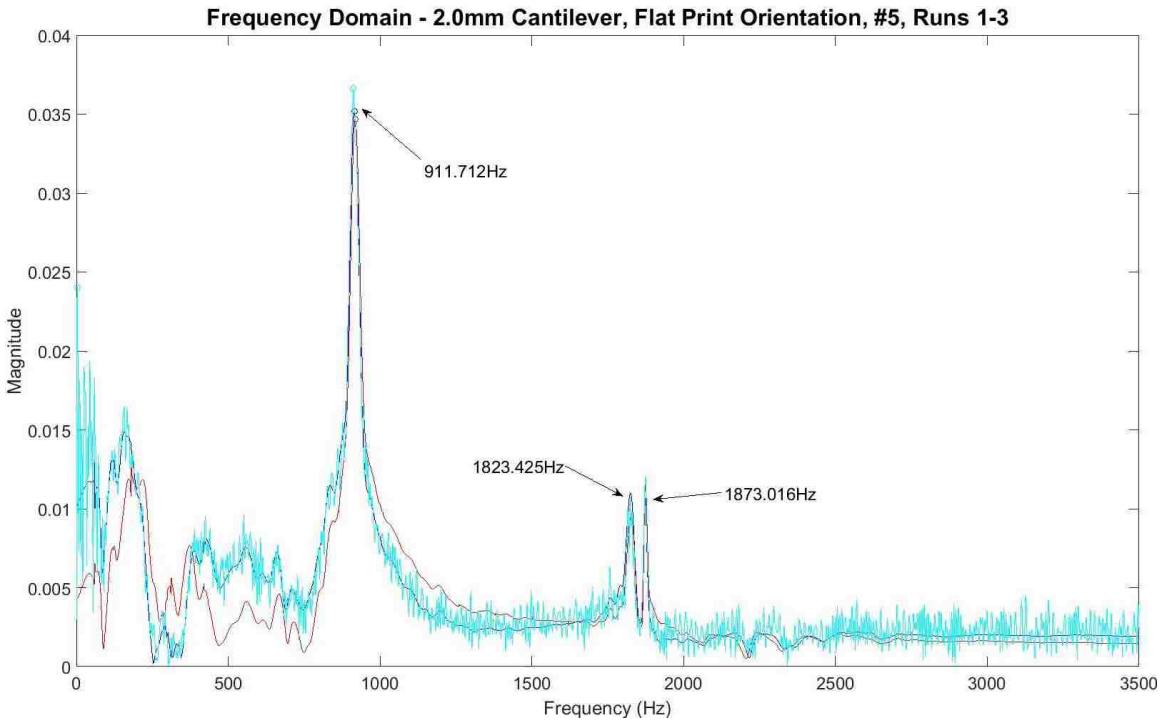

All flat 2.0mm coupons, all runs, overlaid –

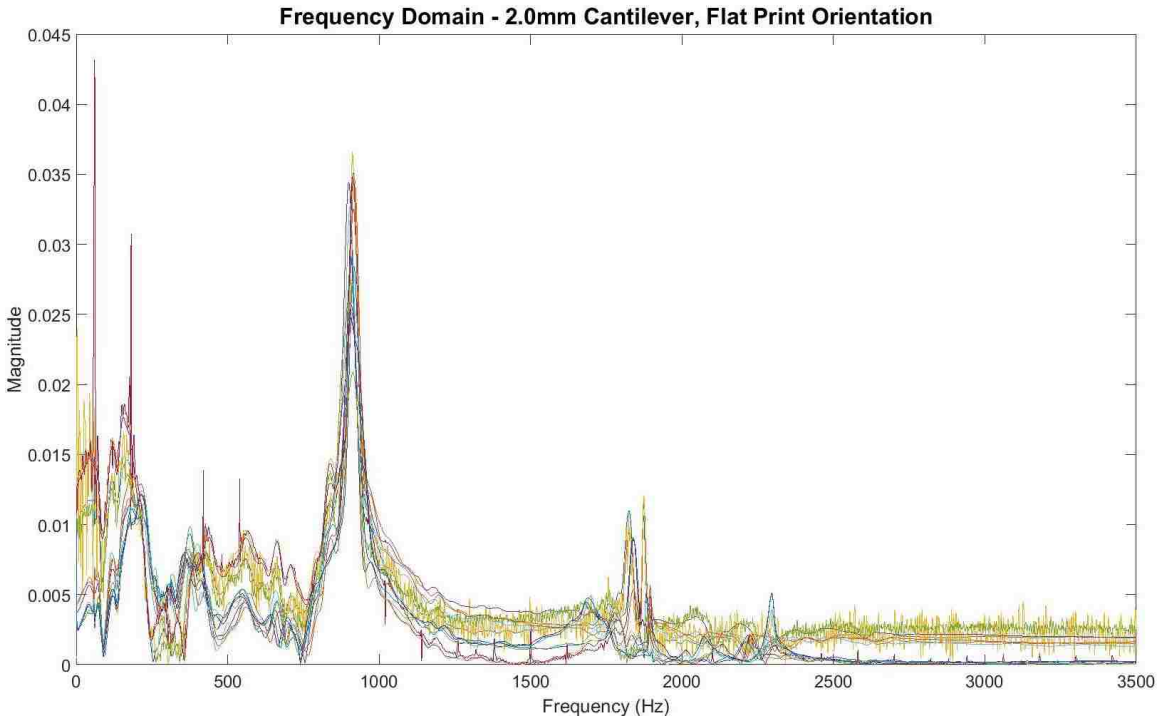

Angled Print Orientation – 2.5mm Cantilever Thickness –

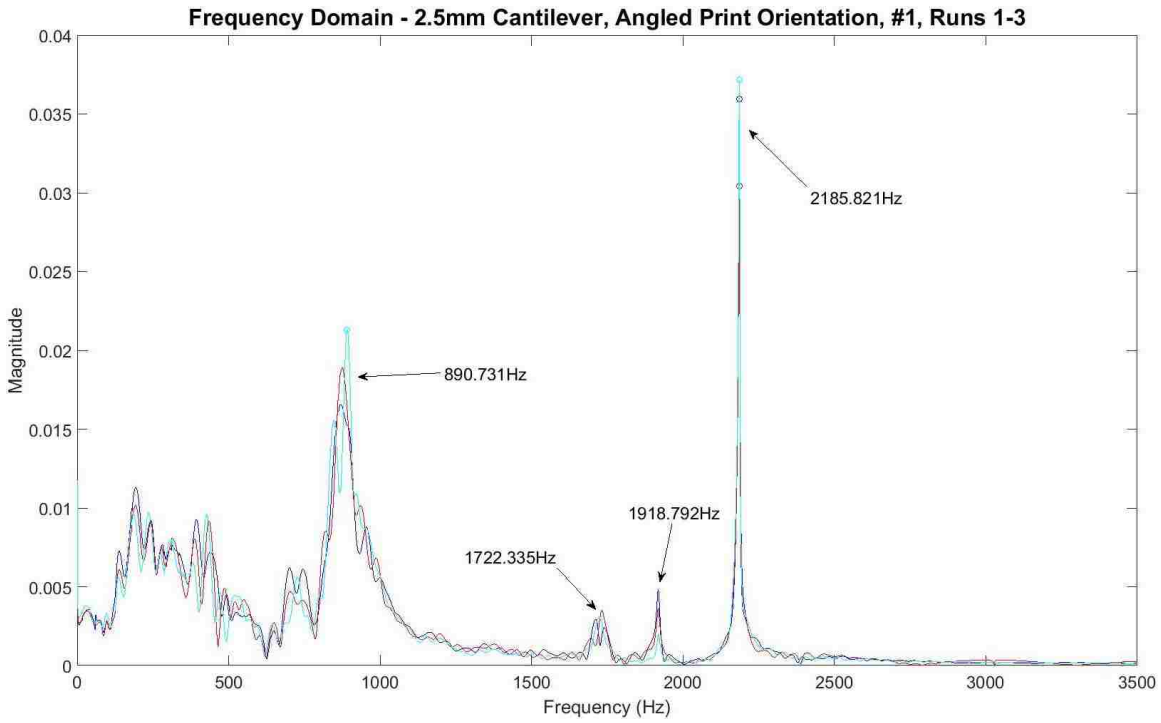

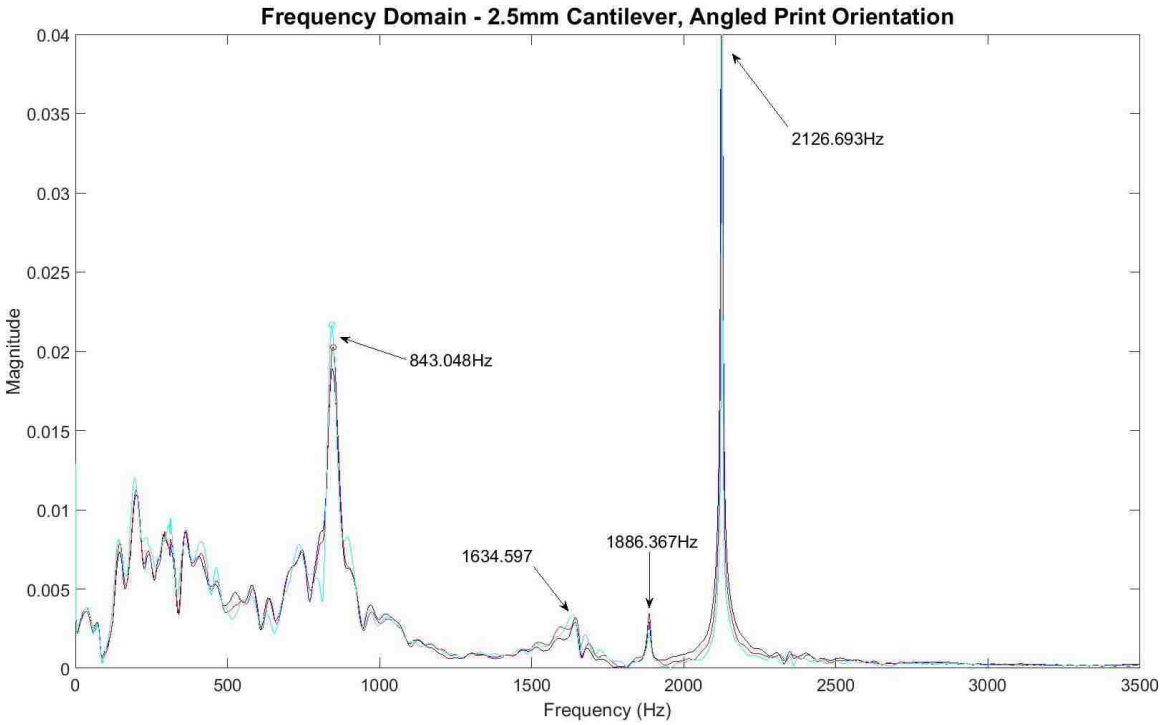

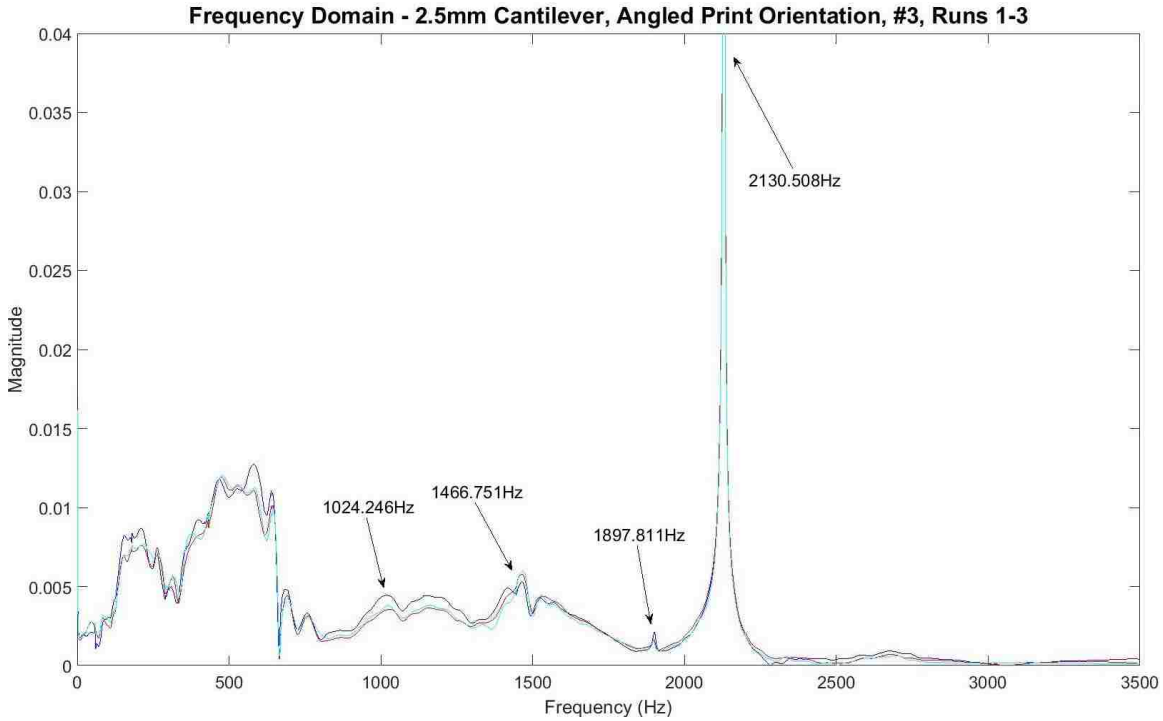
Frequency Domain - 2.5mm Cantilever, Angled Print Orientation, #3, Runs 1-3
Magnitude
Frequency (Hz)
2130.508Hz
1466.751Hz
1024.246Hz
1897.811Hz

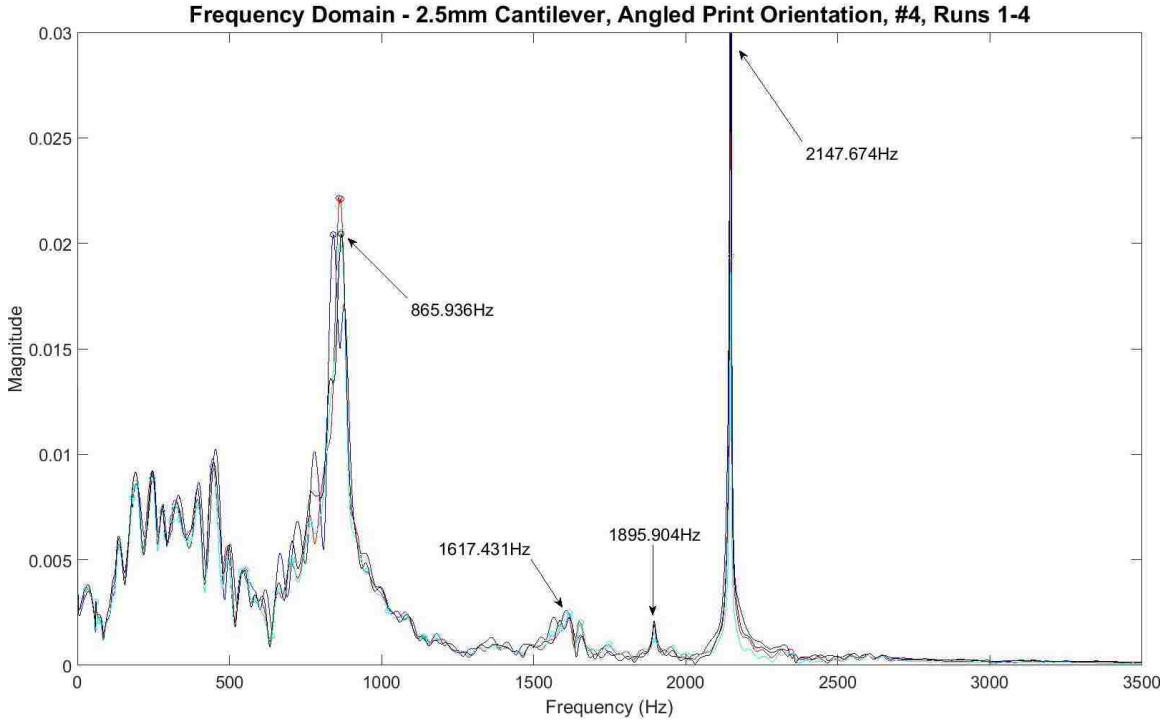
Frequency Domain - 2.5mm Cantilever, Angled Print Orientation, #4, Runs 1-4
Magnitude
Frequency (Hz)
2147.674Hz
865.936Hz
1617.431Hz
1895.904Hz

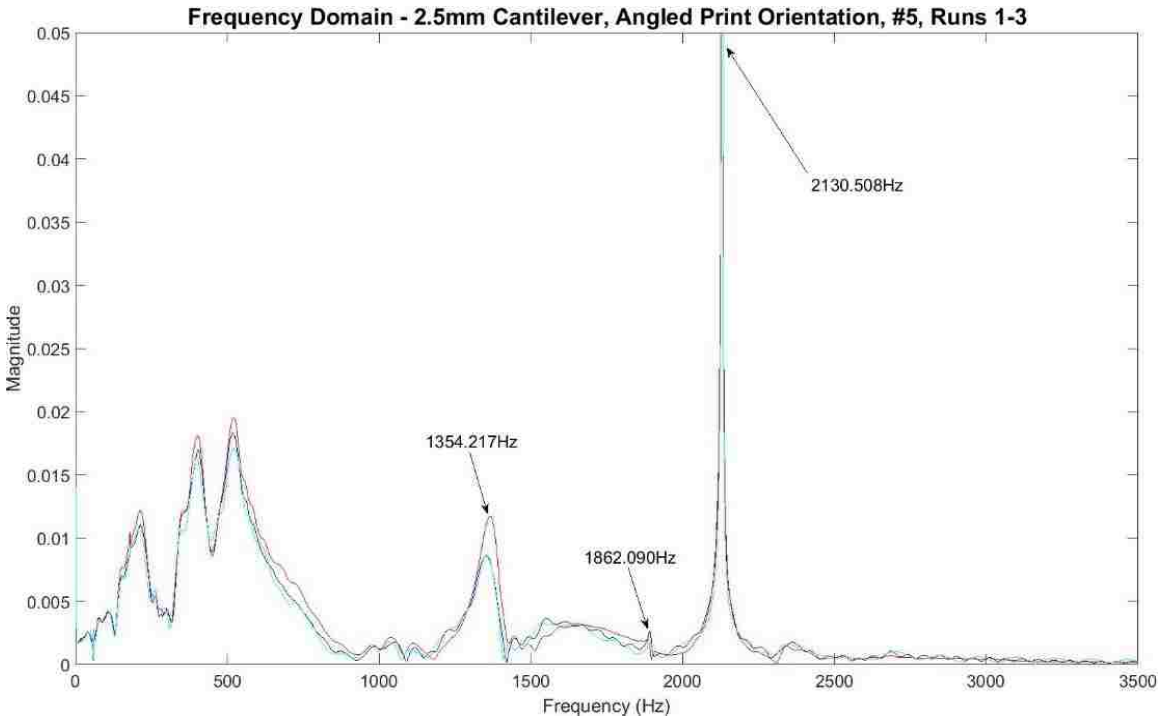

All angled 2.5mm coupons, all runs, overlaid –

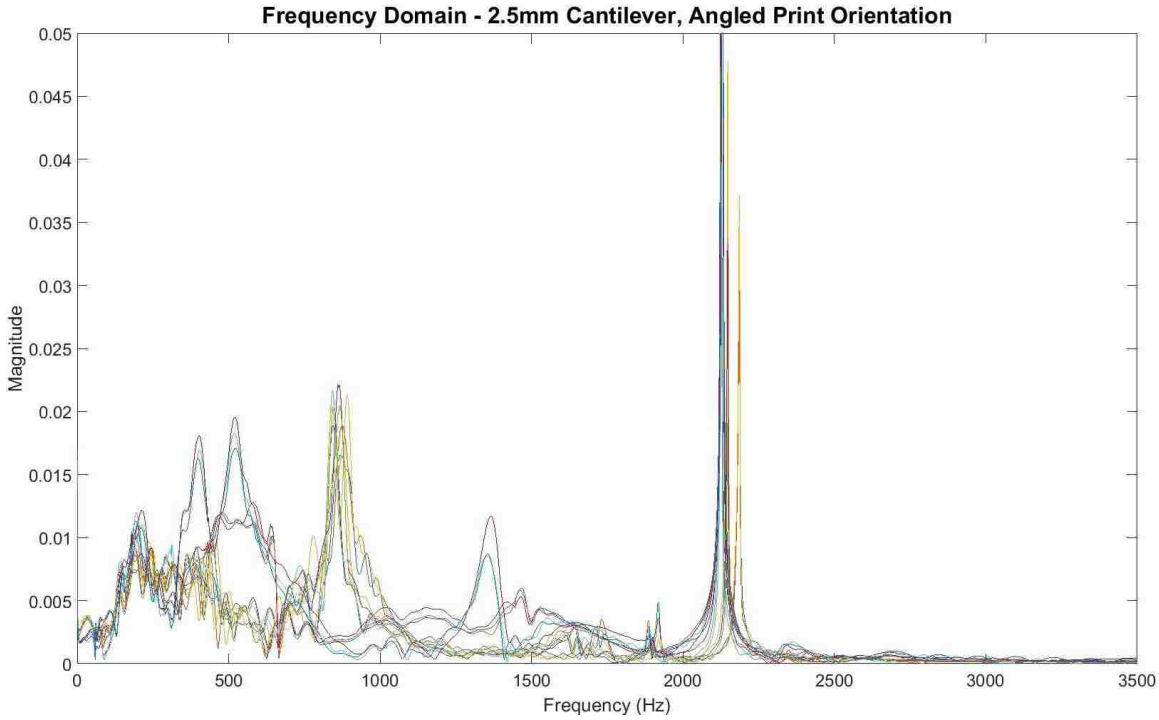

Flat Print Orientation – 2.5mm Cantilever Thickness –

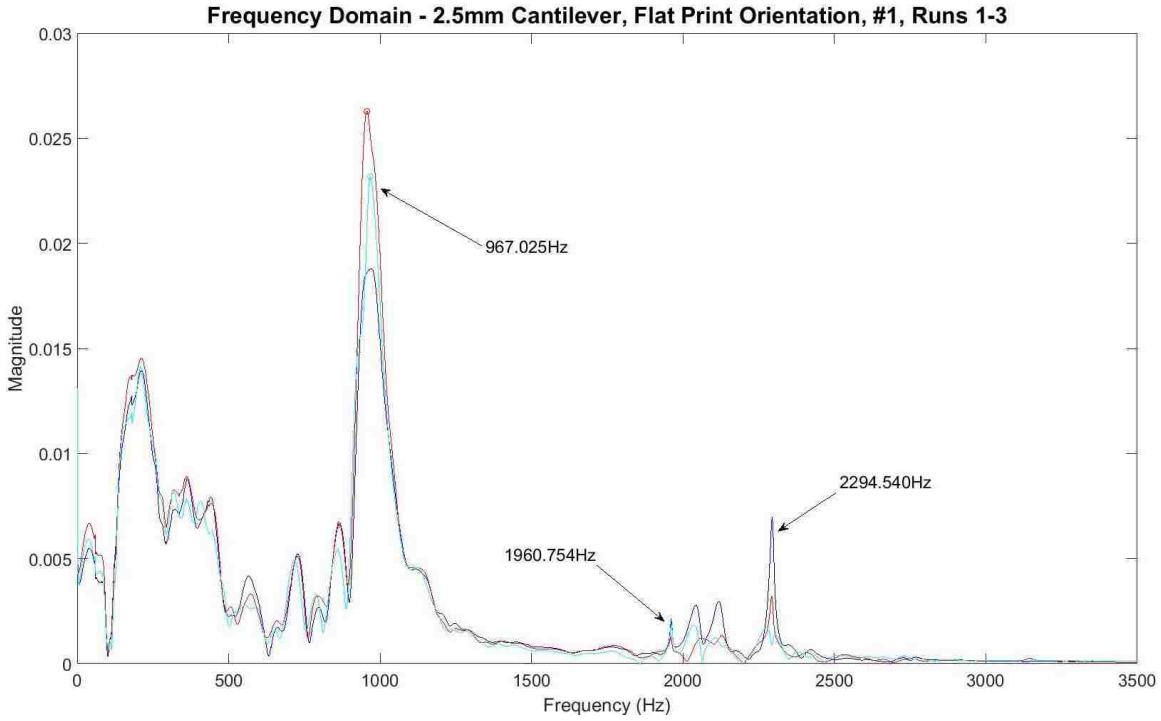

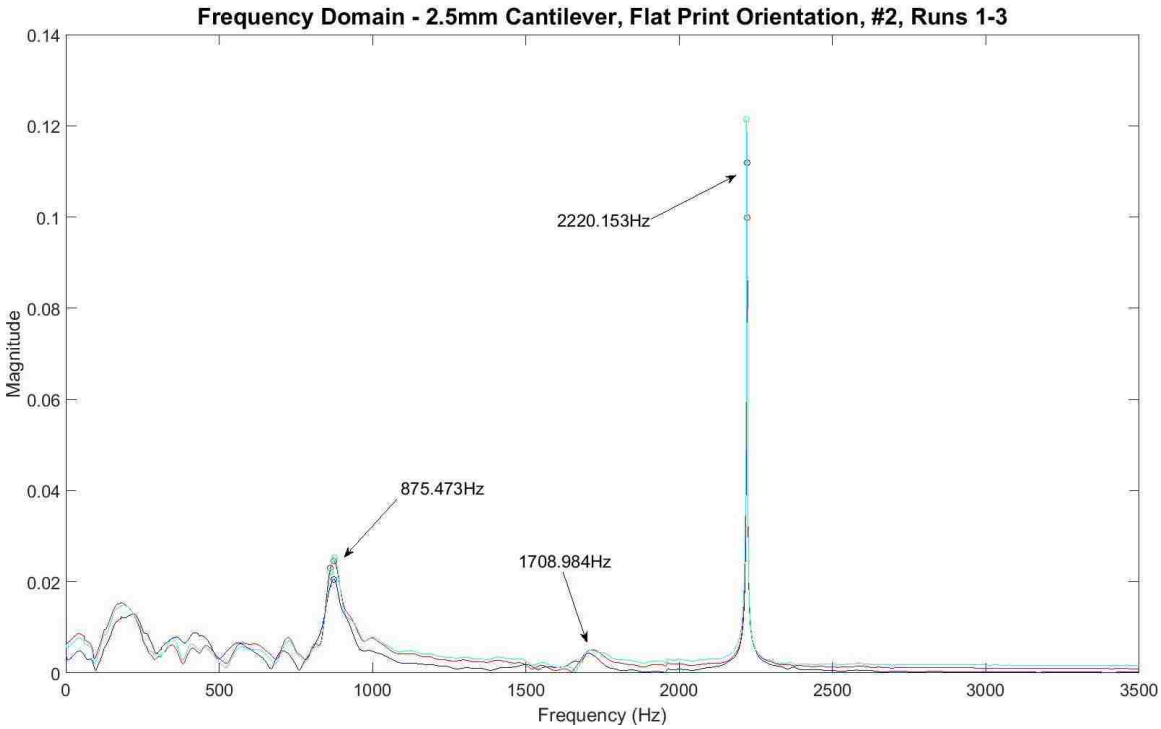

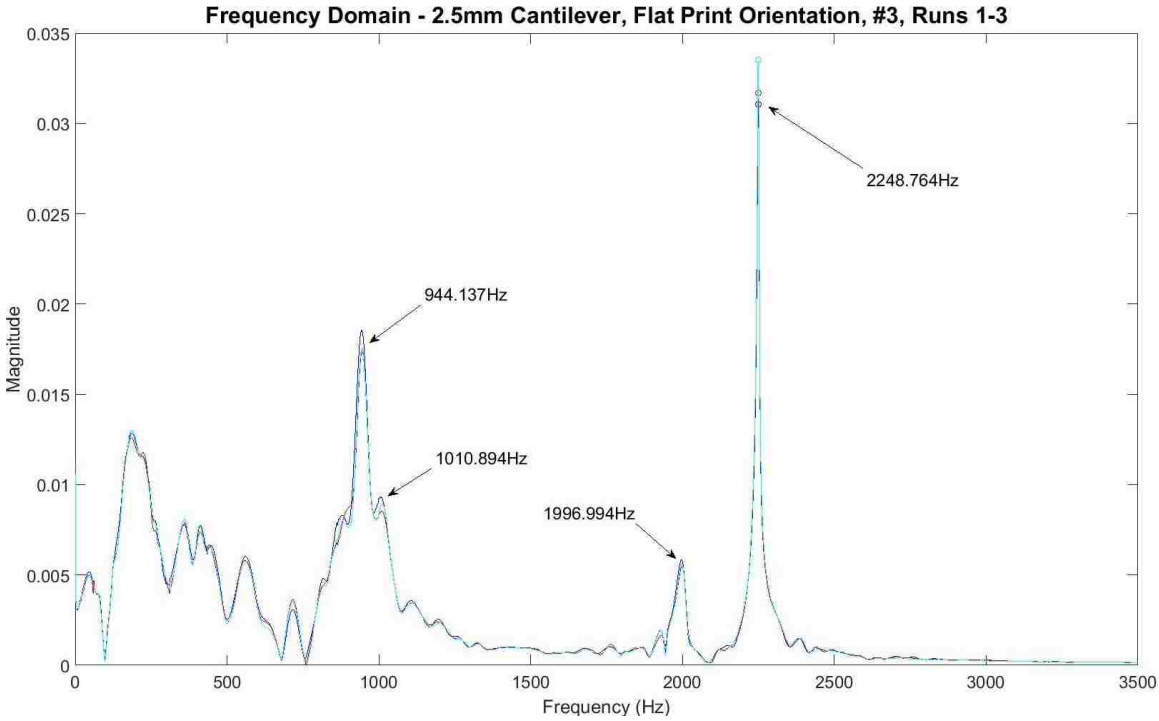
Frequency Domain - 2.5mm Cantilever, Flat Print Orientation, #3, Runs 1-3
Magnitude
Frequency (Hz)
2248.764Hz
944.137Hz
1010.894Hz
1996.994Hz
0.035
0.03
0.025
0.02
0.015
0.01
0.005
0
0
500
1000
1500
2000
2500
3000
3500

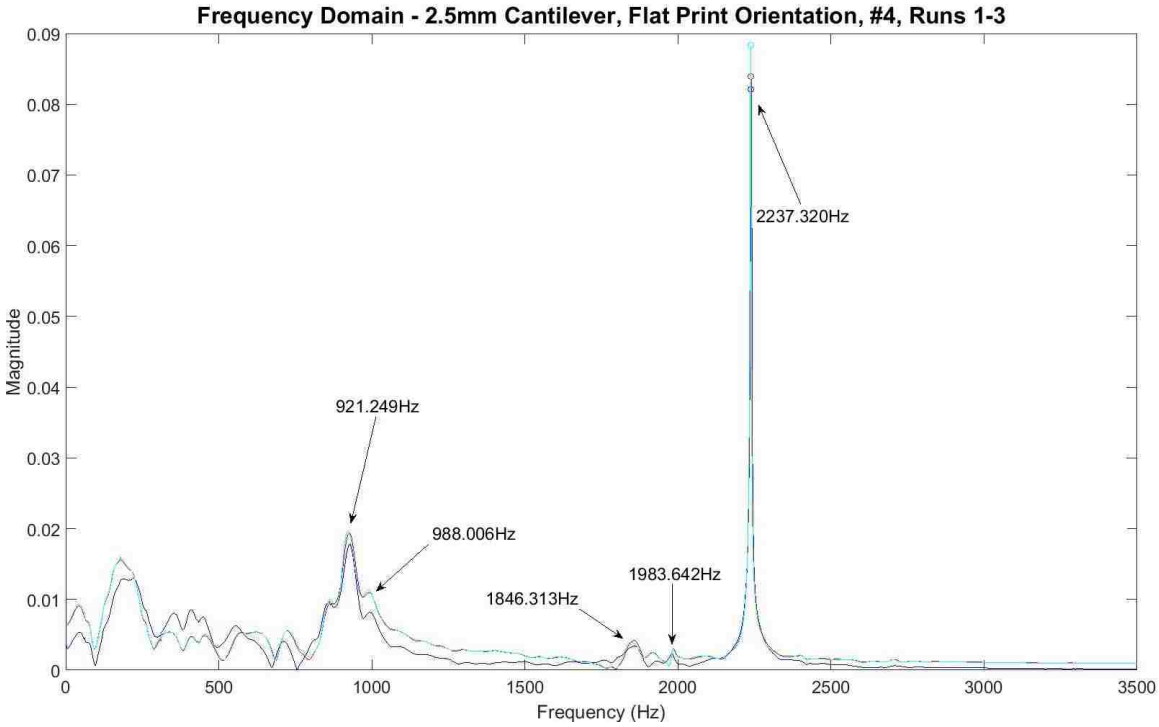
Frequency Domain - 2.5mm Cantilever, Flat Print Orientation, #4, Runs 1-3
Magnitude
Frequency (Hz)
2237.320Hz
921.249Hz
988.006Hz
1983.642Hz
1846.313Hz
0.09
0.08
0.07
0.06
0.05
0.04
0.03
0.02
0.01
0
0
500
1000
1500
2000
2500
3000
3500

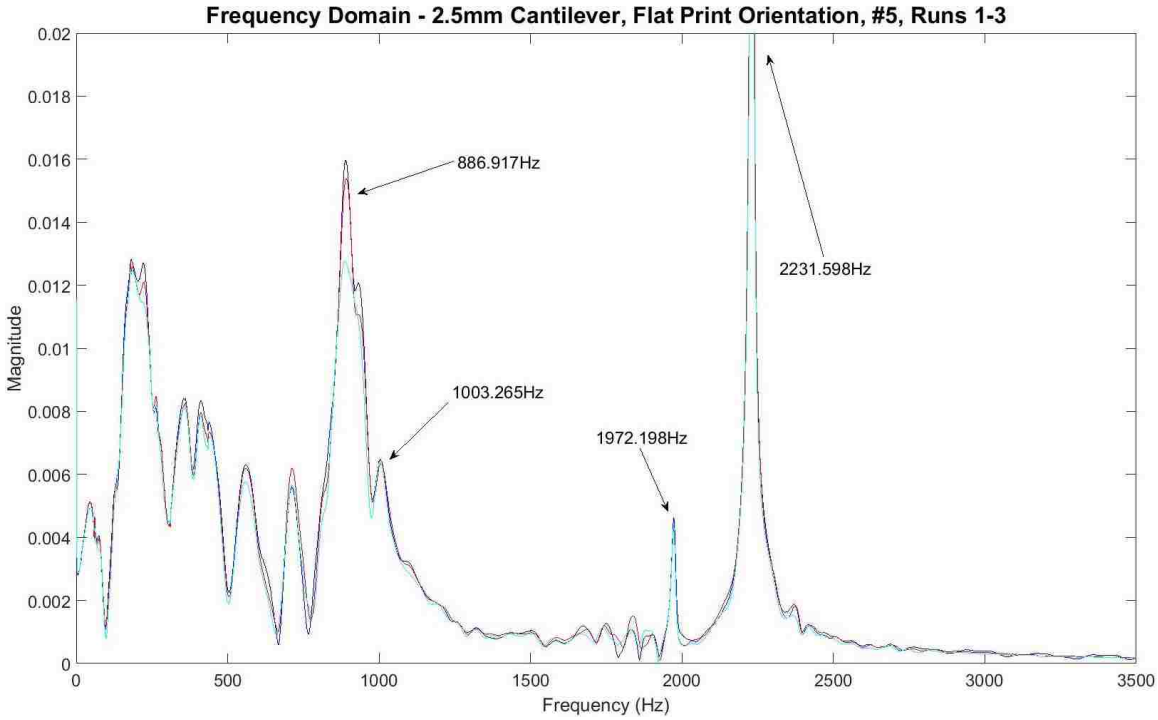

All flat 2.5mm coupons, all runs, overlaid –

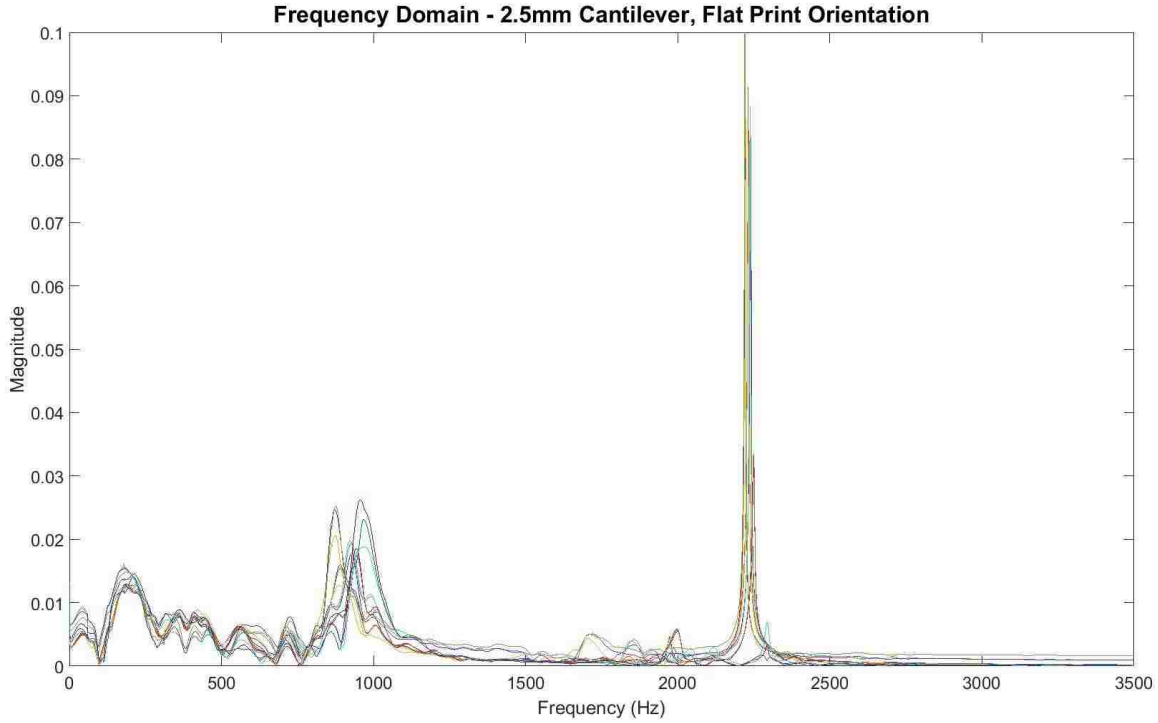

A.5 Young's Modulus vs. Resonant Frequency Plots

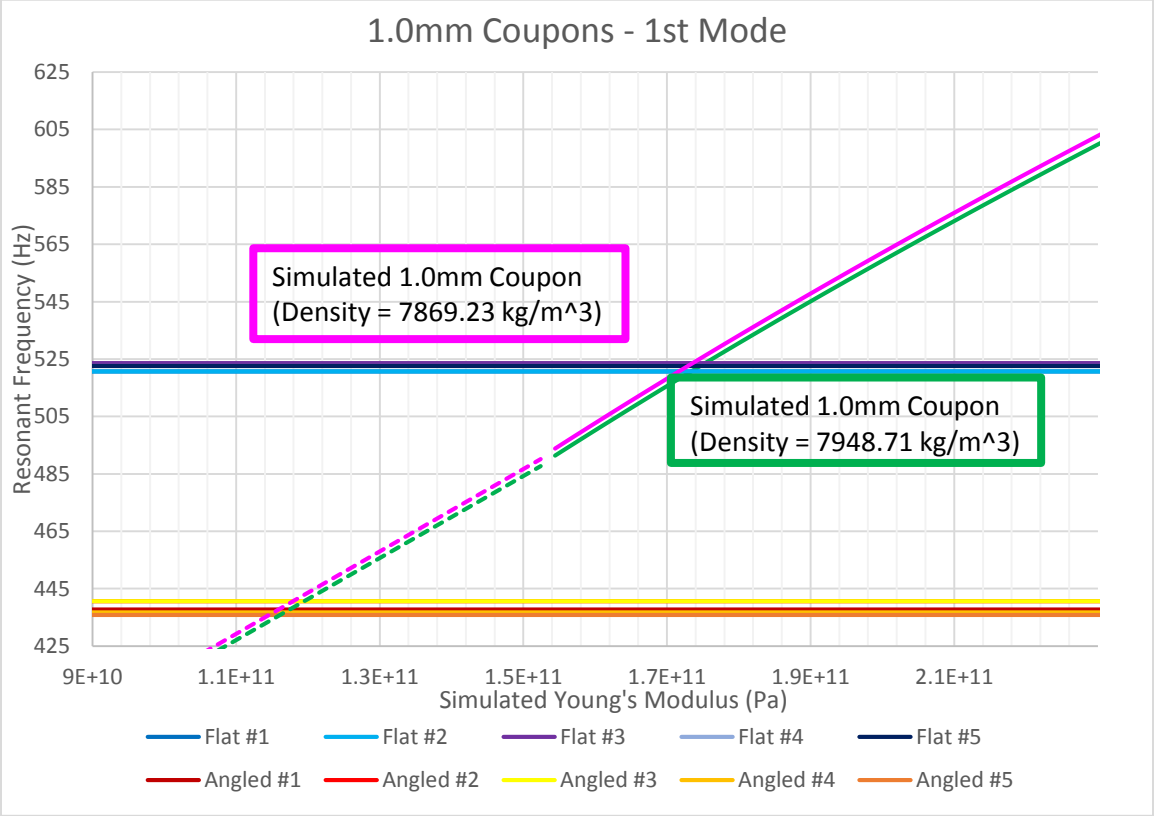

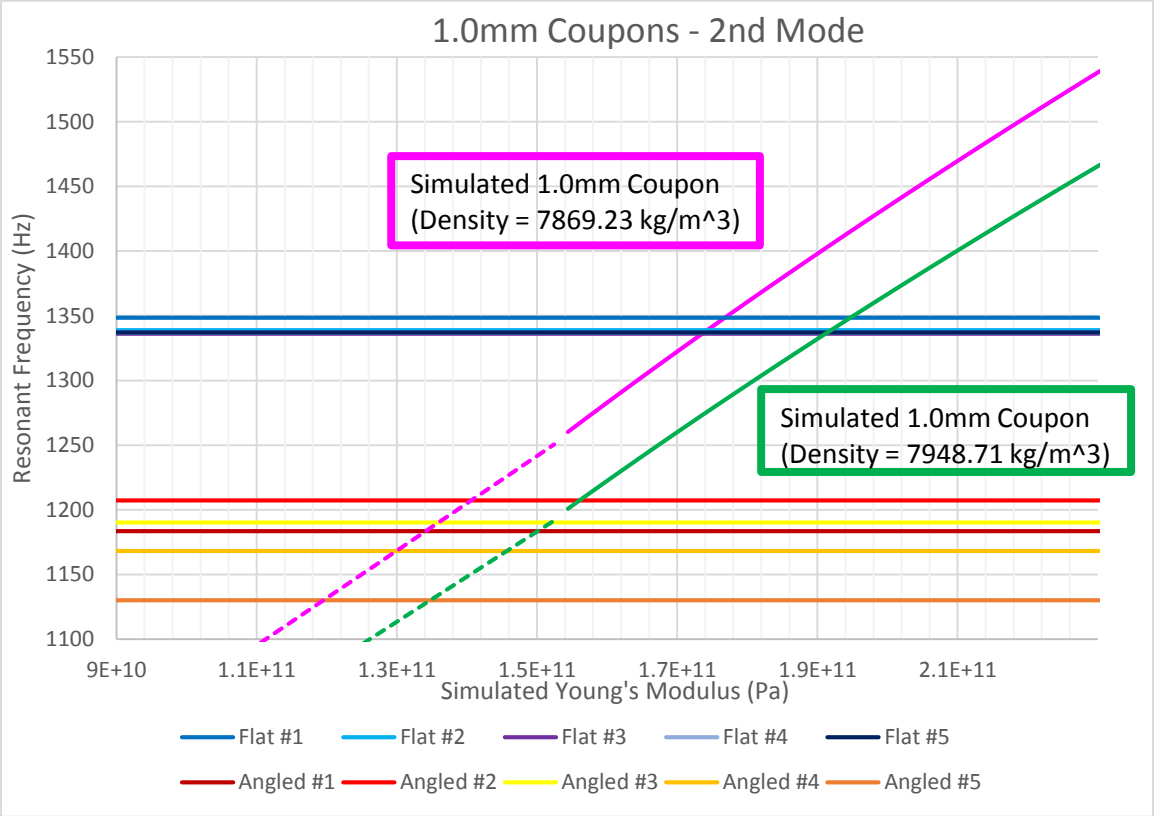

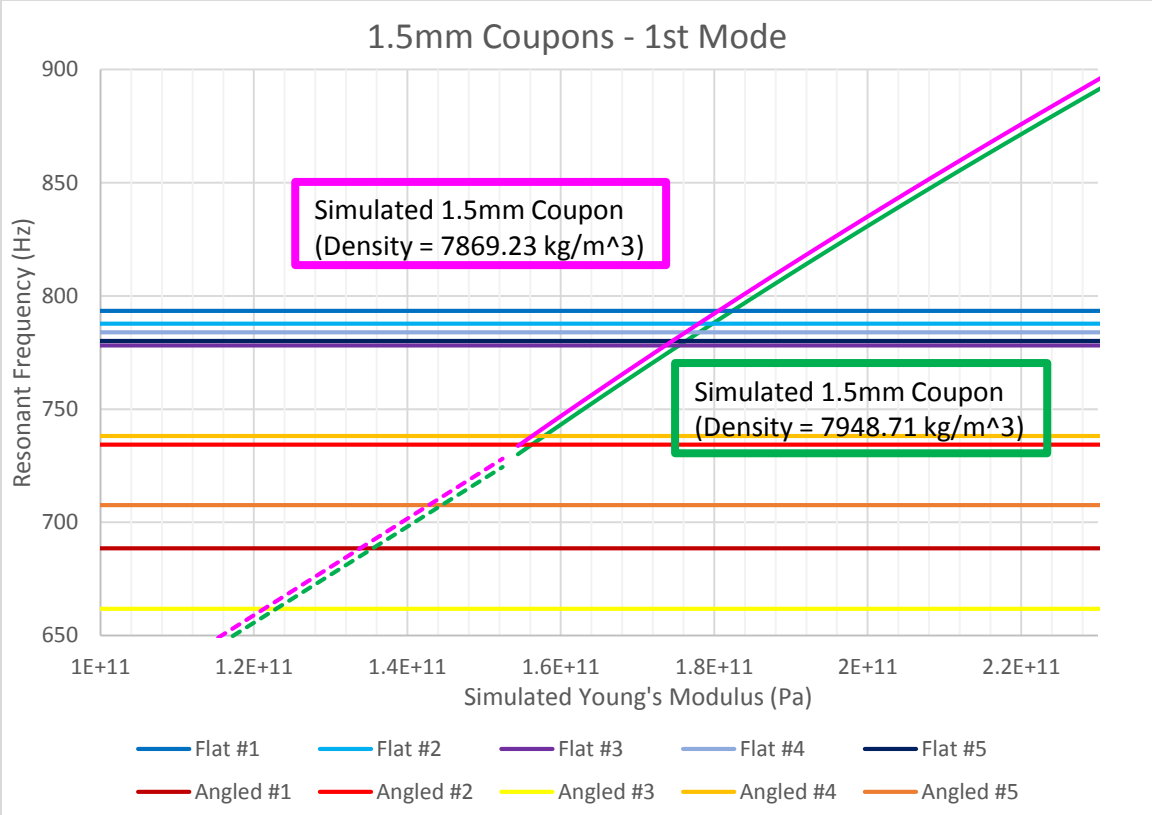
1.5mm Coupons - 1st Mode
Resonant Frequency (Hz)
900
850
800
750
700
650
Simulated 1.5mm Coupon
(Density = 7869.23 kg/m^3)
Simulated 1.5mm Coupon
(Density = 7948.71 kg/m^3)
1E+11
1.2E+11
1.4E+11
1.6E+11
1.8E+11
2E+11
2.2E+11
Simulated Young's Modulus (Pa)
Flat #1
Flat #2
Flat #3
Flat #4
Flat #5
Angled #1
Angled #2
Angled #3
Angled #4
Angled #5

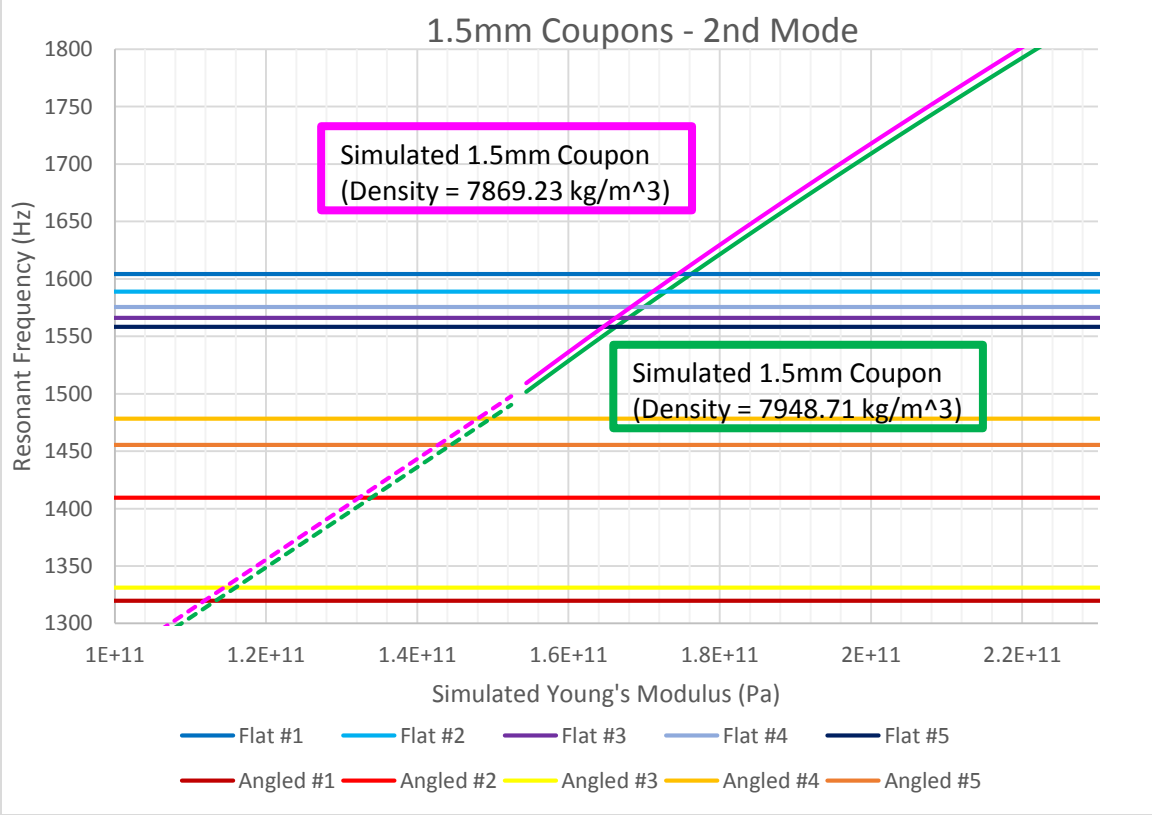
1.5mm Coupons - 2nd Mode
Resonant Frequency (Hz)
1800
1750
1700
1650
1600
1550
1500
1450
1400
1350
1300
Simulated 1.5mm Coupon
(Density = 7869.23 kg/m^3)
Simulated 1.5mm Coupon
(Density = 7948.71 kg/m^3)
1E+11
1.2E+11
1.4E+11
1.6E+11
1.8E+11
2E+11
2.2E+11
Simulated Young's Modulus (Pa)
Flat #1
Flat #2
Flat #3
Flat #4
Flat #5
Angled #1
Angled #2
Angled #3
Angled #4
Angled #5

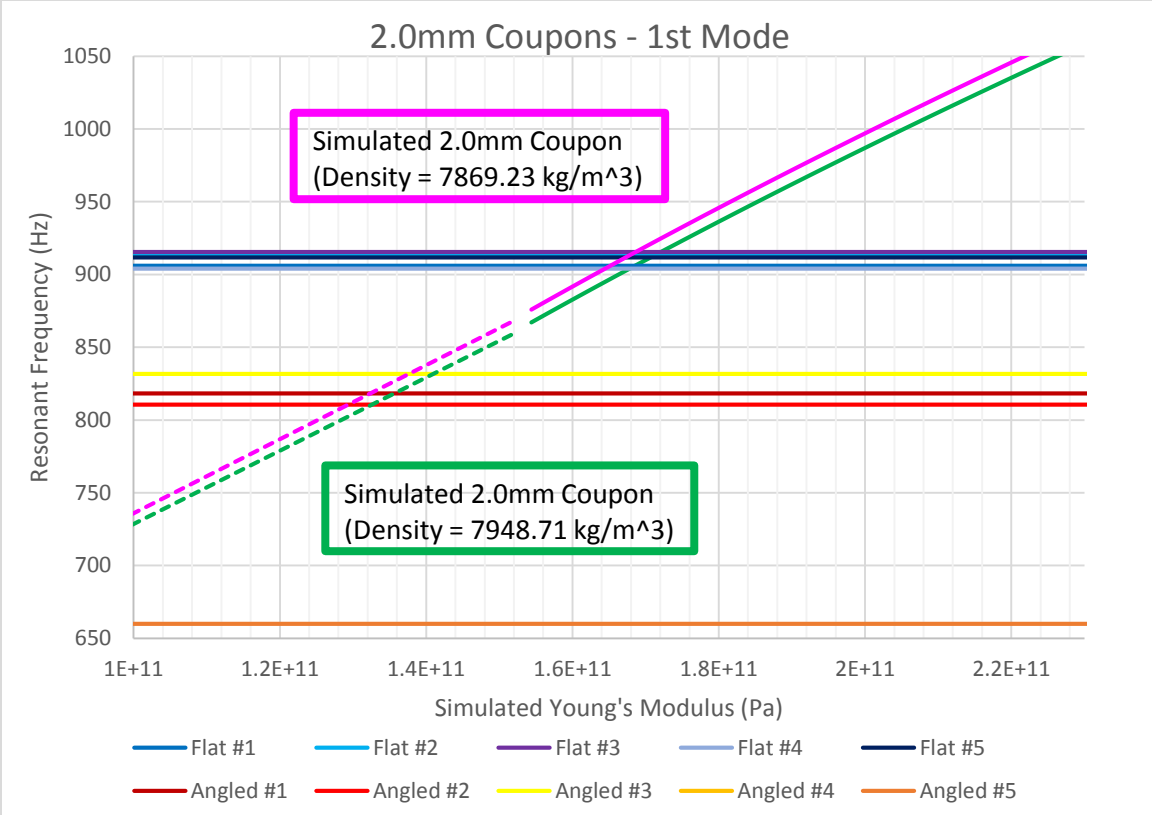
2.0mm Coupons - 1st Mode
Resonant Frequency (Hz)
1050
1000
950
900
850
800
750
700
650
Simulated 2.0mm Coupon
(Density = 7869.23 kg/m^3)
Simulated 2.0mm Coupon
(Density = 7948.71 kg/m^3)
1E+11
1.2E+11
1.4E+11
1.6E+11
1.8E+11
2E+11
2.2E+11
Simulated Young's Modulus (Pa)
Flat #1
Flat #2
Flat #3
Flat #4
Flat #5
Angled #1
Angled #2
Angled #3
Angled #4
Angled #5

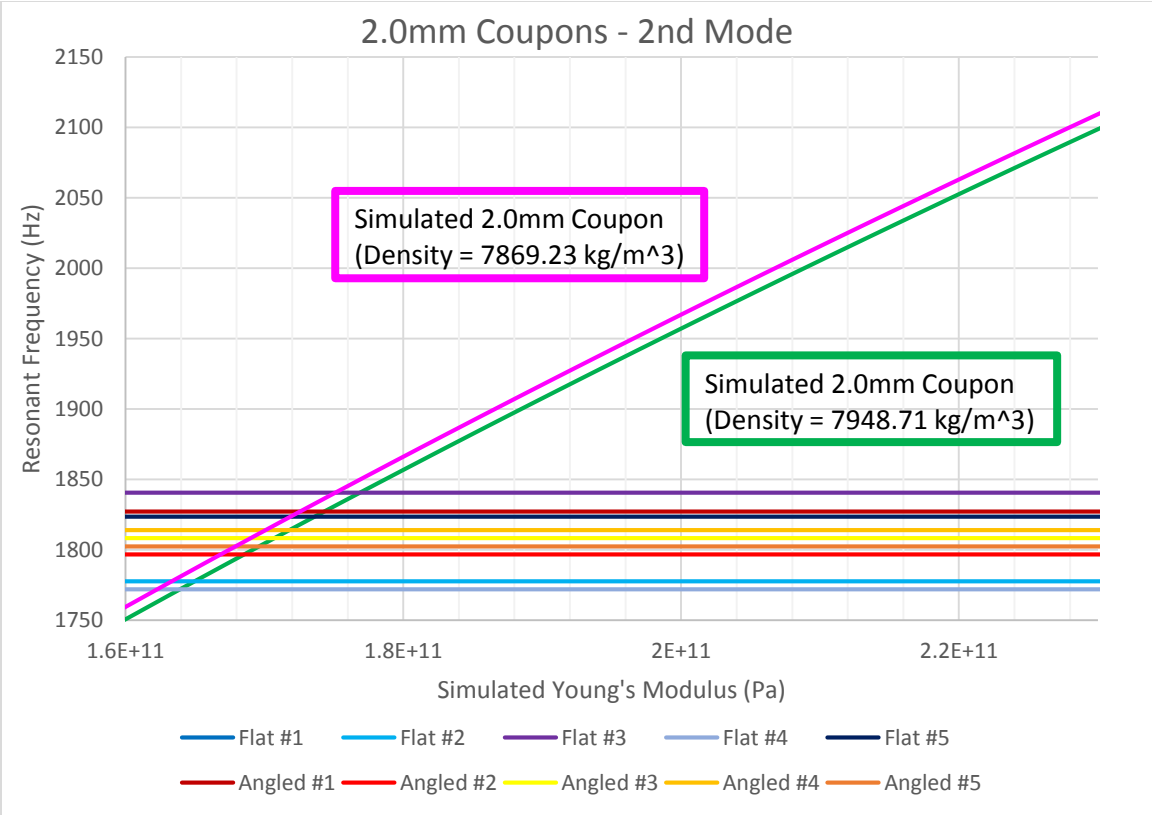
2.0mm Coupons - 2nd Mode
Resonant Frequency (Hz)
2150
2100
2050
2000
1950
1900
1850
1800
1750
Simulated 2.0mm Coupon
(Density = 7869.23 kg/m^3)
Simulated 2.0mm Coupon
(Density = 7948.71 kg/m^3)
1.6E+11
1.8E+11
2E+11
2.2E+11
Simulated Young's Modulus (Pa)
Flat #1
Flat #2
Flat #3
Flat #4
Flat #5
Angled #1
Angled #2
Angled #3
Angled #4
Angled #5

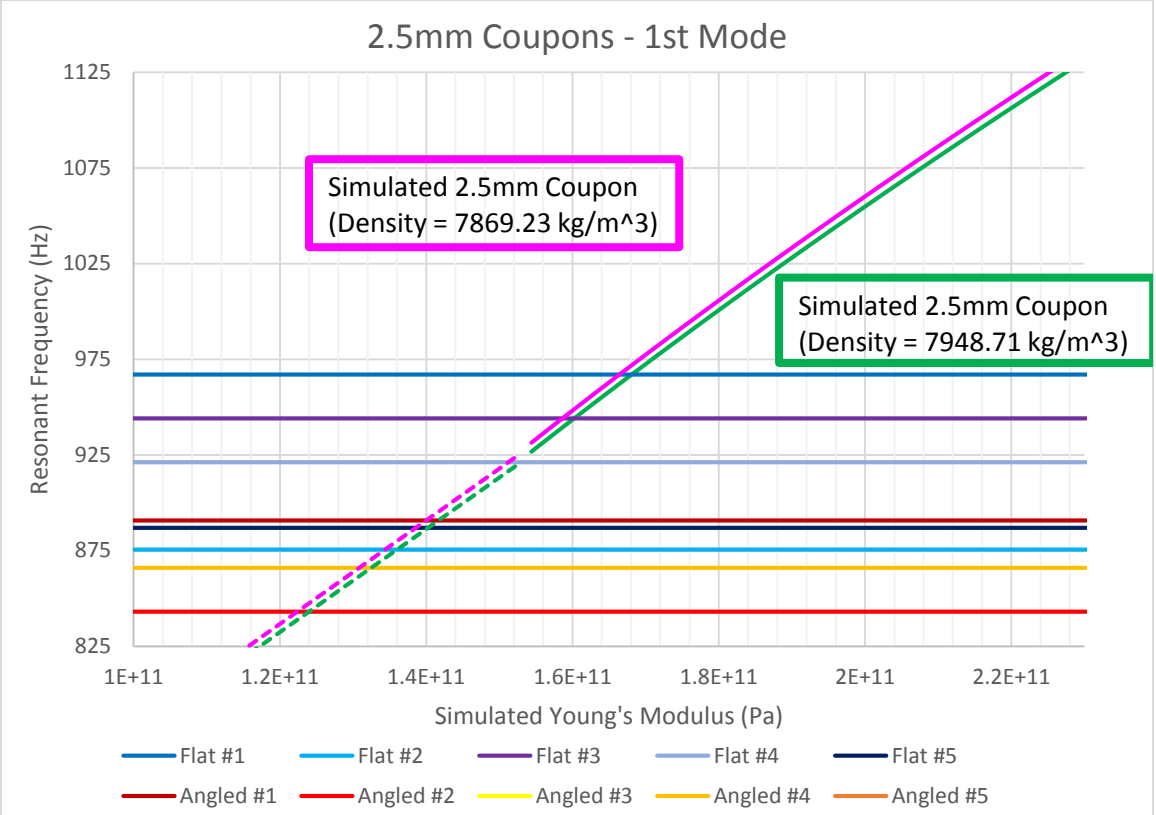
2.5mm Coupons - 1st Mode
Resonant Frequency (Hz)
1125
1075
1025
975
925
875
825
1E+11
1.2E+11
1.4E+11
1.6E+11
1.8E+11
2E+11
2.2E+11
Simulated Young's Modulus (Pa)
Simulated 2.5mm Coupon (Density = 7869.23 kg/m^3)
Simulated 2.5mm Coupon (Density = 7948.71 kg/m^3)
Flat #1
Flat #2
Flat #3
Flat #4
Flat #5
Angled #1
Angled #2
Angled #3
Angled #4
Angled #5

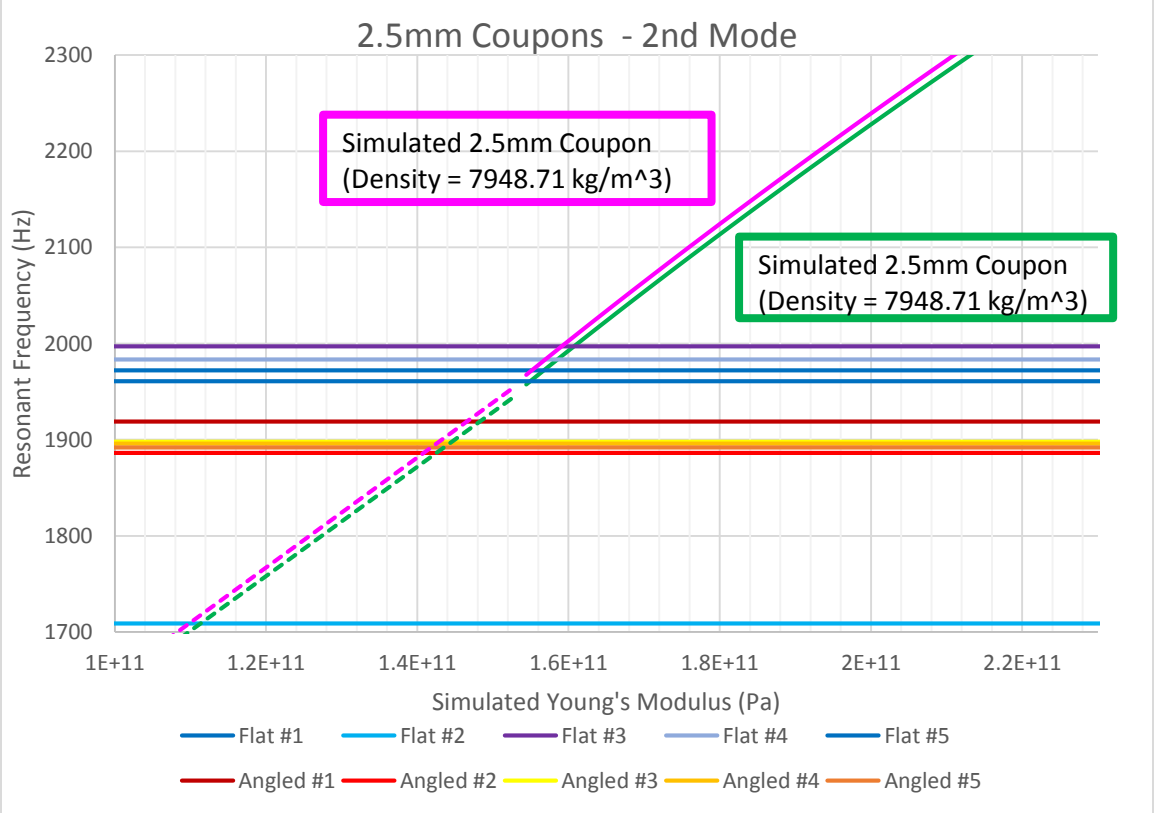
2.5mm Coupons - 2nd Mode
Resonant Frequency (Hz)
2300
2200
2100
2000
1900
1800
1700
1E+11
1.2E+11
1.4E+11
1.6E+11
1.8E+11
2E+11
2.2E+11
Simulated Young's Modulus (Pa)
Simulated 2.5mm Coupon (Density = 7948.71 kg/m^3)
Simulated 2.5mm Coupon (Density = 7948.71 kg/m^3)
Flat #1
Flat #2
Flat #3
Flat #4
Flat #5
Angled #1
Angled #2
Angled #3
Angled #4
Angled #5

A.6 Young's Modulus Values

Young's modulus - First Mode (Density = 7948.71 kg/m^3)								
Coupon #	0.5mm Flat	0.5mm Angled	1.0mm Flat	1.0mm Angled	1.5mm Flat	1.5mm Angled	2.0mm Flat	2.0mm Angled	2.5mm Flat	2.5mm Angled
1	1.365E+11	1.140E+11	1.730E+11	1.150E+11	1.825E+11	1.340E+11	1.685E+11	1.330E+11	1.680E+11	1.390E+11
2	1.390E+11	9.890E+10	1.730E+11	1.170E+11	1.800E+11	1.560E+11	1.715E+11	1.300E+11	1.340E+11	1.218E+11
3	1.390E+11	9.690E+10	1.760E+11	1.170E+11	1.760E+11	1.210E+11	1.721E+11	1.390E+11	1.600E+11	NaN
4	1.370E+11	1.000E+11	1.750E+11	1.148E+11	1.780E+11	1.580E+11	1.680E+11	NaN	1.508E+11	1.300E+11
5	1.370E+11	9.690E+10	1.750E+11	1.140E+11	1.763E+11	1.425E+11	1.710E+11	7.100E+10	1.380E+11	NaN
Young's modulus - First Mode (Density = 7869.23 kg/m^3)										
Coupon #	0.5mm Flat	0.5mm Angled	1.0mm Flat	1.0mm Angled	1.5mm Flat	1.5mm Angled	2.0mm Flat	2.0mm Angled	2.5mm Flat	2.5mm Angled
1	1.346E+11	1.120E+11	1.710E+11	1.140E+11	1.805E+11	1.320E+11	1.650E+11	1.300E+11	1.665E+11	1.375E+11
2	1.370E+11	9.700E+10	1.710E+11	1.160E+11	1.780E+11	1.545E+11	1.680E+11	1.279E+11	1.320E+11	1.200E+11
3	1.370E+11	9.510E+10	1.730E+11	1.160E+11	1.740E+11	1.190E+11	1.685E+11	1.355E+11	1.585E+11	NaN
4	1.350E+11	9.890E+10	1.725E+11	1.130E+11	1.762E+11	1.560E+11	1.645E+11	NaN	1.490E+11	1.287E+11
5	1.350E+11	9.510E+10	1.730E+11	1.120E+11	1.745E+11	1.410E+11	1.675E+11	6.800E+11	1.366E+11	NaN
Young's modulus - Second Mode (Density = 7948.71 kg/m^3)										
Coupon #	0.5mm Flat	0.5mm Angled	1.0mm Flat	1.0mm Angled	1.5mm Flat	1.5mm Angled	2.0mm Flat	2.0mm Angled	2.5mm Flat	2.5mm Angled
1	1.393E+11	1.120E+11	1.770E+11	1.310E+11	1.762E+11	1.110E+11	1.470E+11	1.745E+11	1.548E+11	1.460E+11
2	1.390E+11	9.690E+10	1.742E+11	1.385E+11	1.730E+11	1.315E+11	1.645E+11	1.685E+11	1.090E+11	1.405E+11
3	1.410E+11	9.600E+10	1.733E+11	1.360E+11	1.680E+11	1.140E+11	1.770E+11	1.705E+11	1.608E+11	1.426E+11
4	1.390E+11	1.000E+11	1.739E+11	1.280E+11	1.700E+11	1.480E+11	1.640E+11	1.715E+11	1.585E+11	1.422E+11
5	1.380E+11	9.440E+10	1.739E+11	1.175E+11	1.663E+11	1.425E+11	1.740E+11	1.695E+11	1.565E+11	1.410E+11
Young's modulus - Second Mode (Density = 7869.23 kg/m^3)										
Coupon #	0.5mm Flat	0.5mm Angled	1.0mm Flat	1.0mm Angled	1.5mm Flat	1.5mm Angled	2.0mm Flat	2.0mm Angled	2.5mm Flat	2.5mm Angled
1	1.365E+11	1.090E+11	1.950E+11	1.480E+11	1.745E+11	1.090E+11	1.455E+11	1.725E+11	1.520E+11	1.446E+11
2	1.360E+11	9.420E+10	1.920E+11	1.560E+11	1.710E+11	1.300E+11	1.630E+11	1.665E+11	1.070E+11	1.390E+11
3	1.380E+11	9.380E+10	1.910E+11	1.540E+11	1.660E+11	1.125E+11	1.750E+11	1.690E+11	1.590E+11	1.410E+11
4	1.360E+11	9.720E+10	1.913E+11	1.440E+11	1.682E+11	1.460E+11	1.620E+11	1.700E+11	1.565E+11	1.406E+11
5	1.350E+11	9.150E+10	1.913E+11	1.330E+11	1.645E+11	1.410E+11	1.720E+11	1.675E+11	1.550E+11	1.400E+11

A.7 Simulation Parameters

#	Cantilever Thickness (mm)	Density (kg/m^3)	Young's Modulus (Pa)
1	0.4	6200	1.544E+11
2	0.45	6279.487179	1.56379E+11
3	0.5	6358.974359	1.58359E+11
4	0.55	6438.461538	1.60338E+11
5	0.6	6517.948718	1.62318E+11
6	0.65	6597.435897	1.64297E+11
7	0.7	6676.923077	1.66277E+11
8	0.75	6756.410256	1.68256E+11
9	0.8	6835.897436	1.70236E+11
10	0.85	6915.384615	1.72215E+11
11	0.9	6994.871795	1.74195E+11
12	0.95	7074.358974	1.76174E+11
13	1	7153.846154	1.78154E+11
14	1.05	7233.333333	1.80133E+11
15	1.1	7312.820513	1.82113E+11
16	1.15	7392.307692	1.84092E+11
17	1.2	7471.794872	1.86072E+11
18	1.25	7551.282051	1.88051E+11
19	1.3	7630.769231	1.90031E+11
20	1.35	7710.25641	1.9201E+11
21	1.4	7789.74359	1.9399E+11
22	1.45	7869.230769	1.95969E+11
23	1.5	7948.717949	1.97949E+11
24	1.55	8028.205128	1.99928E+11
25	1.6	8107.692308	2.01908E+11
26	1.65	8187.179487	2.03887E+11
27	1.7	8266.666667	2.05867E+11
28	1.75	8346.153846	2.07846E+11
29	1.8	8425.641026	2.09826E+11
30	1.85	8505.128205	2.11805E+11
31	1.9	8584.615385	2.13785E+11
32	1.95	8664.102564	2.15764E+11
33	2	8743.589744	2.17744E+11
34	2.05	8823.076923	2.19723E+11
35	2.1	8902.564103	2.21703E+11
36	2.15	8982.051282	2.23682E+11
37	2.2	9061.538462	2.25662E+11
38	2.25	9141.025641	2.27641E+11
39	2.3	9220.512821	2.29621E+11
40	2.35	9300	2.316E+11
41	2.4		
42	2.45		
43	2.5		
44	2.55		
45	2.6		